Capacitive Micromachined Ultrasonic Transducers (CMUTs) for Humidity Sensing

by

Zhou Zheng

A thesis

presented to the University of Waterloo

in fulfillment of the

thesis requirement for the degree of

Doctor of Philosophy

in

Department of Systems Design Engineering

Waterloo, Ontario, Canada, 2019

© Zhou Zheng 2019

Examining Committee Membership

The following served on the Examining Committee for this thesis. The decision of the Examining Committee is by majority vote.

External Examiner: Dr. Sazzadur Chowdhury
Professor, Electrical and Computer Engineering
University of Windsor

Supervisor: Dr. John T.W. Yeow
Professor, Systems Design Engineering
University of Waterloo

Internal Member: Dr. Ning Jiang
Assistant Professor, Systems Design Engineering
University of Waterloo

Internal-external Member: Dr. Dayan Ban
Professor, Electrical and Computer Engineering
University of Waterloo

Internal-external Member: Dr. John Z. Wen
Associate Professor, Mechanical & Mechatronics Engineering
University of Waterloo

Author's Declaration

I hereby declare that I am the sole author of this thesis. This is a true copy of the thesis, including any required final revisions, as accepted by my examiners.

I understand that my thesis may be made electronically available to the public.

Statement of Contributions

This thesis contains three co-authored journal articles where I was the primary author and one piece of work that is not published yet. I am responsible for all the sensor design, fabrication, characterization, and application. The co-authors have provided insights and helped with equipment training, part of the experimental setup, reviewing, and editing. Below is the list of the articles and work.

1. *Development of a novel CMUT-based concentric dual-element ultrasonic transducer.*

   This work is presented in Chapter 4 and published in a refereed journal [1]:

   Z. Zheng, S. Na, A. I. H. Chen, Z. Li, L. L. P. Wong, Z. Sun, Y. Yao, P. Liu, and J. T. W. Yeow, "Development of a novel CMUT-based concentric dual-element ultrasonic transducer: Design, fabrication, and characterization," ***Journal of Microelectromechanical Systems,*** **vol. 27, no. 3, pp. 538–546, 2018.**

2. *Development of a highly sensitive humidity sensor based on CMUT.*

   This work is presented in Chapter 5 and published in a refereed journal [2]:

   Z. Zheng, Y. Yao, Y. Sun, and J. Yeow, "Development of a highly sensitive humidity sensor based on the capacitive micromachined ultrasonic transducer," ***Sensors and Actuators B: Chemical,*** **vol. 286, pp. 39–45, 2019.**

3. *Highly sensitive CMUT-based humidity sensors built with nitride-to-oxide wafer bonding technology.*

   This work is presented in Chapter 6 and published in a refereed journal [3]:

Z. Zheng, Y. Yao, J. A. Liu, Y. Sun, and J. T. W. Yeow, "Highly sensitive CMUT-based humidity sensors built with nitride-to-oxide wafer bonding technology," *Sensors and Actuators B: Chemical,* **vol. 294, pp. 123–131, 2019.**

4. *A multi-resonance CMUT for sensing applications.*

This work is presented in Chapter 7 and is not published yet.

Abstract

In the last two decades, capacitive micromachined ultrasonic transducers (CMUTs) have proven themselves to be promising for various ultrasound imaging and chemical sensing applications. Although holding many benefits for ultrasound imaging, CMUTs have certain weaknesses such as the relatively low output pressure at transmission, which hinder their development in the diagnostic imaging application. In the sensing area, CMUTs have shown attractive features such as high mass sensitivity, miniaturized array configuration, and ease of functionalization. However, their potential for humidity sensing is less explored. The objectives of this thesis lie in two aspects. One is to offer a solution to overcome the limitation of low output pressure, and the other is to develop CMUTs as resonant gravimetric humidity sensors. The major efforts are made on the second task.

For the first objective, a novel dual-element ultrasonic transducer is proposed. It incorporates two transducer technologies by using a circular piezoelectric element for ultrasound transmission and an annular CMUT element for reception. The hybrid transducer combines the broad bandwidth and high receive sensitivity of the CMUT and the high output power of the piezoelectric transducer to improve the overall sensitivity and axial resolution. The annular CMUT is designed, fabricated, and concentrically aligned with the piezoelectric probe via a custom housing. Immersion measurements

show that the hybrid dual-element transducer improves the axial resolution by 25.58% and the signal-to-noise ratio by 8.55 dB over the commercial piezoelectric probe.

For the second objective, a CMUT-based resonant humidity sensor is first developed with the direct wafer bonding technique. Graphene oxide (GO) is employed as the sensing material. Due to combination of the mass-sensitive CMUT and the moisture-sensitive GO, the sensor exhibits rapid response/recovery, good repeatability, and higher sensitivity than most of its competitors. The second generation of CMUT-based humidity sensors aims to further improve the relative humidity (RH) sensing performance by adopting the nitride-to-oxide wafer bonding technology for CMUT fabrication. In contrast to conventional wafer bonding CMUT processes that use expensive silicon-on-insulator (SOI) wafers to produce resonating membranes, the new process employs low-pressure chemical vapor deposition (LPCVD) silicon nitride as the membrane material. It provides thinner and lighter membranes, and thus more sensitive CMUT resonators. Additional benefits of the nitride-to-oxide wafer bonding technique are the reduced fabrication complexity and more controllable membrane thickness. Finally, a dual-frequency (10/14 MHz) CMUT is developed using this fabrication technique. It generates two RH response curves and can provide more accurate RH sensing. Due to the independence of the two resonance frequencies, the dual-frequency CMUT also shows great potential for identification of different chemicals. This thesis demonstrates that CMUT sensors can be strong candidates for miniaturized, highly sensitive, and reliable humidity sensors.

Acknowledgements

First, I would like to express my sincere thanks to my supervisor, Prof. John T.W. Yeow, for offering me the valuable opportunity to work in his lab and supporting me on the research projects. It takes a visionary and determined supervisor to send students to work in cleanrooms considering the high cost. Luckily, I have such a supervisor. Over the past years, I have spent countless hours and used countless expensive wafers and materials in the cleanrooms. Prof. Yeow has always been supportive, and I am really grateful for that. I would also like to thank the other members of my committee – Prof. Dayan Ban, Prof. John Wen, Prof. Ning Jiang, and Prof. Sazzadur Chowdhury – for generously sharing their time and expertise.

I also would like to thank my lab mates for their help and friendship. I own special thanks to Albert Chen for guiding me into the world of MEMS and for always replying my questions no matter how silly the questions are, to Shuai Na and Zhenhao Li for sharing their hard-earned cleanroom experience, to Lawrence Wong and Fred Sun for their help on electronics, to Champika Samarasekera and Chen Chen for their technical discussions.

I want to thank a long list of people who made my study and life in Waterloo enjoyable. Specially, thank the staffs in the cleanrooms for their training and for keeping the equipment in a good condition. Thank Czang-Ho, Harlan, Mohsen, Ferhat, Celal, Ruifeng, Navid, and all those amazing guys who helped me out of my difficult times in

the cleanrooms. It has been a privilege to work with you guys in such an incredible community! Thank Prof. Eihab Abdel-Rahman for allowing me to use the laser vibrometer in his lab and thank Mohamed Arabi for his help on this equipment. Thank Prof. Yao Yao for sharing his expertise in the sensing area.

Lastly, and most importantly, I want to express my deepest appreciation to my family for all the support and encouragement throughout the past years.

Table of Contents

List of Tables

List of Figures

Chapter 1　Introduction

1.1 Motivation

Capacitive micromachined ultrasonic transducers (CMUTs), as microelectromechanical systems (MEMS) based devices, have attracted tremendous attentions since invented in 1994 [4]. They were first introduced for air-coupled non-destructive testing (NDT) applications [5]. In the last decades, CMUTs have gained more interests in immersion applications, especially in biomedical imaging [6]–[8]. Compared to conventional piezoelectrical transducers, CMUTs offer many unique characteristics such as broad bandwidth, high receive sensitivity, ease of constructing high-density arrays, and simple integration with electronics, which are favorable for miniaturized high-resolution imaging systems. Despite the advantages, CMUTs inherently suffer from low output pressure due to their limited effective membrane and deflection areas [9]. The inferior transmission performance leads to a lower overall sensitivity than the piezoelectric competitors. The first objective of this work is to provide a solution that can harness the promising benefits of CMUTs while ensuring the overall sensitivity of the transducer.

In addition to ultrasonic transducers, CMUTs can also be seen as gravimetric resonators because they are made of multiple drum-like resonator structures that are electrically connected in parallel. In the last decade, CMUTs have been extensively

investigated for bio/chemical sensing applications based on gravimetric detection [10]–[14]. After coating with a sensing film, a CMUT sensor is able to adsorb a specific analyte, which can be detected by monitoring the resonance frequency shift caused by the loaded mass. In the area of sensing, CMUTs have shown promising features such as high mass sensitivity and reliability, low limit of detection, ease of functionalization, and miniaturized array footprint for multi-analyte sensing. Many analytes have been studied to demonstrate the superiority of CMUTs in the sensing area. However, CMUTs' potential for humidity sensing is less explored.

Humidity detection is of significant importance in a wide variety of applications from our living environment to industrial processes [15], [16]. MEMS technology provides promising solutions to implement portable, sensitive, and reliable humidity sensors. Such humidity sensors include surface acoustic wave (SAW) sensors [17], film bulk acoustic resonators (FBARs) [18], and micro-cantilevers [19]. However, each of these sensors encounters certain limitations. SAW sensors have large footprints when constructed as arrays for selectivity enhancement [12]. FBARs have a low fabrication yield due to the lengthy back etching or sacrificial release fabrication process [20]. Micro-cantilevers suffer from a low quality factor and thus a low mass resolution [12].

The second objective of this dissertation is to develop highly sensitive CMUT-based humidity sensors that are also fast-response, repeatable, and reliable, and to demonstrate the potential of miniaturized CMUTs for selective sensing of multiple analytes including the humidity. This includes design, fabrication, and characterization of the CMUTs,

selection of the sensing materials, as well as performance evaluation and improvement of the sensors.

1.2 Thesis Outline

This thesis is organized into eight chapters. Chapter 2 first provides the relevant background of CMUTs including their operational principle, applications and advantages, and fabrication techniques; then briefly reviews the present resonant humidity sensors and corresponding sensing materials.

Chapter 3 presents the analytical model and finite element simulation of the CMUT.

Chapter 4 reports the hybrid ultrasound transducer that incorporates a CMUT and a piezoelectric probe. The design and detailed fabrication process are followed by the concentric integration scheme and the characterization results.

Chapter 5 presents a highly sensitive CMUT-based humidity sensor that uses GO as the sensing material. The CMUT is designed, fabricated and characterized. The sensing performance of the resonator including the RH sensitivity, the repeatability, the response and recovery time, and the hysteresis is demonstrated.

Chapter 6 is dedicated to further improving the humidity sensing performance of the CMUTs by introducing the nitride-to-oxide wafer bonding fabrication process. The design, fabrication, characterization, and sensing performance of the sensors are presented. Three different concentrations of GO dispersion were used to functionalize the CMUTs and their influences on the devices are investigated.

Chapter 7 reports the development of a multi-resonance CMUT for sensing applications. The characterization and humidity sensing results are presented.

Chapter 8 summarizes the contributions of this thesis and proposes future work.

Chapter 2 Background

2.1 Capacitive Micromachined Ultrasonic Transducers

A CMUT cell can be roughly considered as a parallel-plate capacitor, as shown in Fig. 2.1. It consists of a moving membrane with an electrode atop and a rigid substrate separated by an insulator and a vacuum cavity. A single CMUT element is made of tens to thousands of such cell structures electrically connected in parallel. When an AC signal, superimposed on a DC bias, is applied across the electrodes, the membrane vibrates and transmits ultrasonic waves. In the reception mode, when an incident acoustic wave hits the surface of the biased CMUT, the capacitance between the electrodes is changed and induces a current which can be converted to a voltage signal and be measured.
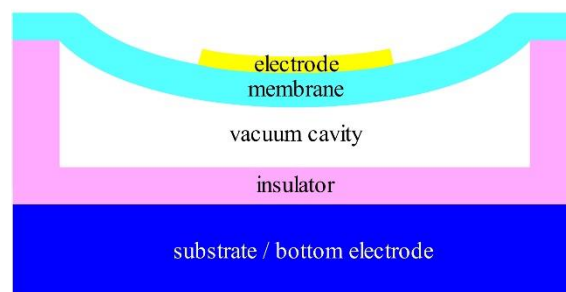
Fig. 2.1: Schematic of basic CMUT cell structure

2.1.1 CMUTs for Ultrasound Imaging

Conventionally, almost all ultrasound imaging is realized by piezoelectric transducers. Based on the piezoelectric effect, a piezoelectric probe converts an electrical pulse into mechanical vibration and generates ultrasound into the medium; the reverse is true when it is as a receiver. Lead-zirconate-titanate ceramic (PZT) is the most commonly

5

used piezoelectric material due to its high electromechanical conversion efficiency [21].

Fig. 2.2 shows the structure of a typical single-element piezoelectric probe. It consists of a piezoelectric crystal (PZT), a matching layer, a backing layer, a metal housing, and an acoustic lens. PZT inherently has a much higher acoustic impedance ($Z_{PZT} \approx 34$ MRay1) than tissue ($Z_{tissue} = 1.5$ MRay1). Hence, a matching layer is required for impedance matching to ensure sufficient ultrasound transmission [22]. The vibration of PZT often lasts for several cycles and stops gradually after the electrical excitation. This phenomenon is termed 'ringing effect'. It reduces the bandwidth and thus the axial resolution of the transducer. The backing layer is used to reduce excessive vibration by absorbing mechanical energy. The dissipation of the acoustic power, however, leads to a compromised transducer sensitivity. An acoustic lens is layered on top of the matching layer. It focuses ultrasonic waves and improves the imaging resolution. Although piezoelectric technology has been dominating the market, it has certain limitations. For example, high-density piezoelectric transducer arrays are difficult to manufacture because the fabrication uses mechanical dicing methods to define the array elements and scaling down the elements is very challenging. In addition, the multiple structural layers typically lead to a bulky probe, making it unsuitable for miniaturized imaging applications such as intravascular imaging and endoscopic imaging.
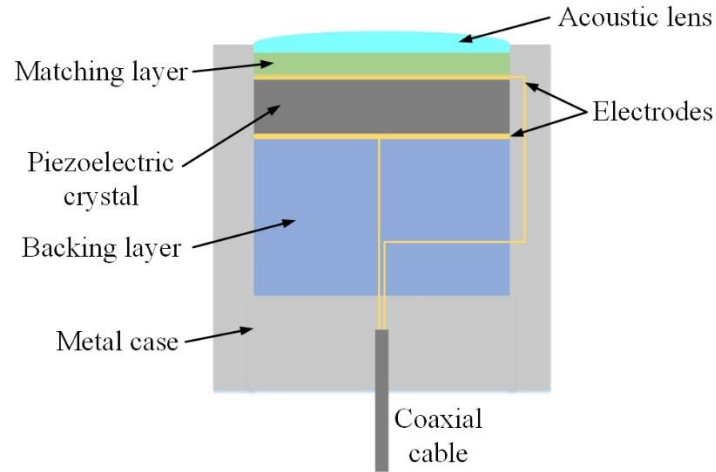
Fig. 2.2: Structure of a single-element piezoelectric probe

As a relatively new transducer technology, CMUTs provide several advantages over piezoelectric transducers. First, the acoustic impedance of CMUTs inherently matches to the surrounding medium, so matching layers are not required [23]. Second, CMUTs are generally fabricated from a silicon wafer using standard integrated circuit (IC) manufacturing techniques, thus benefiting from all the capabilities that IC technology has. One of these attractive abilities is that CMUTs can be seamlessly integrated with electronics [24]–[27], resulting in improved noise performance and receive sensitivity [27]. Moreover, micromachining techniques enable CMUTs to be fabricated into arrays and single elements with a wide range of sizes and shapes, which can be difficult with conventional piezo-based processing techniques. In terms of acoustic performance, CMUTs can easily achieve a fractional bandwidth of over 100%, while that of piezoceramic-based transducers is typically limited to 60% to 80% [7]. The fractional bandwidth is the bandwidth of a transducer divided by its center frequency [28]. A wider fractional bandwidth corresponds to a shorter acoustic pulse and thus a better axial

resolution. Furthermore, CMUTs have been reported to have a higher receiving sensitivity than the piezoelectric counterpart [29]–[31]. With all these features, CMUTs have been considered as a strong alternative to piezoelectric transducers in the ultrasound imaging field.

2.1.2 CMUTs for Bio/Chemical Sensing
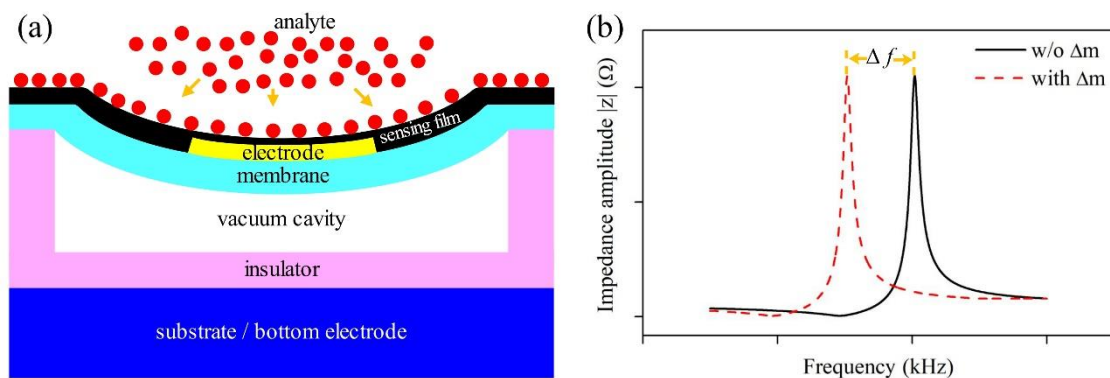
Fig. 2.3: Working mechanism of CMUT as a gravimetric sensor.

In addition to the area of ultrasound imaging, CMUTs have also gained increasing interests in bio/chemical sensing in recent years. CMUTs can be functionalized with sensing materials and be used as gravimetric sensors due to the nature of their resonating structure. Their working mechanism is shown in Fig. 2.3. The added mass of adsorbed analyte induces a resonance frequency shift of the sensor and can be detected. CMUTs have been demonstrated as highly sensitive and reliable bio/chemical sensors by several research groups [10], [12], [14], [32]. First, CMUTs have a high mass sensitivity due to the light weight (sub-nanogram level) of the resonating membrane. Second, as other gravimetric sensor types are often comprised of a single resonating structure, the multi-resonator structure of CMUTs not only enhances the device reliability but also reduces

the motional impedance and thus minimizes the thermal noise [11]. Third, the closed and

flat surface of CMUTs eases coating of the functional layer, which is essential to make

the gravimetric sensors selective to a specific analyte. Moreover, an array with several

CMUT elements can be easily fabricated and integrated with circuits, allowing multi-

analyte sensing in a miniaturized footprint [33]. The analytes that have been studied

include acetone, isopropanol, methanol [10], carbon dioxide [34], [35], sulfur dioxide

[14], dimethyl methylphosphonate (DMMP) [11], [12], [36], [37], and benzyl methyl

ketone (BMK) [32]. Yet, more potentials of CMUTs are to be explored in the sensing area.

2.1.3 Fabrication Methods
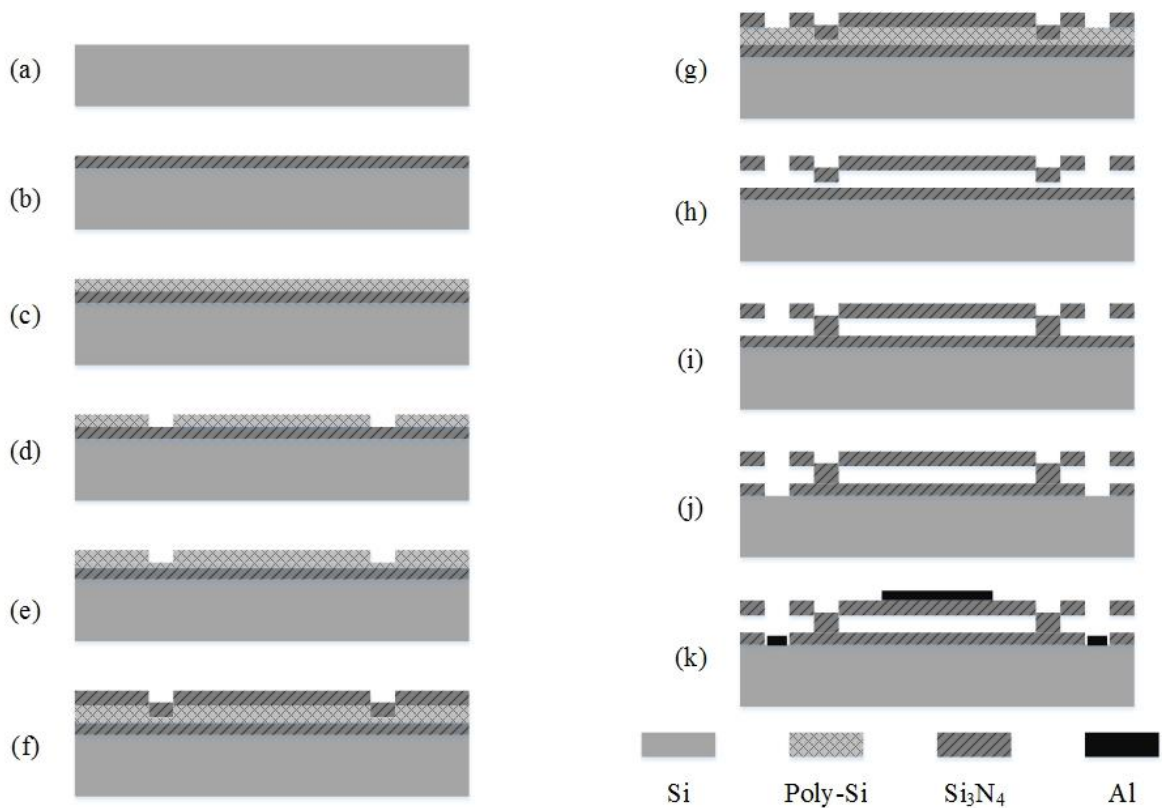
Fig. 2.4: Sacrificial release process for CMUT fabrication [9].

For both ultrasound imaging and bio/chemical sensing applications, one of the major advantages of CMUTs is their microfabrication process. It benefits not only a miniaturized footprint, but also enhanced performance. Two techniques are usually used for CMUT fabrication: the sacrificial release process [9] and the wafer bonding process [38].

The sacrificial release process is the first technique that is adopted to fabricate CMUTs [9]. Fig. 2.4 depicts the process flow. It starts with a highly doped silicon wafer (step a). First, a silicon nitride (Si_3N_4) etch-stop layer is deposited on the substrate with low pressure chemical vapor deposition (LPCVD) (step b). Polysilicon is generally used as the sacrificial layer, which is deposited in two steps. The first layer of polysilicon is deposited with LPCVD (step c), then patterned and dry etched for the channels (step d). The etching stops at the underneath Si_3N_4 layer. Then the second thin layer of polysilicon is deposited with LPCVD (step e). The thickness of the second polysilicon layer defines the thickness of the etch channels, while the total thickness of the sacrificial layer (the first and the second polysilicon layer) determines the thickness of the CMUT cavities. A photolithography and dry etch step, which is not shown in the cross-section view of the process flow, is performed to define the membrane shape and the etch channels after the second polysilicon deposition. Subsequently, the Si_3N_4 membrane is deposited by LPCVD (step f). Since another layer of Si_3N_4 will be deposited to seal the cavities, the thickness of the Si_3N_4 here is not the final thickness of the membrane. The next step is to open etch holes on the etch channels with photolithography and dry etching (step g),

followed by the membrane release step with potassium hydroxide (KOH) wet etching (step h). The cavities are then sealed with another deposition of LPCVD Si_3N_4 (step i). The last process is to create contact pads for the top and bottom electrodes. The Si_3N_4 layer is patterned and etched to expose the bottom electrodes (step j). Finally, the aluminum layer is deposited by sputtering, patterned by photolithography, and wet etched to achieve the top and bottom bonding pads (step k).
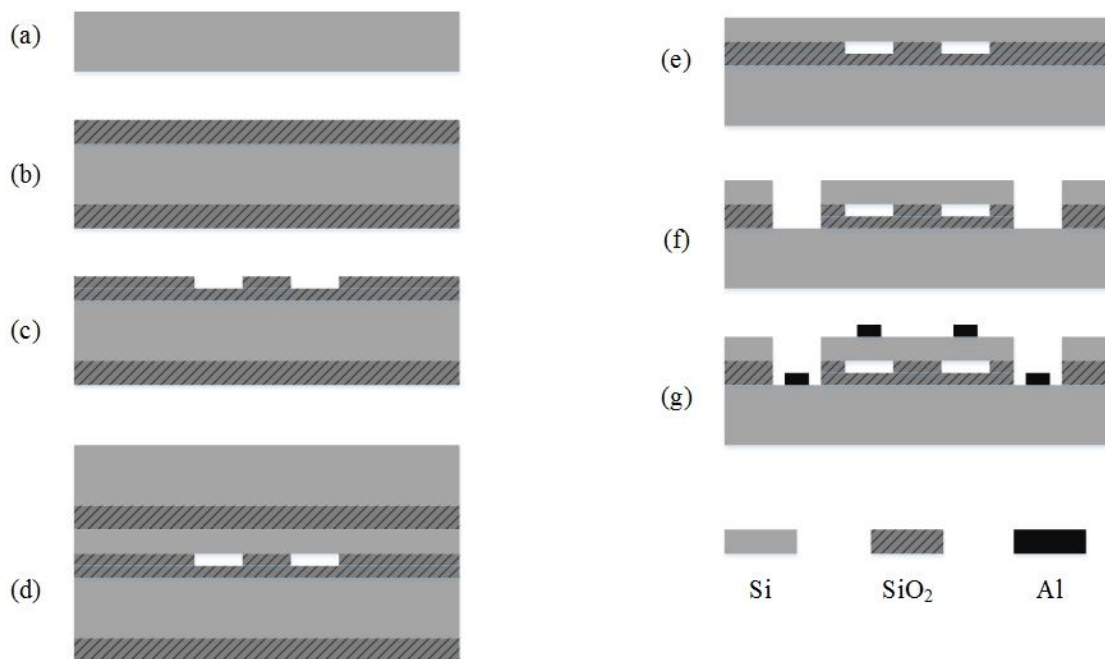
Fig. 2.5: Wafer bonding process for CMUT fabrication.

The wafer bonding process [38] is relatively new and has become a dominant technique for CMUT fabrication. Fig. 2.5 depicts the flow of a typical CMUT wafer bonding process. The fabrication begins with a highly conductive prime silicon wafer, which later serves as both the substrate and the bottom electrode. A layer of wet thermal oxide is grown on the substrate (step b). The cavities are then patterned using a photolithography and oxide reactive-ion etching (RIE) step (step c). Next, a silicon-on-

insulator (SOI) wafer with a conductive silicon device layer is bonded with the patterned substrate (step d). The bonded wafer pair is then annealed for hours to enhance the bonding strength. While the bottom silicon substrate is protected by the thermal oxide, the top silicon handling layer is removed through tetramethylammonium hydroxide (TMAH) etching, followed by wet etching of the buried oxide layer with buffered HF (BHF) (step e). Subsequently, the areas for interfacing of bottom electrodes are revealed through two dry etching steps of the silicon and SiO_2 (step f). The silicon device layer is patterned and etched with deep reactive-ion etching (DRIE) to partially reveal the bottom electrodes. Another purpose of the silicon etching step is to create isolation trenches between the CMUT elements. Next, a lithography patterning and oxide RIE step is made to fully expose the bottom electrodes (step f). Finally, an aluminum electrode layer is deposited by sputtering, followed by a wet etching process to form the metal contact pads (step g).

While process variations of both fabrication techniques have been reported, it is widely accepted that the wafer bonding process is superior to the sacrificial release process [9]. The most straightforward advantage of the wafer-bonded CMUT technique is the reduction in masks and processing steps, and consequently a lower cost and higher yield. Better control of the cavity depth is also achieved with the wafer bonding process due to the absence of the wet sacrificial release process. Additionally, wafer-bonded CMUTs have no etched holes and channels for the membrane release. As a result, a higher sensitivity is obtained due to the increased active area.

2.2 Resonant Humidity Sensors

Humidity detection has been playing an important role in increasing applications such as chemical industry processing, pharmaceutical processing, intelligent control of the living environment, and soil moisture monitoring [15], [16]. To monitor the moisture, a humidity sensor is essential. An ideal humidity sensor should have such features as high sensitivity, fast response and recovery, good reproducibility and reversibility, and low cost. According to the sensing type, humidity sensors are categorized into capacitive [39], resistive [40], optical [41], and gravimetric sensors, among which the gravimetric ones based on mass-loading effect offer such advantages as high sensitivity and fast response. Gravimetric humidity sensors include quartz crystal microbalances (QCMs) [42]–[44], surface acoustic wave (SAW) sensors [17], film bulk acoustic resonators (FBARs) [18], micro-cantilevers [19], and a potential candidate - CMUTs. Each of them will be briefly introduced below.

2.2.1   Quartz Crystal Microbalances (QCMs)
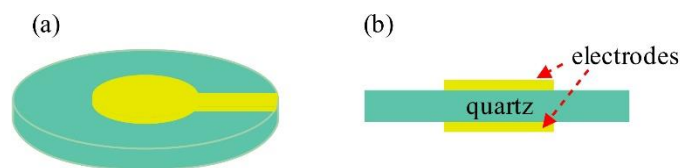
Fig. 2.6: Schematic of a QCM: (a) 3D view; (b) cross-sectional view.

QCM is the most popular and mature gravimetric sensor, known for its good stability and sensitivity. Fig. 2.6 shows the configuration of a QCM sensor, which consists of an AT-cut quartz crystal disk with a metal electrode on each side. QCMs typically operate

in bulk thickness shear mode and possess resonance frequencies between 5 to 20 MHz [45]. They are able to measure a mass change on the nanogram scale [46], [47]. The mass sensitivity of QCMs is proportional to the square of the resonance frequency. Therefore, higher sensitivity can be achieved by thinner crystals which operate at higher fundamental resonance frequencies. However, thinning down quartz crystals beyond the normal ranges imposes fabrication challenges and leads to extremely fragile devices [48]. Another drawback of QCMs is that the crystals are off-chip components and are not IC-compatible. As a result, the sensing system is usually bulky.

2.2.2 Film Bulk Acoustic Resonators (FBARs)
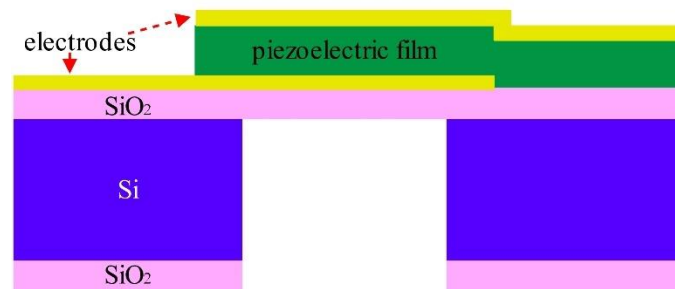
Fig. 2.7: Schematic of an FBAR.

FBAR is another type of bulk acoustic wave (BAW) based device. A schematic of an FBAR is shown in Fig. 2.7. It consists of a piezoelectric layer sandwiched between two electrodes and mounted on a suspended membrane, which is usually SiO_2 [45] and Si_3N_4 [49]. FBAR has a similar working principle to QCM. The major differences between them are the material and dimension of the piezoelectric layer. Zinc oxide and aluminum nitride are the commonly used materials for FBARs due to their superior piezoelectric properties such as high electromechanical coupling coefficient, high

acoustic velocity, and low acoustic loss. FBARs also differentiate from QCMs on the membrane structure, which is completely isolated from the substrate such that the acoustic energy loss is minimized [50]. FBAR devices typically have a piezoelectric layer thickness of only a few microns and hence resonate at very high frequencies between 500 MHz and 5 GHz [45]. As a result, they usually have much higher sensitivity than QCMs. Moreover, FBAR devices are produced by thin-film technology, which is promising for array and IC integration. However, FBARs currently have a very low fabrication yield due to some practical challenges such as the lengthy back etching of the bulk substrate. The hardly predictable combined residual stress of the membrane and the piezoelectric film also makes it difficult to design and fabricate FBARs [20]. Consequently, most of the reported FBARs work as single elements. Moreover, FBARs suffer from a low quality factor due to the high energy loss [51]. As a newcomer in the sensing field, FBAR is expected to be a great candidate for sensing applications providing the challenges can be addressed.

2.2.3   Surface Acoustic Wave (SAW) Sensors
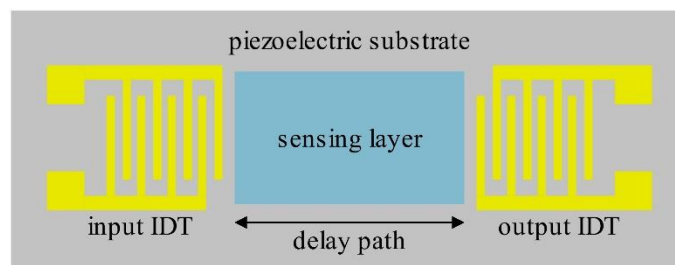
Fig. 2.8: Schematic of a SAW sensor.

SAW device is another alternative of acoustic wave-based gravimetric sensors. Unlike QCMs and FBARs that use bulk acoustic waves, SAW devices utilize acoustic waves confined to the surface of the structure. Fig. 2.8 shows the commonly used two-port configuration of a SAW sensor. Two sets of interdigital electrode transducers (IDTs) are separated by a delay path and located on top of a piezoelectric substrate. With a signal applied to the input IDT, the acoustic wave is emitted over the delay line to the output IDT, where the mechanical wave is converted to an analyzable electrical signal. The sensing film is deposited on the delay path. As the acoustic energy concentrates on the surface of the device within only one or two wavelengths, subtle surface perturbations such as mass loading and electric loading will have a considerable impact on the wave and induce a frequency shift. As a humidity sensor platform, SAW device offers several advantages such as high sensitivity and fast response [17]. The weaknesses of SAW-based humidity sensors include the lack of thermal stability and CMOS-compatibility [51].

2.2.4 Microcantilevers
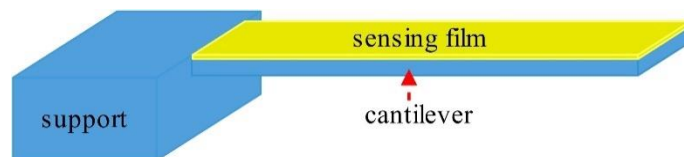
Fig. 2.9: Basic structure of a microcantilever.

Microcantilevers are among the simplest MEMS-based resonators. The basic structure of a microcantilever resonator is shown in Fig. 2.9. It is like a microscale diving board that moves up and down. The operating mechanism of microcantilevers varies as

the sensor structure. One option is actuating the structure piezoelectrically and measuring the resonance frequency by piezoresistors [52]. Microcantilevers are fabricated with MEMS technology. Therefore, they are available as miniature multi-channel structures for selective sensing. However, the low quality factor of microcantilevers has limited the sensor resolution [12]. To address this problem, approaches such as downsizing cantilevers to the nanoscale are under active investigations [53].

2.2.5 CMUTs

CMUT is expected to be an outstanding alternative as a humidity sensor platform. The CMOS-compatible fabrication process of CMUTs enables easy integration with electronics and allows miniaturization of selective sensing systems by implementing tiny multi-element sensor arrays, which is difficult for conventional QCM and SAW sensors. Compared with microcantilevers, CMUTs have advantages such as a higher quality factor and ease of functionalization due to their closed and flat membrane surface. One of the objectives of this work is to develop CMUT-based humidity sensors and evaluate their potential in this area.

2.3 Sensing Materials

It is known that the sensing performance of a resonant gravimetric sensor is determined by both the transducer itself and the functional material. Therefore, selection of the sensing material is of vital importance. The general requirements for a sensing material include high sensitivity, rapid response and recovery, good reversibility, and

prolonged environmental stability. Meanwhile, the material should also have such features as good adhesion to the substrate, ease of processing, and low cost. At present, the most commonly used materials are polymers and metal oxides, while some other materials are under active development.

2.3.1 Polymers

Polymers and polymer-based composites have a history of over 40 years as humidity sensing materials [54]. They have exhibited good mechanical and adhesive properties that control the longevity of the sensors [51]. Some of the reported hygroscopic polymers include cellulose derivatives [55], poly-methylmeth-acrylate (PMMA) [56], and polyvinylidene fluoride (PVDF) [57]. The high capacity and rapid diffusion of amorphous polymers make them attractive for humidity sensing applications due to their high sensitivity and fast response [54]. Moreover, some polymers such as Nafion have excellent chemical stability, which allows them to be operated in the atmosphere with organic vapors and dust [51]. Other advantages of polymers include simple fabrication and low cost [58].

2.3.2 Metal Oxides

Metal oxide films can also be utilized as hygroscopic layers. At present, some metal oxides such as Al_2O_3 [59], ZnO [60] and TiO_2 [61]–[63] have been applied to QCM and SAW-based sensors. However, their application in humidity sensing is much less common than polymers because of their inferior hygroscopic capability. For SAW-based humidity sensors, the metal oxide sensing layer can interact with water vapors and induce

a considerable change in the electrical conductivity, which helps improve the humidity sensitivity. An advantage of metal oxides is their stability in corrosive environment. However, metal oxides usually have inadequate adhesion to the substrate when using low-temperature processes, which limits their applications [51].

2.3.3 Other Materials

Some other materials have also been studied for gravimetric humidity sensors. With high sensitivity being one of the most critical characteristics, microporous materials that have large surface areas and high adsorption capacity are adopted. Some of these materials are black phosphorous [64], carbon nanotubes (CNTs) [65], and metal-organic framework materials (MOFs) [66], [67]. Particularly, in the recent decade, graphene oxide (GO) has been emerging as a superior material for moisture sensing and has been adopted for QCM [42]–[44] and SAW-based humidity sensors [17]. It is an oxidized product of graphene and it has such reactive oxygen functional groups as carboxyl, hydroxyl, and epoxy. These oxygen groups render GO hydrophilic and make it an excellent hygroscopic material. Moreover, GO is easily accessible and low-cost [41]. Due to these advantages, GO is selected as the sensing material throughout this thesis.

Chapter 3　CMUT Modeling

Modeling of CMUTs is of critical importance because it helps predict the performance of the device at the design stage. In this Chapter, the analytical model and the finite element analysis (FEA) model of a CMUT are introduced. Both models assume that the membrane of the CMUT is conductive <100> oriented single crystal silicon, which also serves as the top electrode.

3.1 Mass-Spring-Damper Model
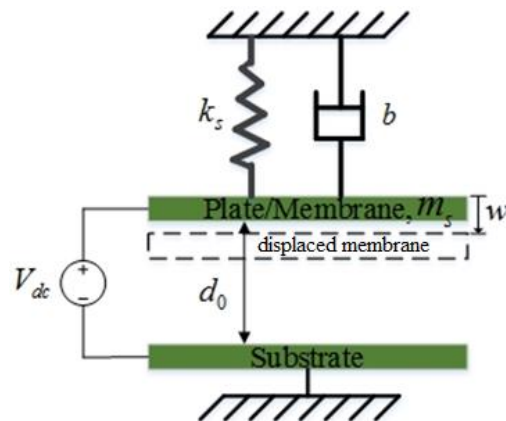
Fig. 3.1: CMUT mass-spring-damper model

The mass-spring-damper model is used to derive some important CMUT parameters such as the resonance frequency and the pull-in voltage. The model simplifies the CMUT membrane as a rigid plate supported by a spring and a damper anchored on a substrate, as depicted in Fig. 3.1. This model assumes the top plate is limited to a small piston-like displacement, i.e., the plate does not deform. It is not true in practical situations because the membrane displacement generally peaks at the center and decreases towards the

clamped edge. Therefore, an adjusted plate area is required to ensure the accuracy of the model. To derive the equivalent plate area, we assume that the actual membrane and the plate displace the same volume under the same condition. Fig. 3.2 displays the CMUT with a deformed membrane and the equivalent circular plate.
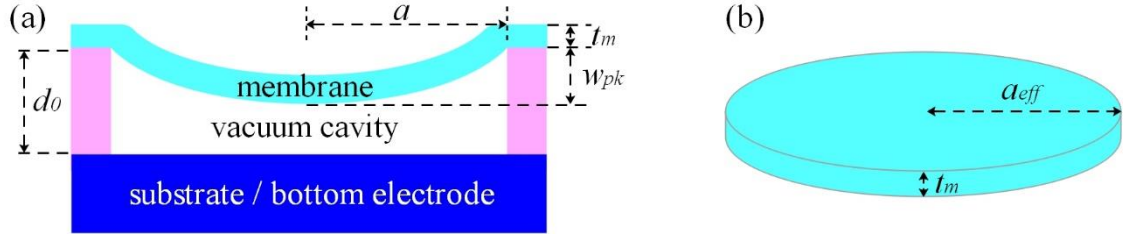
Fig. 3.2: CMUT with deformed membrane and equivalent plate: (a) CMUT; (b) equivalent plate.

As the membrane satisfies the thin plate condition $10 \leq 2a/t_m \leq 100$, where a is the membrane radius and t_m is the membrane thickness, the membrane deformation can be analyzed by thin plate theory [68]. Using the deflection shape function based on the plate theory, we can get the membrane deflection as [69]

$$w(r) = w_{pk}\left(1 - \frac{r^2}{a^2}\right)^2 = \frac{Pa^4}{64D_0}\left(1 - \frac{r^2}{a^2}\right)^2, \tag{3.1}$$

where r is the distance from the center, w_{pk} is the maximum displacement of the membrane, P is the uniform pressure that deflects the membrane. D_0 is described as

$$D_0 = \frac{Et_m^3}{12\left(1-\upsilon^2\right)}, \tag{3.2}$$

where E, t_m, and υ are the Young's modulus, thickness, and Poisson's ratio of the membrane material, respectively. It has been proved that the peak displacement w_{pk} equals to 46% of the CMUT gap height d_0 just before pull-in occurs, under the conditions that the deflection is small compared to the membrane thickness and the

atmospheric membrane displacement is negligible [69]. These simplifying assumptions are true with high-frequency devices. The near-pull-in instance is analyzed here because it is where the CMUT gets the highest efficiency [23]. In this case, the volume deflected by the membrane can be calculated as

$$V_{disp} = \int_0^a 2\pi r w(r) dr = \frac{1}{3} w_{pk} \pi A_m^2 = \frac{0.46 d_0}{3} \pi a^2,$$ (3.3)

where $A_m = \pi a^2$ is the area of the membrane.

For the equivalent piston-like plate, the pull-in occurs when the displacement is 1/3 of the gap height [23]. Hence the volume displaced by the plate is

$$V_{disp} = \frac{1}{3} d_0 A = \frac{1}{3} d_0 \pi a_{eff}^2,$$ (3.4)

where $A = \pi a_{eff}^2$ is the area of the equivalent plate. By equating (3.3) and (3.4), we can get the equivalent radius a_{eff} of the plate in the mass-spring-damper model

$$a_{eff} = 0.68\, a.$$ (3.5)

In addition to the equivalent radius, other parameters such as the spring constant k_s and equivalent mass m_s for the mass-spring-damper model are also obtained based on plate theory. The average displacement over the entire membrane is obtained to be 1/3 of the peak displacement:

$$w_{avg} = \frac{1}{A_m} \int_0^a 2\pi r w(r) dr = \frac{P a^4}{192 D_0} = \frac{1}{3} w_{pk}.$$ (3.6)

According to Hooke's Law, the linear spring constant k_s can be written as

$$k_s = \frac{F}{w_{avg}} = \frac{P \bullet \pi a^2}{w_{avg}} = \frac{192 \pi D_0}{a^2}.$$ (3.7)

The resonant angular frequency of the membrane can be derived by plate theory as [69]

$$\omega_0 = \frac{10.22}{a^2}\sqrt{\frac{D_0}{\rho_m t_m}}, \tag{3.8}$$

where ρ_m is the density of the membrane. The resonant angular frequency derived from the mass-spring-damper model is

$$\omega_0 = \sqrt{\frac{k_s}{m_s}}. \tag{3.9}$$

Combining Eq. (3.7) – Eq. (3.9), we can get the relationship between the mass of the equivalent plate m_s and the mass of the membrane m:

$$m_s = \frac{k_s}{\omega_0^2} = 1.84\pi a^2 t_m \rho_m = 1.84m. \tag{3.10}$$

According to Eq. (3.2) and Eq.(3.8), the resonance frequency in air for the clamped circular membrane can be written as

$$f_0 = \frac{\omega_0}{2\pi} = \frac{0.47t_m}{a^2}\sqrt{\frac{E}{\rho_m\left(1-\upsilon^2\right)}}. \tag{3.11}$$

It is quite straightforward that the resonance frequency of the membrane is proportional to the membrane thickness and inversely proportional to the square of the membrane radius.

When operated in immersion, where the diameter of the membrane is much smaller than the acoustic wavelength ($a \ll \lambda$) and the damping effect from the medium cannot be neglected, the resonance frequency of the membrane becomes [70]

$$f_0 = \frac{\dfrac{0.47t_m}{a^2}\sqrt{\dfrac{E}{\rho_m\left(1-\upsilon^2\right)}}}{\sqrt{1+0.67\dfrac{\rho a}{\rho_m t_m}}}. \tag{3.12}$$

where ρ is the density of the medium. It can be seen that the same membrane has a lower resonance frequency in immersion than in air.

After obtaining the parameters from plate theory, we can substitute them into the mass-spring-damper model. When a DC bias voltage V_{dc} is applied across the electrodes, an electrostatic force is generated to pull the membrane towards the substrate. Assuming no other external forces exist, the equation of plate vibrating motion can be expressed as

$$m_s \frac{d^2 x}{dt^2} + b \frac{dx}{dt} + F_s + F_e = 0, \tag{3.13}$$

where x is the displacement of the plate, b is the damping coefficient, F_s is the spring force, and F_e is the electrostatic force. At the equilibrium position, the first two terms become zero, and the spring force is balanced with the electrostatic force. The capacitance of the parallel plate capacitor is given by

$$C = \frac{A \varepsilon_0}{d_0 - x}, \tag{3.14}$$

where ε_0 is the permittivity of vacuum. The energy stored in the parallel plate capacitor is

$$W = \frac{C V_{dc}^2}{2} = \frac{\varepsilon A V_{dc}^2}{2(d_0 - x)}. \tag{3.15}$$

The electrostatic force exerted on the plate can be calculated as

$$F_e = -\frac{dW}{dx} = \frac{\varepsilon_0 A V_{dc}^2}{2(d_0 - x)^2}. \tag{3.16}$$

The spring force, which is also referred to as the mechanical restoring force of the plate, is linearly proportional to the displacement

$$F_s = -k_s x. \tag{3.17}$$

At the equilibrium state, Eq. (3.13) can be simplified as

$$F_s + F_e = \frac{\varepsilon_0 A V_{dc}^2}{2(d_0 - x)^2} - k_s x = 0. \tag{3.18}$$

From Eq. (3.18), the relationship between the voltage and the plate displacement is solved as

$$V_{dc} = \sqrt{\frac{2k_s x}{A\varepsilon_0}} \left(d_0 - x\right).$$ (3.19)

As the bias voltage increases, the electrostatic force will eventually overcome the mechanical restoring force, and the membrane will abruptly collapse into the substrate. The pull-in voltage (or collapse voltage) represents this transition voltage. The plate displacement x_{pi} at the collapse point can be found by equating the derivative of the voltage to zero ($dV_{dc}/dx = 0$) and is calculated as $x_{pi} = d_0/3$. By substituting the calculated displacement into Eq. (3.19), the pull-in voltage is obtained as [23]

$$V_{pi} = \sqrt{\frac{8k_s d_0^3}{27\varepsilon_0 A}} \ .$$ (3.20)

Note that the above calculations assume that the membrane is conductive and no insulation layer is introduced. In practical devices, an insulating layer such as SiO_2 and Si_3N_4 is deposited on the substrate and the membrane may be a non-conductive material with an extra metal electrode layer on top. Thus, the gap height d_0 between the top and bottom electrodes should be replaced by the effective gap d_{eff} in the above equations. The effective gap is given by [23], [71]

$$d_{eff} = d_0 + \frac{t_m}{\varepsilon_m} + \frac{t_i}{\varepsilon_i} ,$$ (3.21)

where t_m and ε_m are the thickness and relative dielectric constant of the membrane, t_i and ε_i are the thickness and relative dielectric constant of the insulating layer.

3.2 FEA Model

3.2.1   2D FEA Model
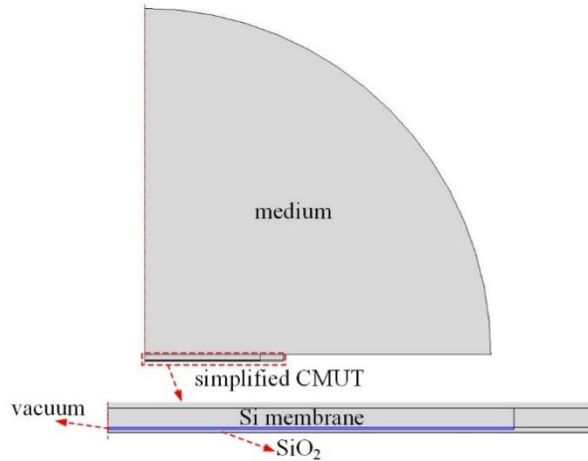
Fig. 3.3: FEM of the simplified CMUT with COMSOL.

In addition to the analytical model, the FEA model is also useful for analyzing CMUTs. The FEA model provides a more time-consuming yet a more accurate method for predicting the performance of CMUTs. COMSOL Multiphysics is used for the FEA simulation. Fig. 3.3 shows the axisymmetric 2D FEA model of a CMUT cell in the medium. The simplified 2D model consists of the silicon membrane, the vacuum cavity, and the silicon oxide insulating layer of the CMUT, and the medium. The substrate of the CMUT is omitted to reduce the computational complexity. Boundary conditions have been set to eliminate the effect of this simplification. The insulation layer is fixed and its bottom surface is grounded, as with the situation where the substrate exists. The diameter of the medium is set as three times the membrane diameter in the simulation. This size is determined as a compromise between the computational time and accuracy according to our previous experience in comparing the simulation results and experimental results. A

larger dimension of the medium will improve the calculation accuracy at a price of a longer computational time. Future research will seek to quantify the rate of change in accuracy with the increasing diameter of the medium.

The material properties used for FEA simulations are listed in Table 3.1. Unlike the well-studied silicon and SiO_2, GO has a very wide range of mechanical and dielectric properties depending on how it is produced. It is hence difficult to determine all the properties of GO from single literature. In the FEA simulations, its material properties are reasonably chosen from different resources [72]–[74].

Table 3.1 Material properties

Parameters	<100> Si	SiO2	GO
Young's modulus (GPa)	130	70	25
Poisson's ratio	0.28	0.17	0.28
Density (kg/m^3)	2329	2200	200
Relative permittivity	-	4.2	100

Table 3.2 Parameters of the simulated CMUT

Parameter	Value
Resonance frequency	10 MHz
Membrane thickness	2 μm
Membrane diameter	52 μm
Cavity depth	200 nm
Thickness of insulation layer	300 nm
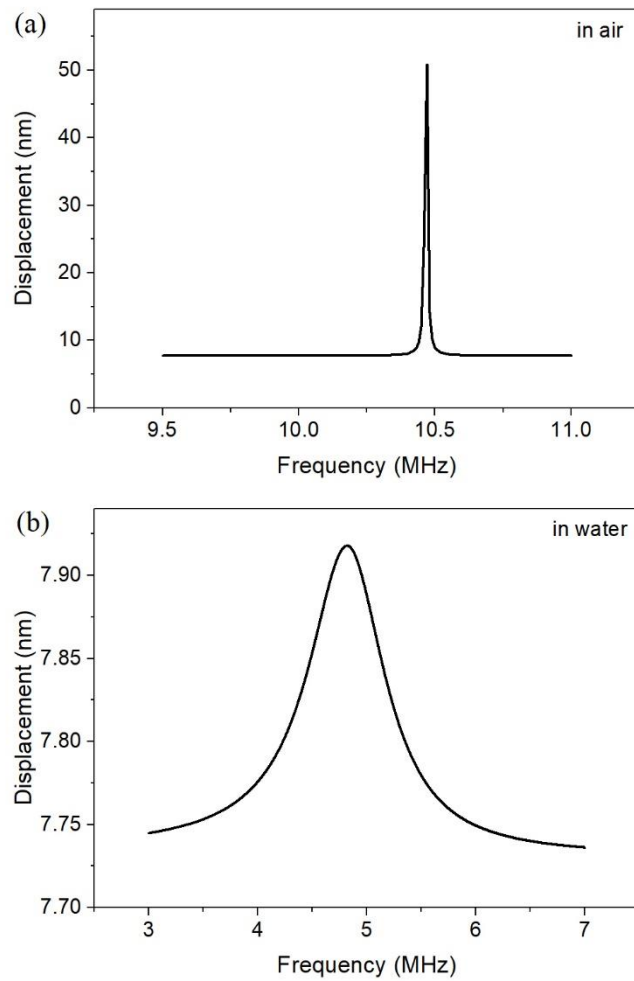
Fig. 3.4 Relationship between the maximum membrane displacement and the sweeping frequency:

(a) in air; (b) in water.

Here, a CMUT with ten MHz in-air resonance frequency is simulated. The design

parameters of the CMUT is listed in Table 3.2. Using a frequency sweep, the resonance

frequency of the CMUT is found where the membrane displacement reaches the

maximum. Under a bias voltage of 40 V, the simulated relationship between the

maximum membrane displacement and the sweeping frequency is shown in Fig. 3.4. Both

the in-air and in-water situations are analyzed. The resonance frequencies of the CMUT

are 10.47 MHz and 4.82 MHz when the medium is air and water, respectively, which

shows a good agreement with the analytical model calculations (10.81 MHz and 4.97 MHz, respectively). It is observed that when working in water, the CMUT has a much smaller membrane displacement, a lower resonance frequency, and a wider bandwidth. This is attributed to the higher damping in water.

3.2.2 Effect of Functional Layer

In order to investigate the resonating performance of the CMUT after functionalization, a GO layer is built on top of the membrane. The thickness of the GO film is determined to be 100 nm, which is much thinner than the membrane thickness, simulating practical situations. Essentially, the GO becomes a structural layer of the CMUT and vibrates simultaneously with the membrane. As the CMUT is targeted for humidity sensing in the room environment, only the in-air situation is simulated. Fig. 3.5 shows the simulated influence of the GO film on the CMUT. Fig. 3.5 (a) indicates that the GO film causes a decrease in membrane displacement and an increase in the resonance frequency. The lower resonating amplitude is due to the extra damping introduced by the GO layer. The influence on the resonance frequency is twofold. For one, the GO film adds to the effective thickness of the CMUT membrane, thus increases the resonance frequency. For another, it adds an extra mass to the membrane and hence decreases the resonance frequency. Which effect dominates the frequency shift mainly depends on the mechanical property and the dimension of the GO layer. In this simulation, the effect of the thickness increase overwhelms the effect of the mass loading and results in the rise of the resonance frequency. Fig. 3.5 (b) presents the 'spring softening effect'

of the CMUT. The resonance frequency decreases as the bias voltage increases. It can be

seen that the functionalized CMUT always has a higher resonance frequency than the

original device despite the change in the DC bias.
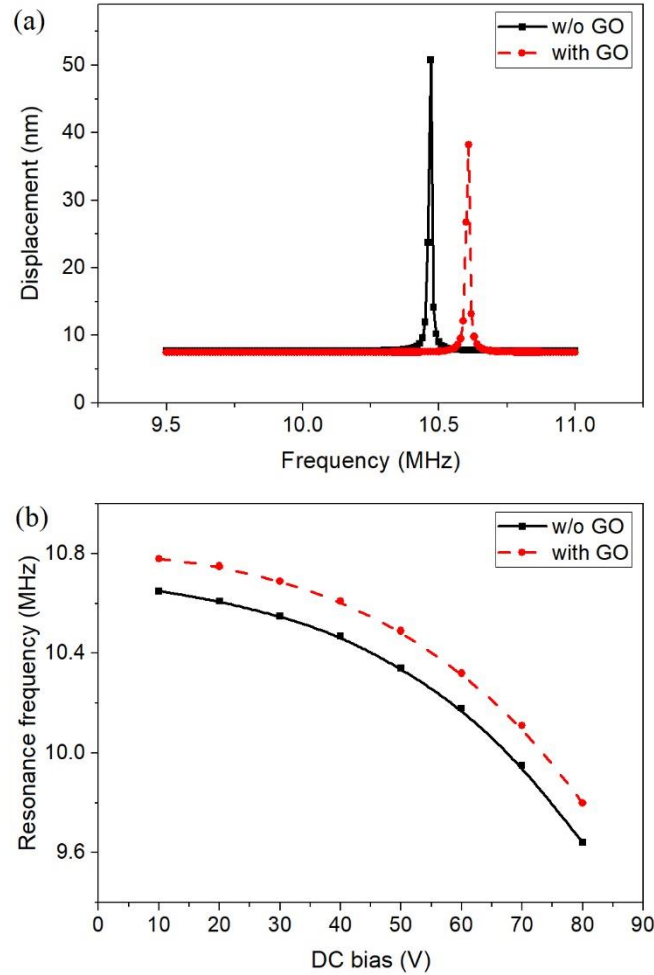
Fig. 3.5: Simulated influence of the GO film on the resonating performance of CMUT: (a)

membrane displacement vs. frequency; (b) resonance frequency vs. bias voltage.

3.2.3   Mass Sensitivity

The FEA model is also used to evaluate the mass sensitivity of the CMUT sensor.

The mass of the GO layer m_{GO} is calculated to be 0.04 ng, which is 0.43% of the mass

m of the Si membrane. Because the loaded mass on the membrane is generally much

smaller than *m* in practical sensing applications, only the small mass loading case ($\Delta m \ll m$) is analyzed. The loaded mass is simulated by increasing the density of the GO layer. The relative mass loading is defined as the multiples of m_{GO}. Fig. 3.6 presents the frequency shift as a function of the relative mass loading under various bias voltages. When increasing the relative mass loading from 0 to 10, the resonance frequency decreases for 224 kHz at a 10 V bias voltage, showing a mass sensitivity of 0.56 Hz/fg. As the bias increases from 10 V to 80 V, the mass sensitivity degraded slightly. This is because the membrane is more stringent at a higher bias and hence the extra mass causes a smaller frequency shift. Nonetheless, the effect of the bias voltage on the mass sensitivity is very small.
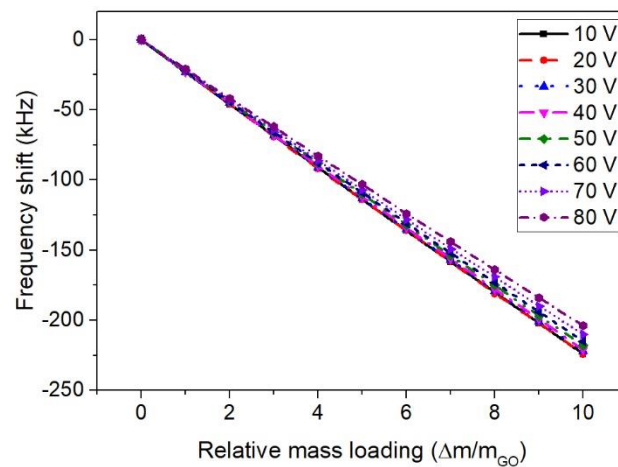
Fig. 3.6: Influence of the bias voltage on the mass sensitivity of CMUT sensor.

Chapter 4 Development of a Novel CMUT-based Concentric Dual-Element Ultrasonic Transducer

4.1 Revisiting Motivation

Ultrasound has been used for a wide range of applications including medical imaging and non-destructive testing (NDT). The core of an ultrasound imaging system is the ultrasound transducer, which transmits acoustic pulses into the medium and receives echoes for image reconstruction. While piezoelectric transducers are currently dominating the ultrasound market, CMUTs have emerged as a promising alternative in the last three decades [6], [8], [9], [23], [75]. CMUTs provide many advantages over piezoelectric transducers in both fabrication techniques and acoustic performance. In terms of fabrication, CMUTs have CMOS compatibility, the capability of building highly dense arrays, and flexibility of forming various sizes and shapes. Regarding the acoustic performance, CMUTs offer a wider bandwidth and a higher receive sensitivity.

Despite these attractive features, CMUTs inherently suffer from low output pressure due to the limited effective membrane and deflection areas [9]. Recent research showed that the overall sensitivity of CMUTs is 10 dB lower than the comparable piezoelectric transducer, mainly due to the inferior transmission performance [76]. Efforts have been made to increase the output pressure of CMUTs. About 6 dB increase in the transmit pressure was achieved by operating the CMUT in the collapse-snapback mode, in which

the CMUT membrane was collapsed onto the substrate and then released to maximize the volume displacement [77]. However, reliability issues can be a problem for the collapse-snapback mode due to frequent membrane and substrate contact [78]. Optimized CMUT geometry designs featuring improved fill factor and transmission efficiency, such as rectangular membrane configurations, have also been reported [79]. The dual-electrode CMUT structure, which separates the transmit and receive electrodes by locating the transmit electrodes near the edges and the receive electrode in the center, has demonstrated a 6.8 dB increase in the maximum output pressure [78]. CMUTs with piston-shaped membranes have also been developed to enhance both transmission and reception performance [80]. Added with an extra mass in the center of the membrane, piston CMUTs provide a more uniform membrane displacement and higher output pressure than conventional flat-membrane CMUTs. While more research is ongoing, the consensus is that CMUTs are currently not yet able to compete with piezoelectric transducers in term of transmission power, which limits CMUTs' performance in depth of penetration. This motivates us to find a solution that can harness the promising benefits of CMUTs while ensuring the overall sensitivity of the transducer.

In this chapter, a hybrid dual-element transducer, which incorporates a piezoelectric transducer and a CMUT element, is introduced. The dual-element prototype utilizes a commercial piezoelectric probe for ultrasound transmission and a custom CMUT for reception. As a result, high transmission power of the piezoelectric element and high

receive sensitivity of the CMUT are combined to provide enhanced overall sensitivity.

Moreover, improved axial resolution is achieved due to the wide bandwidth of the CMUT.

4.2 Sensor Design
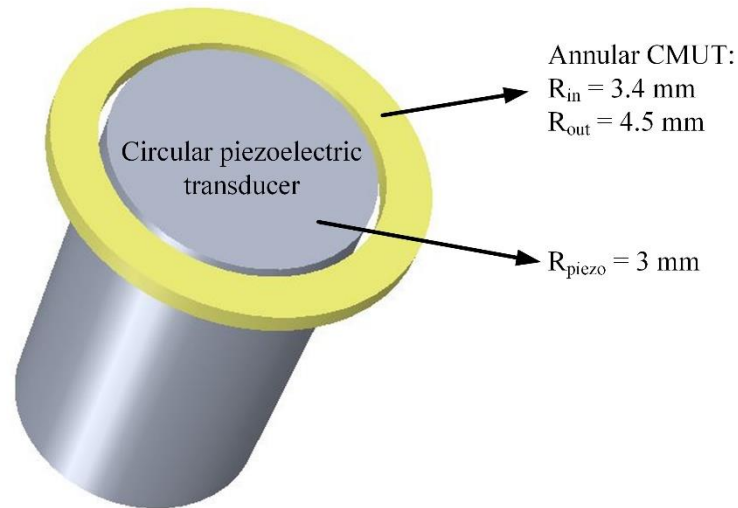
Fig. 4.1: Schematic of the concentrically aligned dual-element transducer.

Success in contrast-enhanced ultrasound imaging has been achieved with the

concentric dual-element design, which consists of a high-frequency (30 MHz) circular

and a low-frequency (2 MHz) annular piezo-based elements [81], [82]. We have chosen

to adopt a similar geometric layout largely due to the fact that this confocal configuration

provides identical beam axis and focal point between the transmitter and receiver [83].

As shown in Fig. 4.1, a circular piezoelectric transmitter and a ring-shaped CMUT

receiver were concentrically aligned and integrated. An unfocused 2.25 MHz 6 mm-

diameter commercial piezoelectric probe (Olympus I3-0204-S-SU) was selected as the

transmitter. 2.25 MHz is a commonly used frequency for both medical diagnosis (i.e.

abdominal imaging) and NDT. The smallest diameter available by the vendor, 6 mm, was

chosen to maximize the fabrication yield of the annular CMUT because smaller aperture

sizes are less susceptible to contaminations during the fabrication process.

Table 4.1 Dimensions of the annular CMUT

	Parameter	Value
Element	Inner radius	3.4 mm
	Outer radius	4.5 mm
Cell	Membrane diameter	76 μm
	Membrane thickness	2 μm
	Cavity depth	250 nm
	Thickness of insulation layer	250 nm

Based on the selected piezoelectric probe, the CMUT receiver was designed

accordingly. In order to achieve an optimal sensitivity, the intended natural focus and

resonance frequency of the CMUT element should be the same as those of the

piezoelectric element. The designed dimensions of the annular CMUT is shown in Table

4.1. The inner radius of the CMUT annulus was designed to be 3.4 mm to keep the two

elements close while also allowing a 400 μm tolerance for misalignment. The outer radius

was dependent on the desired natural focal depth, which was calculated to be 14 mm. A

well-established rule for annular arrays consisting of multiple concentric ring-shaped

elements was employed to determine the outer radius of the CMUT - elements with equal

areas share the same natural focus [84]. This rule should be valid for our case as the dual-

element design can be considered a two-element annular array. The outer radius was

designed to be 4.5 mm such that the CMUT had an area equivalent to the piezoelectric probe. Ultrasound beam simulations were performed using the fast object-oriented C++ ultrasound simulator (FOCUS) [85], [86]. Fig. 4.2 displays the simulated -8 dB and -17 dB pressure fields of both the circular and annular elements. The natural focus of both elements is 14 mm, which validates the design. The side lobes of the acoustic beams are highlighted in the figure. It can be observed that the annulus generates higher-level side lobes than the circular plate. Simulations show that the first side lobe level of the annulus is -8 dB, compared to -17 dB of the circular element. Associated with the side lobes are fluctuations in the acoustic signal, which will be discussed in the Results section.
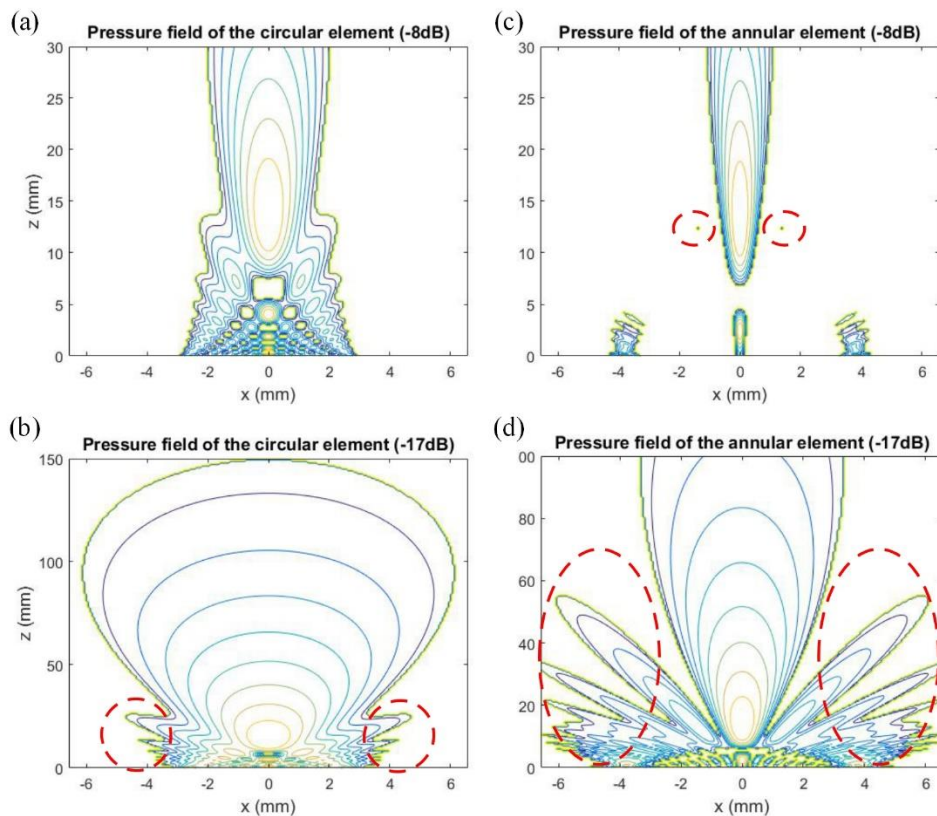
Fig. 4.2: Simulation of pressure profiles of the two elements with equal area: (a-b) circular element with a radius of 3 mm; (c-d) annular element with an inner radius of 3.4 mm and an outer radius of 4.5 mm.

The CMUT cells that comprise the annular element were designed to resonate at around 2.25 MHz. The membrane of the CMUT came from the silicon device layer of an SOI wafer. Based on the availability of commercial SOI wafers, a 2 µm-thick membrane was chosen. Given the resonance frequency, the membrane radius of the CMUT cell was determined to be 38 µm via FEA simulations. The cavity depth was designed to be 250 nm for the CMUT to operate in the non-contact mode. The thickness of the insulating layer was a trade-off between the sensitivity and dielectric breakdown voltage. A thinner insulating layer is desired for better sensitivity, while a sufficient thickness is required to avoid breakdown of the device. The insulating wet thermal silicon dioxide was grown in our facility with a dielectric strength of around 300 V/µm [87]. Its thickness was selected to be 250 nm. Consequently, the breakdown voltage was around 75 V, which was safe for the CMUT to be biased within 60 V.

4.3 Sensor Fabrication
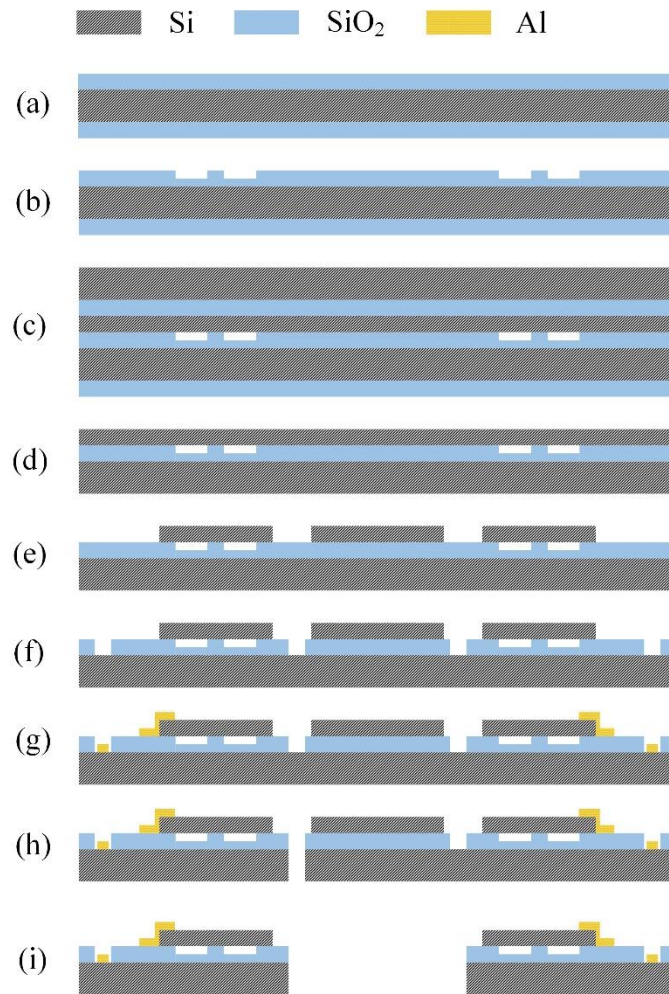
Fig. 4.3: Fabrication flow of the annular CMUT.

The CMUT was fabricated pursuant to the direct wafer bonding process, followed by a singulation process for the annulus. The wafer bonding process was selected due to its exceptional yield, uniformity and process control [38]. Fig. 4.3 depicts the detailed process flow of the annular CMUT. The fabrication process started with a 100-mm 0.001-0.005 ohm-cm <100> silicon wafer, which later served as both the substrate and the bottom electrode. A 500 nm layer of wet thermal oxide was grown on the bottom wafer at 1100 °C (step a). The 250 nm deep cavities were patterned using a photolithography

step and RIE (step b). Next, a 100 mm 0.01-0.02 ohm-cm <100> SOI wafer with a silicon device layer thickness of 2 μm was prepared for wafer bonding with the bottom wafer. The thicknesses of the BOX layer and the handling layer are 0.6 μm and 500 μm, respectively. Before the wafer bonding process, a standard RCA 1 cleaning (based on 5 parts deionized water, 1 part 27% ammonium hydroxide and 1 part 30% hydrogen peroxide) [88] was performed on both the SOI wafer and the patterned bottom wafer to remove organics and particles on the wafer surfaces. Direct fusion bonding (AML AWB-04 aligner wafer bonder) was conducted between the two wafers at a 2500 N downward force after a 10-minute plasma treatment (step c). The bonded wafer pair was then annealed at 1100 °C for an hour to enhance the bonding strength. While the bottom silicon substrate was protected by the thermally grown oxide, the top silicon handling layer was removed through TMAH etching, followed by wet-etching of the BOX layer with BHF (step d). Subsequently, the silicon device layer was patterned and etched with DRIE to create isolation trenches between the devices (step e). Another purpose of this step was to partially reveal the bottom electrodes for interfacing and open a 200 μm-wide annular via for singulation of the annulus. Next, a lithography patterning and oxide RIE step is made to fully expose the bottom electrodes and the annular via (step f). A 400 nm-thick aluminum electrode layer was then deposited by sputtering, followed by a lift-off process to form the metal contact pads (step g). At this point, the CMUT device was produced. The next step was to create the central hole for the packaging. Silicon DRIE (Oxford PlasmaLab 100 ICP 380 DRIE system) was used to through etch the substrate (step h).

The Bosch process [89], popular for its capability of creating vertical sidewalls, was chosen for DRIE.

The through-wafer etching process was one of the most critical and challenging steps in the fabrication, making selection of the DRIE mask material crucial. We took into account the device compatibility and fabrication yield/risk. Two layers of masks were chosen - a 50 nm sputtered Cr layer and an 11 μm-thick photoresist layer atop (Electronic Materials plc AZ9260). In addition to the function as a mask, the thick photoresist was also used to pattern the underlying Cr. Both Cr and the photoresist offered high selectivity over silicon (Si : photoresist ≈ 40 : 1, Si : Cr > 2000 : 1) and protected the devices from ion bombardment in the DRIE process. After the through-wafer etching process, the photoresist was completely bombarded away. Then, the Cr mask was removed by wet etching. Fig. 4.4 (a) shows the through-etched CMUT. Note that three asymmetric tethers with a width of 100 μm were designed to maintain connections between the annular CMUT and the central substrate (see Fig. 4.4 (b)). The tethers prevented the central substrate from falling into the plasma chamber. Finally, the central circular substrate was manually removed with a tweezer, as shown in Fig. 4.4 (c).
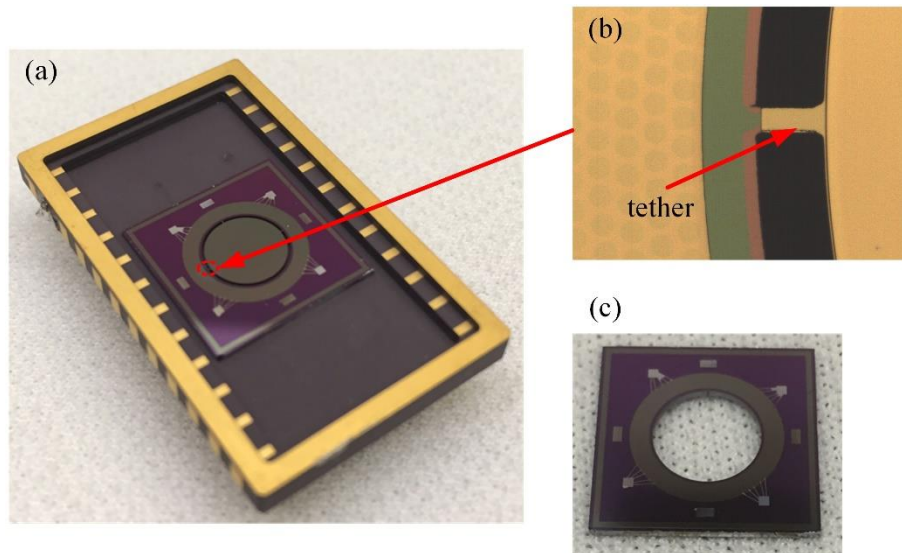
Fig. 4.4: Through-etched CMUT: (a) CMUT on a chip carrier; (b) magnification of the tether; (c)

annular CMUT with central substrate removed.

4.4 Device Characterization

A Laser Doppler Vibrometer (Polytec OFV-5000, DD-300 displacement decoder) was used to test the functionality and the in-air resonance frequency of the CMUT. Using a frequency sweep with a function generator (Tektronix AFG3022B), the in-air resonance frequency of the CMUT was determined by measuring where the maximum membrane displacement occurred. Given a 50 V bias and a 10 Vpp AC continuous sinusoidal signal, the CMUT reached the in-air resonance at 5.15 MHz with a maximum displacement of 50 nm.
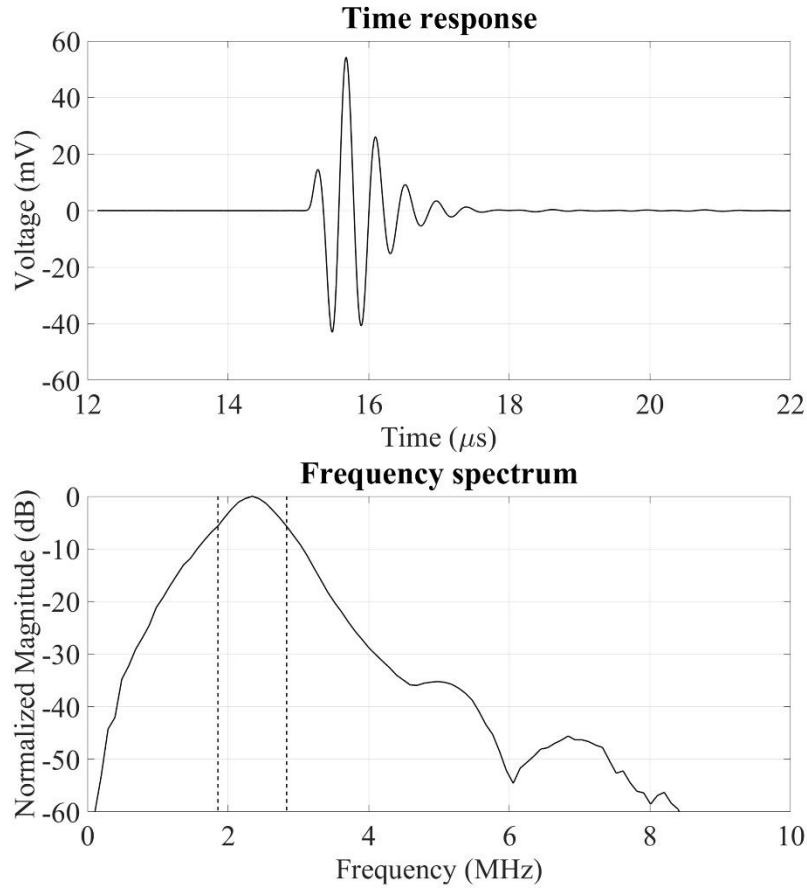
Fig. 4.5: Hydrophone measurement and frequency spectrum of the piezoelectric probe: the center

frequency is 2.34 MHz and the -6dB bandwidth is 42%.

Transmission test: To study the immersion performance of the CMUT and the

Olympus piezoelectric element, both the transmission and reception tests were carried

out in vegetable oil, which provided electrical insulation between the electrodes of the

CMUT. The transmission performance of the piezoelectric probe was first characterized

to analyze the output pressure and the frequency spectrum. A pulser/receiver

(Panametrics NDT 5073PR) was used to drive the probe. The acoustic signal was picked

up by a hydrophone (Onda HGL-0200), which was placed at 22 mm away from the

transducer and connected to a digital oscilloscope (Agilent DSO7104B) through a pre-

amplifier (Onda AH-2010). The hydrophone was aligned to the center of the piezoelectric probe by adjusting its position to achieve a maximum receiving signal amplitude while keeping it 22 mm away from the probe. Fig. 4.5 shows the acoustic output captured by the hydrophone in both the time and frequency domain. Using the sensitivity of the hydrophone-pre-amplifier combination provided by the manufacturer (0.322 mV/kPa), the output pressure of the transducer was calculated to be 302 kPa according to the maximum peak-to-peak output voltage. The center frequency and the -6 dB fractional bandwidth of the probe, determined from the frequency spectrum, were 2.34 MHz and 42%, respectively. Note that the measured center frequency and bandwidth were very close to that provided by the manufacturer, which were 2.24 MHz and 43%, respectively. Then, the transmission test of the CMUT was conducted under the same conditions as the piezoelectric probe. The CMUT was biased at 20 V. Fig. 4.6 depicts the CMUT output signal in both time and frequency domain. The output pressure was measured to be 68 kPa. The frequency spectrum revealed a center frequency of 2.63 MHz and a -6 dB bandwidth of 131%. The measured center frequency of the CMUT was slightly higher than the predicted value (2.25 MHz). We hypothesize that the frequency difference resulted from the thickness uniformity of the membranes because there was an up to 0.5 μm thickness variation in the device layer of the commercial SOI wafer. Comparison of the transmission tests between the piezoelectric probe and the CMUT is presented in Table 4.2. Compared to the piezoelectric transducer, the CMUT has approximately triple the bandwidth and one-fifth the output pressure. It can also be observed that the -6 dB

frequency range of the CMUT completely covers that of the piezoelectric probe. In other

words, the frequency spectrums of the two transducers excellently matched as designed.
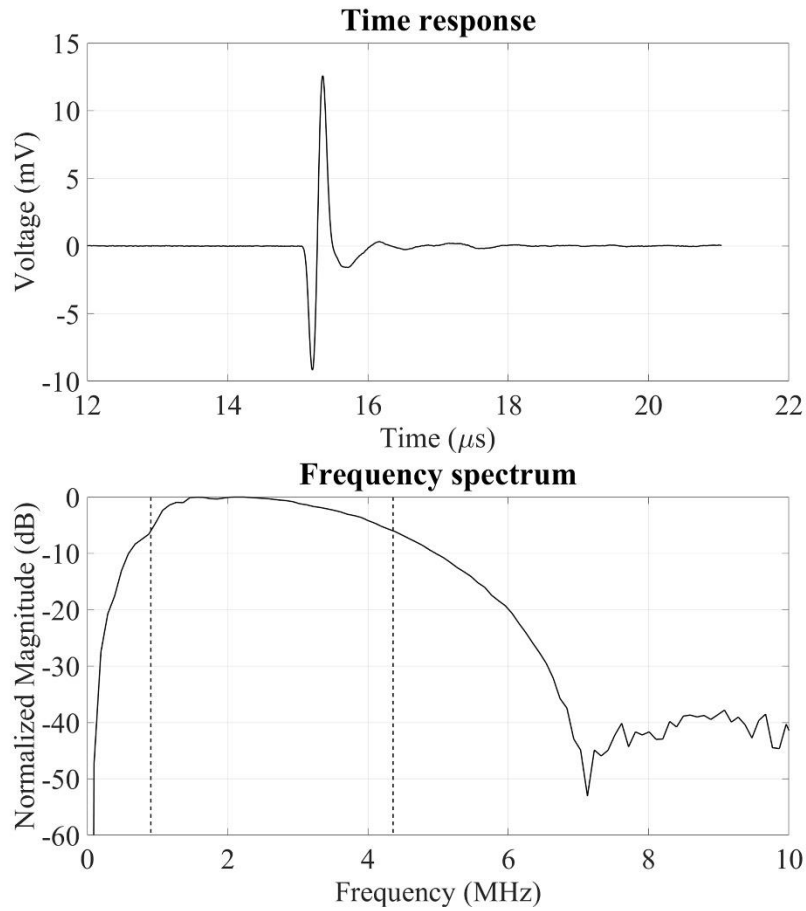
Fig. 4.6: Hydrophone measurement and frequency spectrum of the CMUT: the center frequency is

2.63 MHz and the -6dB bandwidth is 131%.

Table 4.2 Comparison between the piezoelectric probe and the CMUT in the pitch-catch tests

Parameters	Piezoelectric probe	CMUT
Center frequency (MHz)	2.34	2.63
-6 dB bandwidth	42%	131%
Output pressure (kPa)	302	68
Receive sensitivity (mV/kPa)	4.28	22.57

Reception test: To characterize the receive sensitivity of the two elements, a 6 mm-diameter circular CMUT which was fabricated in the same batch with the annular CMUT, was used for ultrasound transmission. First, the output pressure of the circular CMUT was characterized with the hydrophone placed 22 mm away. When the circular CMUT was biased at 20 V and excited by the same pulser as in the above transmission test, the output pressure of the pre-amplifier was measured to be 65 kPa. Note that the circular CMUT generated a very similar acoustic signal to that of the annular CMUT. Its center frequency and the -6 dB bandwidth were measured to be 2.59 MHz and 122%, respectively. Then, the Olympus piezoelectric transducer, which was connected to the oscilloscope through the pulser/receiver (Panametrics NDT 5073PR), was substituted in lieu of the hydrophone for ultrasound reception. Fig. 4.7 shows the ultrasound signal detected by the piezoelectric probe. The maximum peak-to-peak output voltage of the pulser/receiver was determined to be 278 mV, which translated to a receive sensitivity of 4.28 mV/kPa. Subsequently, the Olympus probe was replaced by the annular CMUT biased at 20 V. The incident acoustic signal to the CMUT induced a current and was converted to a voltage using a transimpedance amplifier with a gain of 20 kΩ. The CMUT captured signal is presented in Fig. 4.8. The maximum peak-to-peak output voltage of the amplifier was measured as 1.467 V. Accordingly, the receive sensitivity of the CMUT-transimpedance amplifier combination was calculated to be 22.57 mV/kPa.
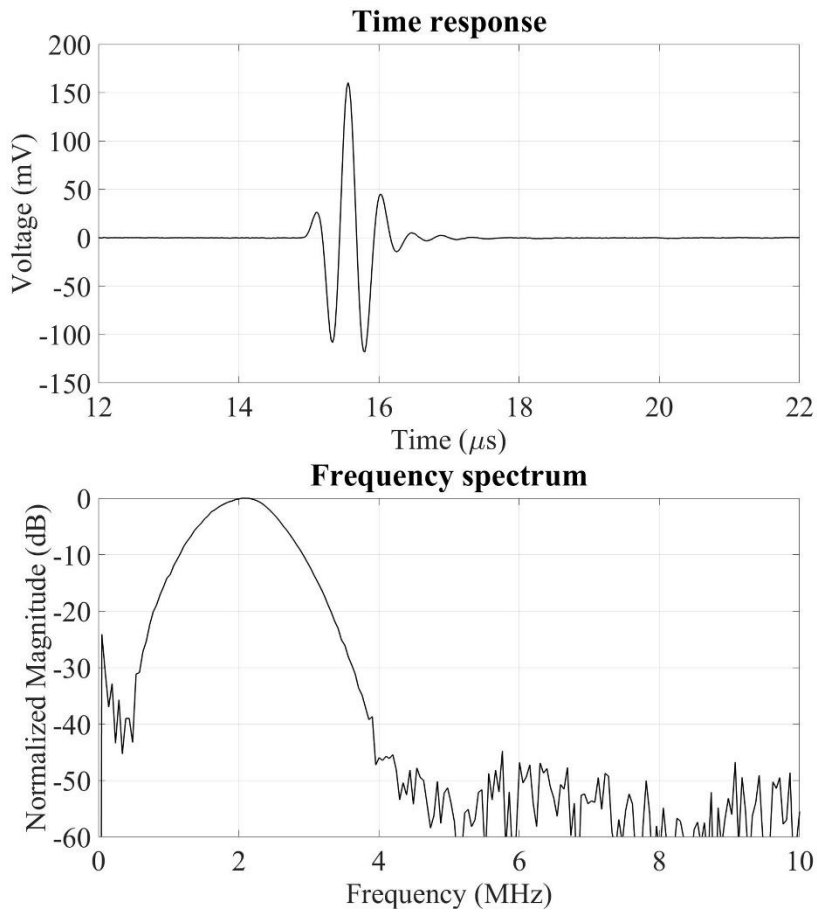
Fig. 4.7: Reception test using a 6 mm - diameter circular CMUT for ultrasound transmission: acoustic

signal detected by the piezoelectric probe in both time domain (top) and frequency domain (bottom).
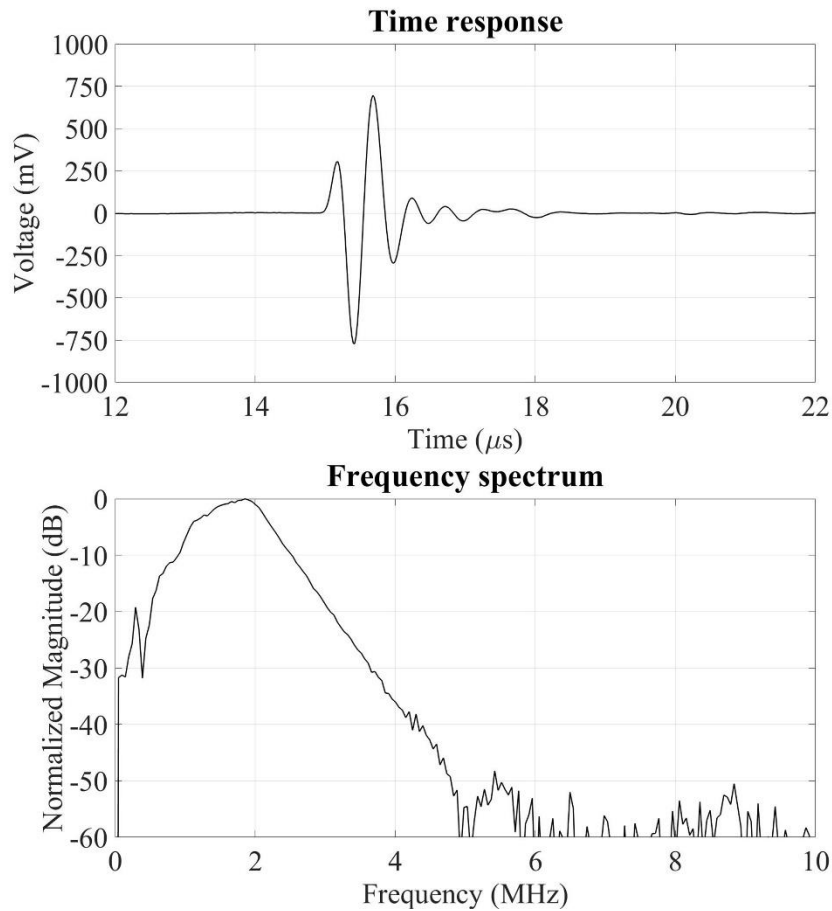
Fig. 4.8: Reception test using a 6 mm - diameter circular CMUT for ultrasound transmission: acoustic signal detected by the annular CMUT in both time domain (top) and frequency domain (bottom).

4.5 Results

The round-trip (transmit and receive) measurements of the Olympus piezoelectric probe and the integrated piezo-CMUT dual-element prototype were performed for comparison.
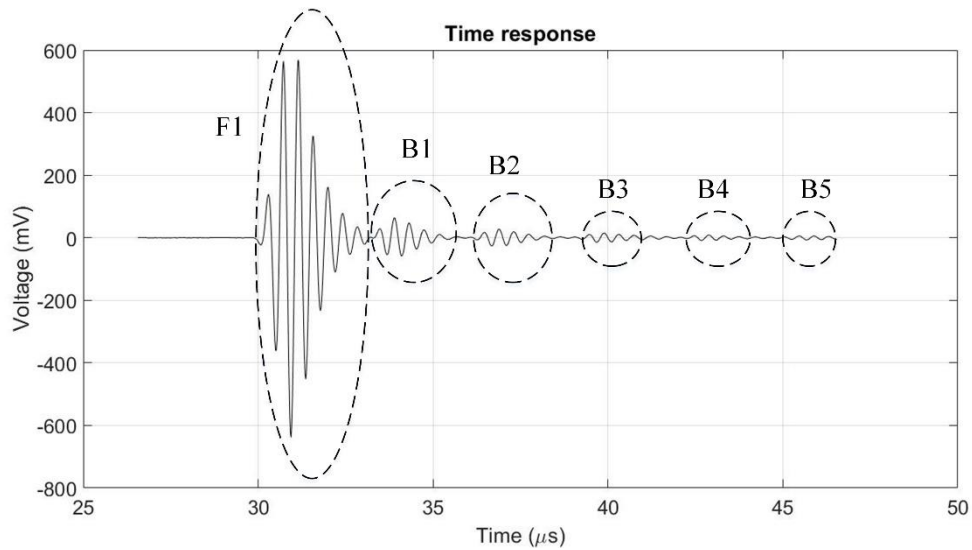
Fig. 4.9: Pulse-echo test of the piezoelectric transducer.

Piezo-only test: The piezoelectric transducer was first tested. A 9.5 mm-thick aluminum reflector was placed 22 mm away from the transducer. The same pulser/receiver was used to excite the piezoelectric transducer and feed the echo to the digital oscilloscope. Fig. 4.9 shows the signal reflected from the aluminum block and received by the piezo probe. F1 and B1 represent the interface echo (or front wall echo) and backwall echo, respectively. B2-B5 are the second to fifth backwall echoes which have been reflected within the test block. Two successive backwall echoes represent a round trip in the block.
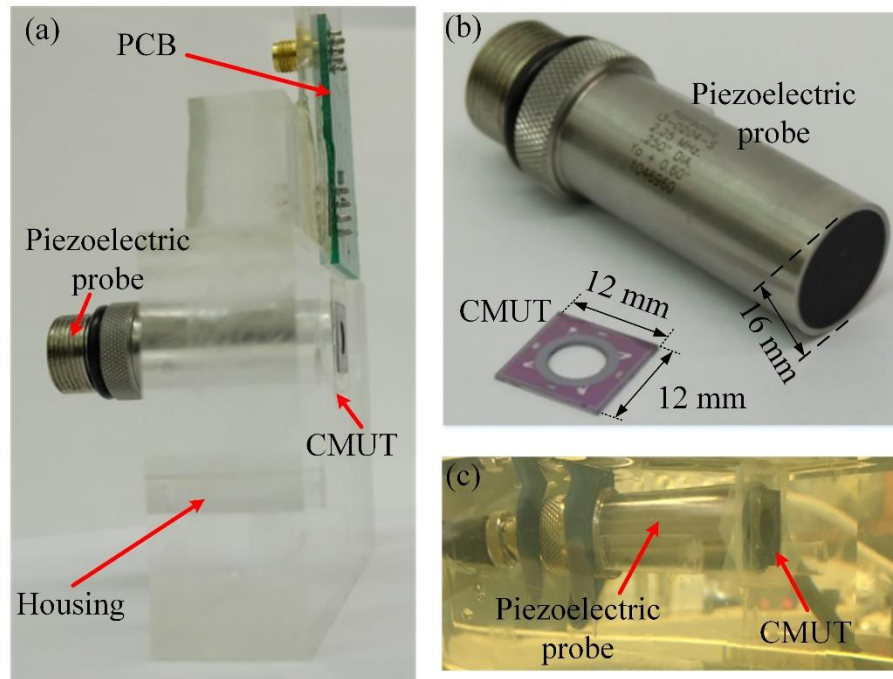
Fig. 4.10: Integration of the CMUT and the piezoelectric probe (a) photograph of the integrated dual-element prototype (b) transducers before integration (c) the hybrid transducer in oil.

Piezo-transmit-CMUT-receive test: The piezoelectric probe was then integrated with the annular CMUT via a custom plastic housing, as shown in Fig. 4.10. The CMUT was mounted on the trough on the front side of the laser-graved housing, while the piezo probe was inserted in the hole from the back side. Note that there was a 1.6 mm gap between the surface of the piezo probe and the CMUT resulting from the thicknesses of the CMUT and the housing. Although ideally the two elements should be seamlessly integrated, the 1.6 mm gap was negligible compared to the -6 dB depth of field of the transducers (approximately 35 mm calculated from Fig. 4.2). After integration, the CMUT was wire bonded to the circuit board for external electrical connections. Next, the round-trip experiment was performed with the piezo-CMUT hybrid prototype. The hybrid transducer was immersed in oil, with the same aluminum reflector 22 mm away. The

pulse applied to the piezoelectric transmitter remained unchanged. The CMUT was biased at 20 V and connected to the oscilloscope through the transimpedance amplifier. The piezo-transmitted ultrasound was reflected by the aluminum block and received by the CMUT. Fig. 4.11 presents the received echo.
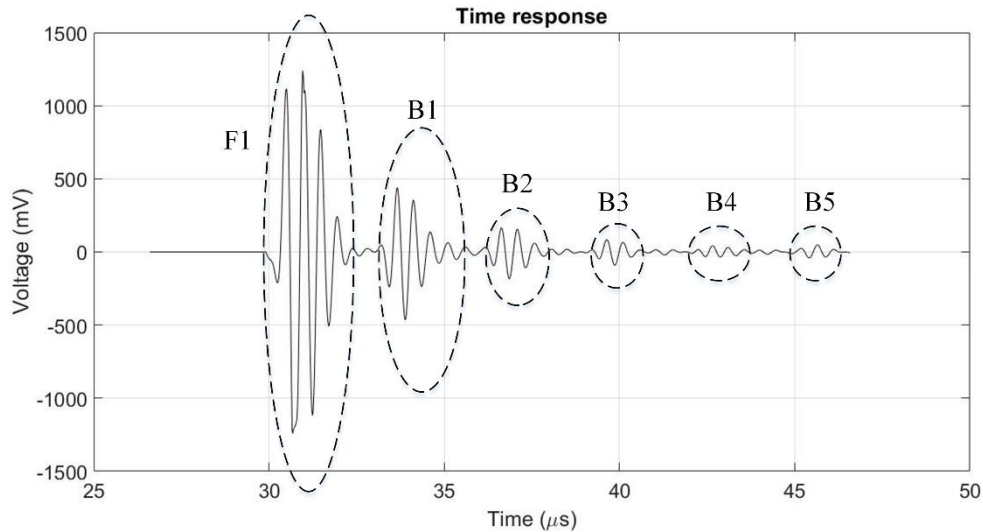
Fig. 4.11: Measurement for the piezo-transmit-CMUT-receive test.

Table 4.3 Comparison between the piezo-only and the piezo-transmit-CMUT-receive measurements

Parameters	Piezo-only	Piezo-transmit-CMUT-receive
-20 dB pulse length of F1 (µs)	2.26	1.68
SNR (dB)	15.08	23.63

Quantitative comparison between the piezo-only and the piezo-transmit-CMUT-receive measurements are presented in Table 4.3. The -20 dB pulse length (pulse length where the output pressure is 10% of the maximum) of F1 reflects the axial resolution of the detection. A shorter pulse length indicates a higher axial resolution. The CMUT-involved measurement showed a pulse length of 1.68 µs and a 25.58% enhancement over

the piezo-only test. The round-trip sensitivity was compared using the signal-to-noise ratio (SNR). The piezo-only experiment measured an SNR of 15.08 dB, while the piezo-transmit-CMUT-receive test showed an improvement of 8.55 dB.

In addition to the improved axial resolution and sensitivity, undesired signal fluctuations were observed with the dual-element prototype. In particular, the amplitude of the fifth backwall echo B5, which was supposed to be the lowest among all those of the backwall echoes due to acoustic attenuation, was calculated to be 15% higher than that of B4 (see Fig. 4.11). The variation was possibly induced by the side lobes of the annular CMUT, which corresponds to the simulation results in the Method section. A reasonable explanation is that the chance of picking up interfering signals by the side lobes increases as the acoustic signal reflects within the aluminum block several times. Side lobes are known to be inevitably higher for annular transducers than circular ones [90]. However, it is possible to suppress them by several strategies such as reducing the ratio of the inner radius to the outer radius of the annular transducer [91].

4.6 Summary

To address the limitation of CMUTs' low output pressure, a hybrid dual-element ultrasonic transducer was proposed. It incorporated two transducer technologies by using a circular commercial piezoelectric element for ultrasound transmission and an annular CMUT element for reception. To the best of our knowledge, this is the first-ever reported integration of the piezoelectric transducer and the CMUT. The hybrid transducer

combined the broad bandwidth and high receive sensitivity of the CMUT and the high output pressure of the piezoelectric transducer to improve the overall sensitivity and axial resolution. The annular CMUT was designed, fabricated, and concentrically aligned with the piezoelectric probe via a custom housing. Immersion characterization revealed that the CMUT had a center frequency of 2.63 MHz, a -6 dB fractional bandwidth of 131%, and a receive sensitivity of 22.57 mV/kPa, compared to 2.34 MHz, 42% and 4.28 mV/kPa of the piezoelectric probe. The round-trip measurements showed that the hybrid dual-element transducer improved the axial resolution by 25.58% and the SNR by 8.55 dB over the commercial piezoelectric probe. Potential applications of this hybrid transducer include, but are not limited to, detection of pipeline cracks and the delamination of aircraft structures.

Chapter 5 Development of a Highly Sensitive CMUT-based Humidity Sensor

5.1 Revisiting Motivation

CMUTs have been proven to be a promising bio/chemical platform in the last decade. Compared to other gravimetric-based sensors, their advantages include high mass sensitivity, reliability, miniaturization, ease of functionalization, and capability of selective sensing. However, their potential for humidity sensing is less explored. In 2012, Lee et al. applied a 50 MHz CMUT to detect water vapors using mesoporous silica thin film as the sensing material. A sensitivity of 2 kHz/%RH was reported in an RH range of 0% to 80% [92]. In 2014, this group developed a multichannel oscillator for the sensing system and improved the RH sensitivity to 2.6 kHz/%RH between an RH level of 0% to 20% [13]. It is well known that the mass sensitivity of a resonant gravimetric sensor is determined by both the transducer itself and also the sensing material. In the recent decade, GO has been emerging as a superior material for moisture sensing due to its excellent hygroscopic property and low cost. It has been widely adopted for other types of gravimetric sensors like QCMs [42]–[44] and SAW sensors [17].

In this chapter, a CMUT-based humidity sensor functionalized with GO is introduced. The objective is to demonstrate the efficiency of combining the mass-sensitive CMUT and the moisture-sensitive GO. The CMUT humidity sensor is designed and fabricated

with microfabrication techniques and coated with a GO thin film. The analysis on the sensitivity, the repeatability, the response/recovery time, and the hysteresis characteristics are presented to prove that the CMUT humidity sensor can serve as a strong candidate for humidity sensing.
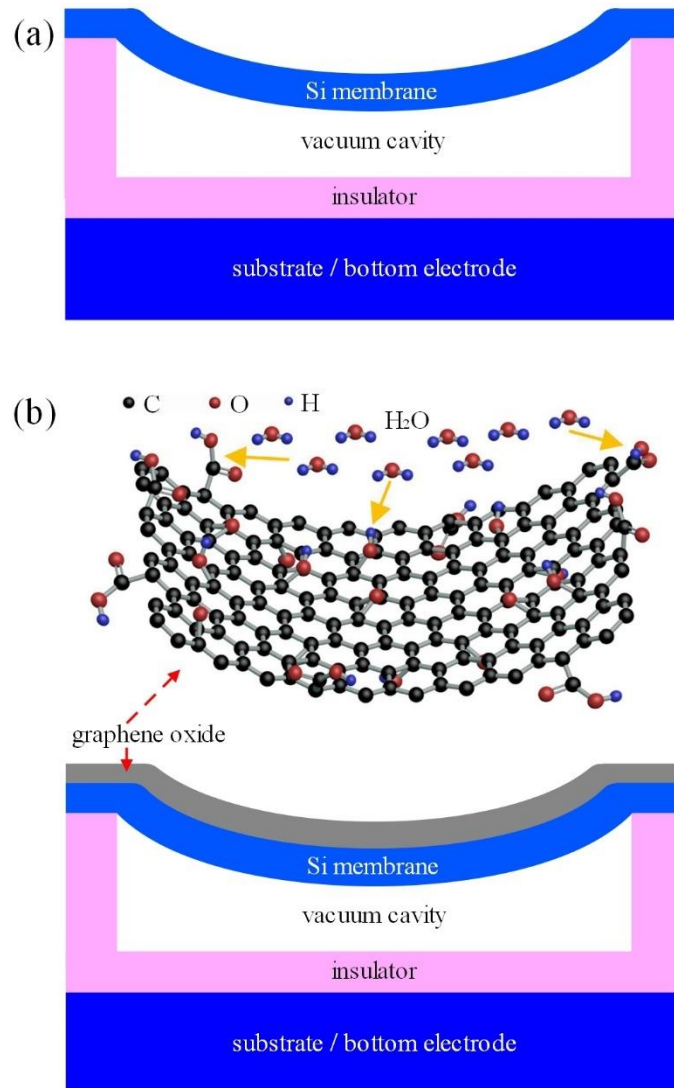
Fig. 5.1: Schematic of (a) CMUT structure; (b) working mechanism of the CMUT humidity sensor.

5.2 Operational Principle and Design

As shown in Fig. 5.1 (a), a basic CMUT cell structure is a parallel-plate capacitor with a vacuum cavity in between and the resonating membrane anchored around. Superimposed by a DC voltage, when an AC voltage is applied across the two plates, the membrane vibrates. The vibration amplitude is maximized as the frequency of the AC voltage equals the resonance frequency of the CMUT. For a CMUT with circular membranes, the resonance frequency is determined by Eq. (3.11).

After coating of the GO thin film, a resonance frequency shift of the CMUT is expected. Whether the shift is positive or negative mainly depends on the mechanical property and the dose of the GO. As depicted in Fig. 5.1 (b), the working principle of the CMUT humidity sensor is based on the mass-loading effect, where the additional mass of water molecules loaded on the GO film causes a resonance frequency shift. If the added mass is small compared with the mass of the membrane, the mass sensitivity can be expressed as [32]

$$S = \frac{\partial f}{\partial m} = -\frac{1}{2}\frac{f_0}{m} \propto \frac{1}{a^4} \, . \tag{5.1}$$

According to Eq. (5.1), a higher mass sensitivity requires a higher resonance frequency and a lower mass, both of which can be achieved by a smaller radius. However, given a membrane thickness, the radius is limited by the fabrication capabilities and the SNR level when the resonance frequency becomes impractically high. Therefore, both

the performance and practical conditions need to be considered while designing the CMUT humidity sensor.

A circular CMUT with a diameter of 2 mm was designed to facilitate the deposition of the GO thin film. A single sensor contains 850 CMUT cells. The resonance frequencies of the reported CMUTs for gravimetric detection range from 1.8 MHz to 50 MHz [11], [12], [14]. In this work, the in-air resonance frequency of the CMUT was moderately designed to be around 12 MHz as a compromise between the mass sensitivity and the fabrication yield. A thinner membrane is usually desired for a higher mass sensitivity due to its lighter weight. Here, the thickness of the membrane was selected as 2.2 μm depending on the availability of SOI wafers. Using the FEA simulation, the radius of the membrane and the cavity depth were determined to be 26 μm and 250 nm according to the selected resonance frequency and membrane thickness.

5.3 Sensor Fabrication
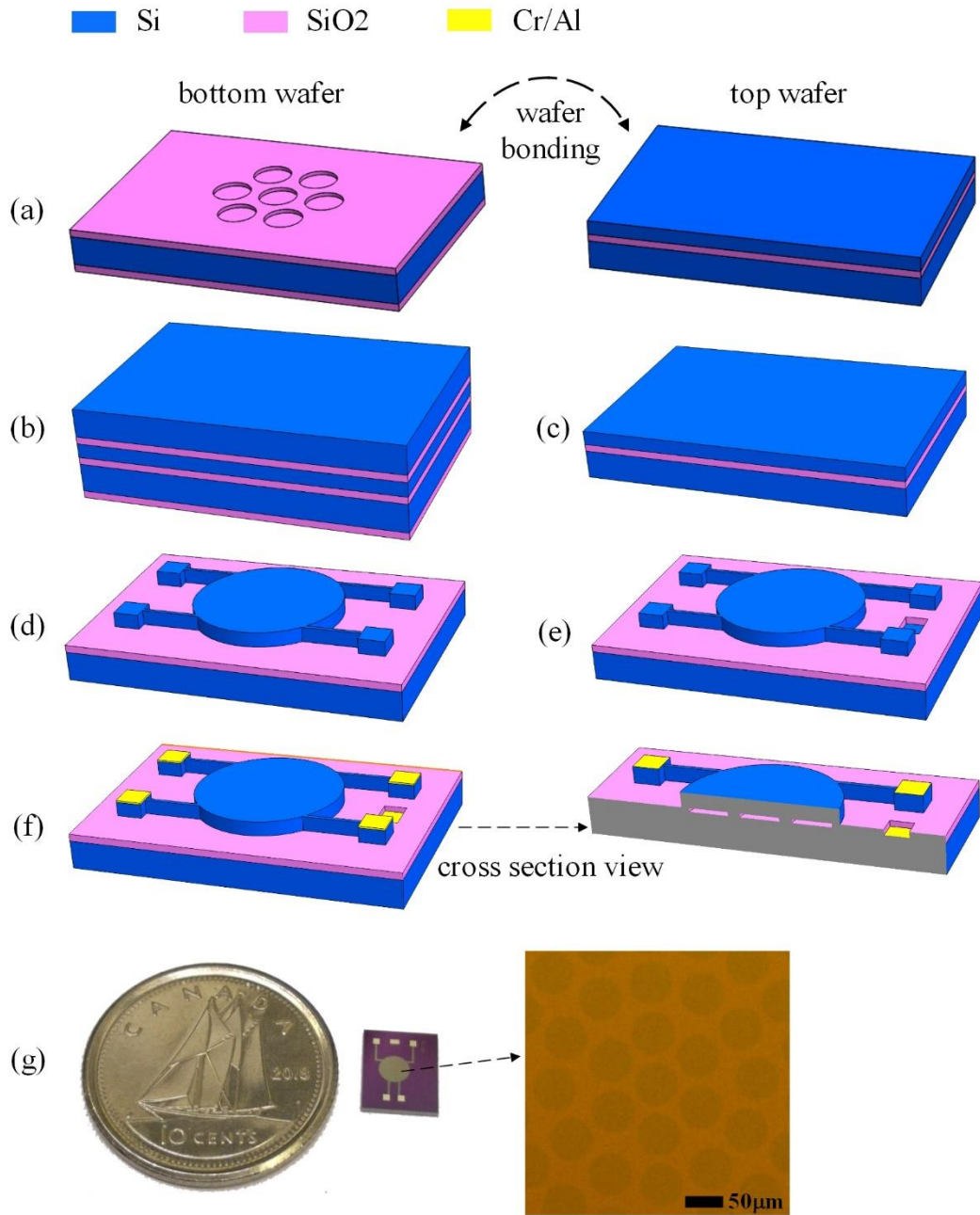
Fig. 5.2: Process flow of the CMUT.

The CMUT was fabricated using the direct wafer bonding process. Fig. 5.2 depicts

the process flow. The fabrication started from a 100 mm 0.001-0.005 ohm-cm < 100 >

prime silicon wafer, which was grown with a 500 nm SiO_2 layer by wet thermal oxidation.

In step (a), the oxide layer on the substrate was patterned and etched with cavities. Then a 100-mm 0.001-0.005 ohm-cm < 100 > SOI wafer with a device layer thickness of 2.2 μm was prepared for wafer bonding. An RCA-1 cleaning was done on both the bottom wafer and the SOI wafer before the bonding to ensure the surface cleanness and also render the wafer surfaces hydrophilic. Then the wafers were bonded in vacuum after a 10-minute plasma treatment (step b). In step (c), the CMUT membrane was released by removing the handling layer and the BOX layer. Then, the membrane was patterned and etched with DRIE to define the CMUT elements (step d). Subsequently, the bottom electrode was exposed through a lithography patterning and RIE etching step (step e). In step (f), a 30 nm chromium and 100 nm aluminum bi-layer electrode was deposited using e-beam evaporation, followed by a lift-off process to form the metal contact pads. The fabricated CMUT is displayed in Fig. 5.2 (g).

The 1 mg/mL GO dispersion was prepared by dispersing the commercial GO powder with DI water and then treating it with ultrasonic bath for an hour. To functionalize the CMUT, 5 μL of GO dispersion was drop-casted on the CMUT membrane using a microliter syringe. The GO thin film was formed after the water was evaporated in room temperature. Since multilayer GO is a metastable material [93], the sensor was kept in room temperature for three weeks until its structure and chemistry properties became stable.

5.4 Apparatus
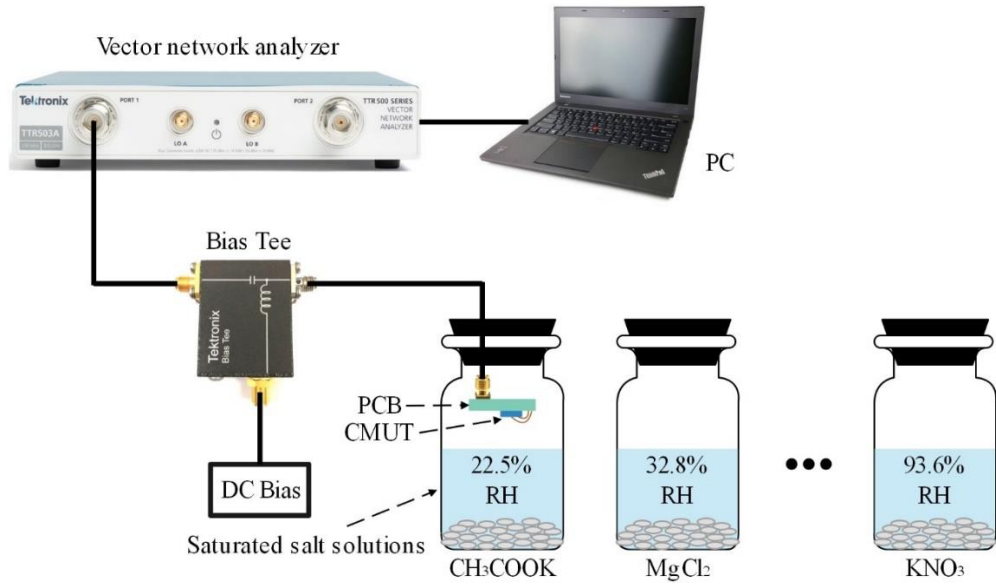
Fig. 5.3: Schematic diagram of the humidity sensing experimental setup.

Fig. 5.3 shows the schematic diagram of the experimental setup. Note that all the measurements were performed at the room temperature (~25 °C). Saturated salt solutions were used to generate different levels of RH. Potassium acetate (CH₃COOK), magnesium chloride (MgCl₂), potassium carbonate (K₂CO₃), sodium chloride (NaCl), potassium chloride(KCl), and potassium nitrate (KNO₃) provided an RH of 22.5%, 32.8%, 43.2%, 75.3%, 84.3%, and 93.6%, respectively [94]. Via a bias tee (PSPL5530B, Tektronix), the CMUT humidity sensor was biased by a DC power supply (GPR-11H30D, GW Instek) and excited by the vector network analyzer (VNA). The VNA (TTR503a, Tektronix) was used to measure the S_{11} parameters [95] of the CMUT humidity sensor at each RH level, which were converted into electrical impedances for analyzing the resonance shift. The relationship between the electrical impedance and the S_{11} parameter is expressed by

$$Z = Z_{ref} \cdot \frac{1+S_{11}}{1-S_{11}}. \tag{5.2}$$

where Z_{ref} is the system impedance and equals to 50 Ω.

5.5 Device Characterization

The laser-doppler vibrometer test was first carried out to test the vibration and the in-air resonance frequency of the CMUT before the functionalization. The CMUT was biased at 70 V and excited by a 10 Vpp AC continuous sinusoidal signal. Using a frequency sweep, the resonance frequency of the CMUT was measured to be 12.40 MHz with a $\pm$ 0.2 MHz variation across 10 randomly picked cells. Fig. 5.4 displays a 2-D scan image of the CMUT membrane displacement. Variations in the membrane displacement were observed due to the distinguished resonances of the cells.
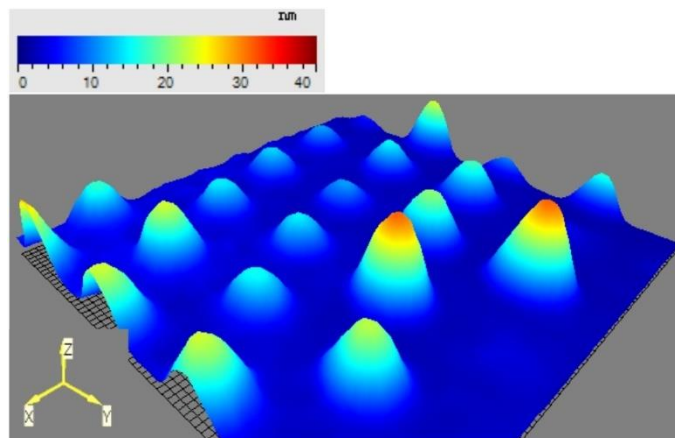
Fig. 5.4: Vibrometer displacement measurement of the CMUT at a 70 V DC voltage and a 10 Vpp

AC signal at 12.40 MHz.
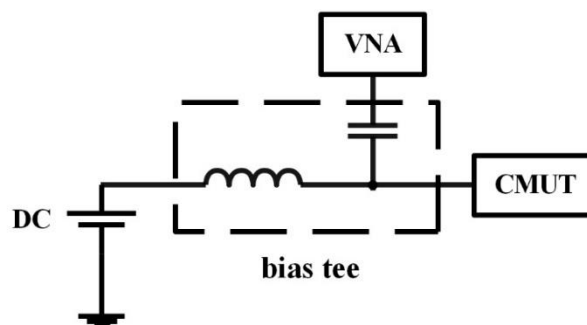
Fig. 5.5: Schematic of the setup for electrical impedance measurement.

The electrical input impedance of the CMUT was characterized by the VNA. Fig. 5.5 shows the schematic of the electrical layout for the test. The S_{11} parameters of the CMUT were measured at various DC voltages, then converted into electrical input impedances. Fig. 5.6 (a) and Fig. 5.6 (b) show the impedance magnitudes and the parallel resonance frequencies of the CMUT at different bias voltages, respectively. Due to the spring softening effect [23], the resonance frequency decreased as the DC bias voltage increased. When biased at 70 V, the measured resonance frequency of the CMUT was 12.315 MHz, which was close (0.6% variation) to the result from the vibrometer test.
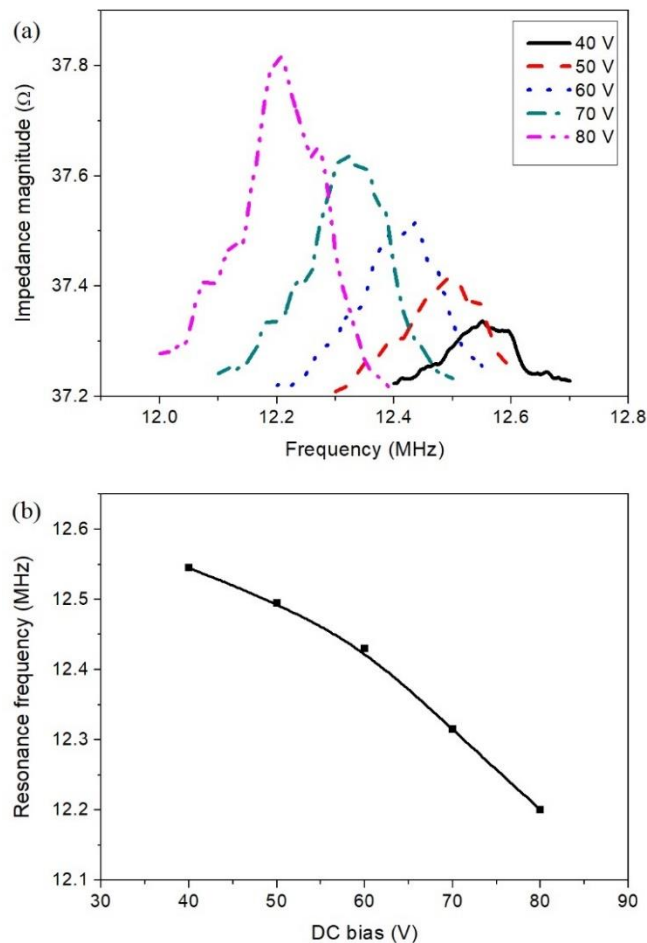
Fig. 5.6: (a) Measured impedance magnitude of the CMUT; (b) resonance frequencies at various

bias voltages.

61

A field emission scanning electron microscope (SEM, JSM 7200-F, JEOL) was used to characterize the surface morphology of the GO thin film, which is shown in Fig. 5.7. It can be seen that the uniformity of the coating was imperfect. Many clusters of GO nanoflakes were randomly distributed. This was caused partially by the non-uniform nature of the drop-casting technique and partially by the high concentration of the GO dispersion. The non-uniform film may result in improved sensitivity of the sensor due to the increased space for water molecule capture, but also degraded reversibility because the clusters can trap water molecules during desorption process. Other coating techniques such as spin coating and inkjet printing may be investigated for a more uniform coating in the future. This will be discussed in the last chapter of the thesis. After GO deposition, the impedance test showed a slight increase in the resonance frequency of the CMUT humidity sensor. Specifically, the resonance frequency increased from 12.20 MHz to 12.865 MHz when biased at 80 V.
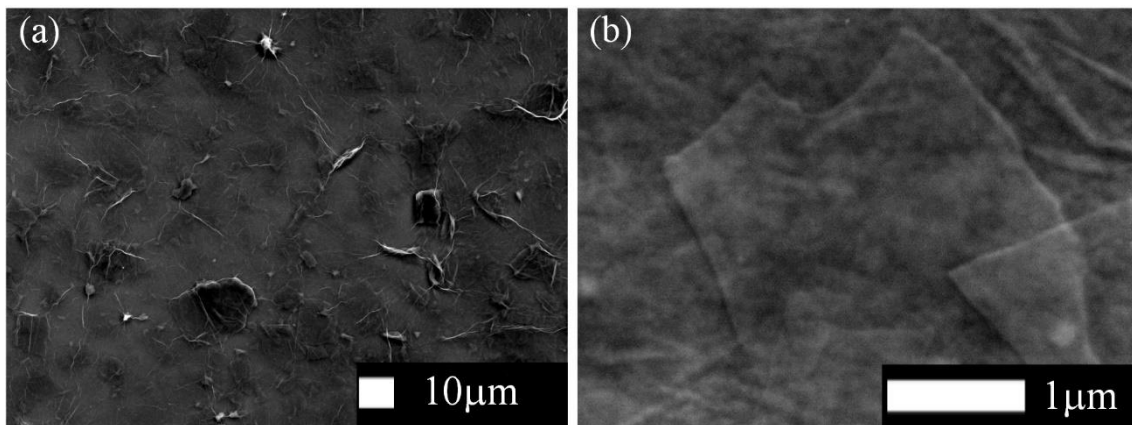
Fig. 5.7: SEM images of the GO morphology (a) 10 µm; (b) 1 µm.

5.6 Humidity Sensing Results
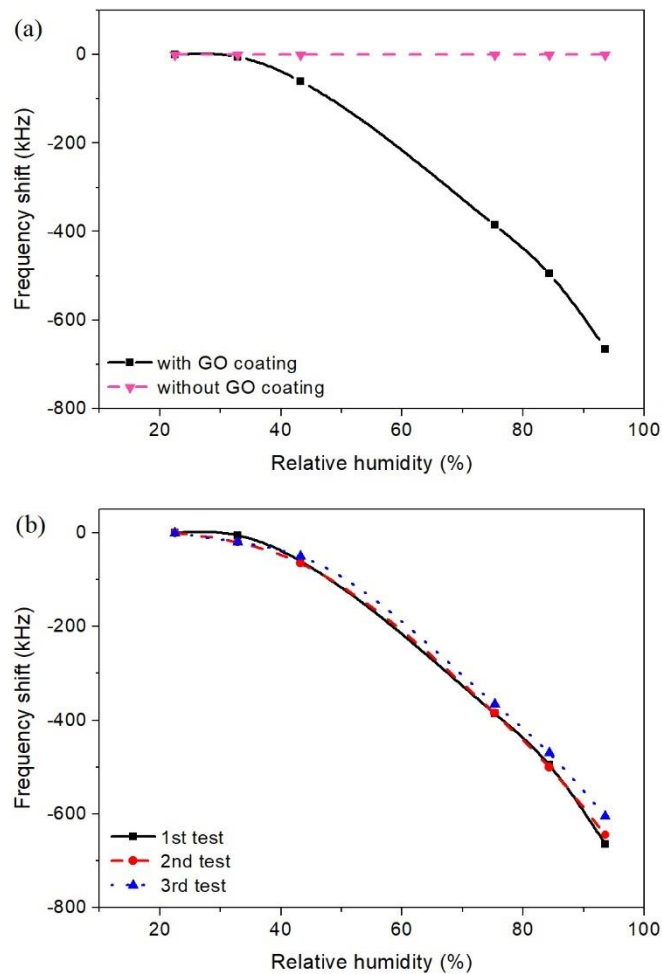
Fig. 5.8: (a) Resonance frequency response of CMUT humidity sensor at various RH levels;

(b) resonance frequency response in three different measurements.

The humidity sensing performance of the CMUT humidity sensor was characterized using the setup shown in Fig. 5.3. The resonance frequency shift Δf of the CMUT was analyzed at various RH levels before and after GO coating. Fig. 5.8 (a) displays the resonance frequency response when increasing the RH level from 22.5% to 93.6%. The frequency shift was negligible without GO coating due to the ultra-smooth silicon

membrane of the CMUT, which was not a good moisture adsorbent. After coating of the GO sensing layer, the humidity sensitivity was improved drastically. It is also observed that the resonance frequency shift was small at low RH levels (<43.2%), and large at high RH levels (>43.2%). An explanation was that the added mass of the GO film came from the adsorption of water molecules, which mainly concentrated on the surface of the film at low humidity levels, and penetrated into the interlayer of the film at high humidity levels, inducing a higher mass increase and thus a higher frequency shift [96]. Specifically, the sensitivity was calculated to be 2.9 kHz/%RH between the RH level of 22.5% and 43.2%, and 11.5 kHz/%RH between 43.2% and 93.6%. Table 5.1 presents a comparison between the CMUT in this work and other gravimetric humidity sensors reported in literature. The CMUT-based humidity sensor is found to exhibit a superior RH sensitivity over most of the competitors. In order to test the repeatability of the sensor, three measurements were conducted under the same condition in three different days. Fig. 5.8 (b) displays the resonance frequency responses of the three tests. It was found that the variation became larger with the increased RH level. The repeatability error reached the maximum of ±4.51% at the RH of 93.6%.

Table 5.1 Comparison between the CMUT sensor in this work and other reported gravimetric

humidity sensors

Reference	Sensor type	Resonance frequency (MHz)	Sensing material	Range of RH (%)	Sensitivity (kHz/%RH)
This work	CMUT	12	GO	22.5 - 43.2	2.9
				43.2 - 93.6	11.5
[13]	CMUT	50	mesoporous silica	0 - 20	2.6
[17]	SAW	392	GO	10 - 80	3.17 - 16.19
				80 - 90	42.08
[97]	SAW	200	sol-gel SiO_2	30 - 93	8.3
[98]	FBAR	1400	zinc oxide	20 - 50	2.2
				50 - 95	8.5
[18]	FBAR	1250	GO	3 - 70	5
[42]	QCM	10	GO	6.4 - 93.5	up to 0.022
[99]	QCM	10	GO/poly(ethyleneimine)	11.3 – 97.3	0.027
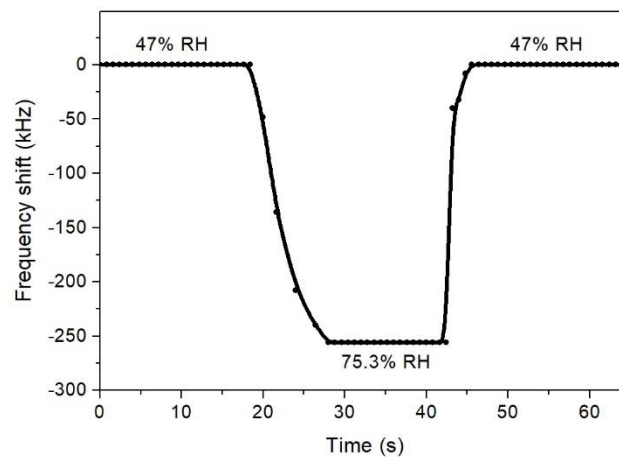
Fig. 5.9: Dynamic frequency shift of the CMUT humidity sensor with the RH level switching

between 47% and 75.3%.

The time-dependent frequency response of the CMUT humidity sensor was tested

by switching the sensor between the laboratory ambiance (47% RH) and a 75.3% RH

environment provided by NaCl solution. The resonance frequency of the CMUT in the

laboratory atmosphere was first recorded as the baseline. Then the frequency shift was monitored by the VNA and recorded by a LabVIEW program. The dynamic frequency response of the sensor, as shown in Fig. 5.9, indicated that the CMUT humidity sensor had fast response-recovery performance. The response time and recovery time (defined as the time for reaching 90% of the steady state) were measured to be 10 s and 4 s, respectively.
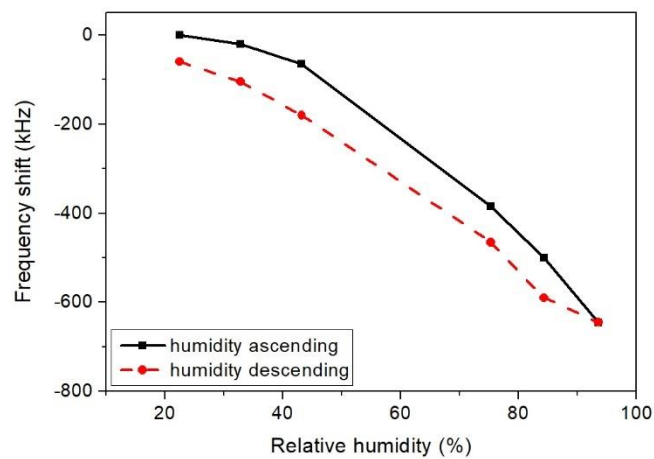
Fig. 5.10: Humidity hysteresis curve of the CMUT humidity sensor.

Hysteresis due to water molecule adsorption is a common phenomenon for humidity sensors [100]. The humidity hysteresis characteristic of the CMUT humidity sensor was investigated by measuring its resonance frequency response with the RH increased from 22.5% to 93.6% and then decreased back to 22.5%. Fig. 5.10 shows the tested hysteresis curve. Compared to the frequency shift in the humidity-ascending response curve, a decline in the frequency shift was observed in the humidity-descending response curve. It is also observed that the hysteresis level was slightly higher at lower RH levels (<43.2%) and peaks at 43.2% RH. The possible reason for the hysteresis was that the water

molecules were trapped in the deep layer of the GO film and were difficult to desorb when decreasing the RH from high humidity levels [17].

5.7 Summary

This chapter presents a highly sensitive CMUT-based humidity sensor with GO sensing film. The CMUT transducer with a diameter of 2 mm and an operating frequency of 12 MHz was fabricated by the direct wafer bonding technique. To validate the design, both the laser vibrometer and the VNA were adopted to characterize the resonant properties of the fabricated device. A GO thin film was then coated as the water vapor adsorbing layer on the resonating membranes of the CMUT. The humidity sensing performance of the CMUT humidity sensor was evaluated through the electrical impedance analysis over an RH range of 22.5% to 93.6%. Frequency shifts caused by the added mass of the absorbed water molecules was observed in the measurements. Particularly, the sensor exhibited a humidity sensitivity of 2.9 kHz/%RH at low RH levels and 11.5 kHz/%RH at high humidity levels. It also showed decent repeatability with a maximum repeatability error of ±4.51% and a short response/recovery time of 10 s/4 s. Benefit from the MEMS technology and the water-sensitive GO, CMUTs have shown to be a strong candidate for miniaturized and highly sensitive humidity sensing platform.

Chapter 6 CMUT Humidity Sensors Fabricated with Nitride-to-Oxide Wafer Bonding Technology

6.1 Revisiting Motivation

In the last chapter, the CMUT-based humidity sensor functionalized with GO showed an excellent sensitivity of up to 11.5 kHz/%RH between an RH level of 22.5% to 93.6%. The moisture-sensitive GO significantly enhanced the humidity sensing performance of the CMUT due to its abundance of oxygen-containing groups. Although the CMUT-based humidity sensor was more sensitive than most of its competitors, there is still a need to further improve its sensitivity. This work aims to improve the RH sensitivity by introducing the nitride-to-oxide wafer bonding technology for fabrication of CMUT sensors. Previously, the CMUT was fabricated by the standard wafer fusion bonding technique, which bonded an SOI wafer with a thermally oxidized bottom wafer. The resonating membranes of CMUTs came from the silicon device layer of the SOI wafer. Employing SOI wafers can lead to several issues. First, obtaining commercial SOI wafers with a thin device layer at the sub-micron level can be difficult. This limits the flexibility of sensor design and performance optimization. Moreover, the poor thickness uniformity of the device layer can degrade sensor performance, despite the high cost of SOI wafers. A solution is to avoid the use of SOI wafers by adopting thin Si_3N_4 resonating membranes for CMUTs. The Si_3N_4 layer can be grown by LPCVD, so its thickness can

be customized. As a result, thinner and lighter membranes can be easily achieved for a higher mass sensitivity. In general, CMUTs with Si_3N_4 membranes are fabricated by the sacrificial release process [9], which produces stiction during the releasing process. As such, the CMUT sensitivity often has to be compromised in order to reduce stiction by making a larger gap between the membrane and the substrate.

In 2009, our group reported a nitride-to-nitride wafer bonded CMUT with promising acoustic and electrical results [101]. In this process, a chemical mechanical polishing (CMP) step was required to smoothen the surface of both the bottom and top wafers before wafer bonding. More recently, we developed a nitride-to-oxide wafer bonding process [102] and fabricated a CMUT for the collapse-mode operation [103], where the membrane was in contact with the substrate. The new wafer bonding technique requires a CMP step solely for the top wafer. When compared to conventional SOI-based wafer bonding processes, it reduced the number of photomasks from four to three for CMUT fabrication. As a result, the fabrication cost was reduced without compromising the performance.

In this chapter, highly sensitive CMUT humidity sensors that were fabricated by the nitride-to-oxide wafer bonding process is reported. The CMUTs are functionalized by GO with three different concentrations. Based on the first-generation CMUT-based humidity sensor presented in Chapter 5, this chapter aims to improve the RH sensitivity and device uniformity, and reduce the fabrication cost and operating voltage. The

humidity sensing performance of the CMUT sensors is investigated by measuring their

RH sensitivity, repeatability, dynamic response, and hysteresis characteristics.

6.2 Sensor Design

Eq. (5.1) indicates that a smaller radius results in a higher mass sensitivity. Apart

from the mass sensitivity, the operating voltage is another design criterion for CMUTs.

It is estimated from the pull-in voltage V_{pi}. By substituting Eq. (3.2), Eq. (3.7) and Eq.

(3.21) into Eq. (3.20), we can get the relationship between V_{pi} and the CMUT dimension

and material properties as

$$V_{pi} \propto \sqrt{\frac{E t_m^3 d_{eff}^3}{\varepsilon_0 a^4 \left(1-\upsilon^2\right)}} \ . \tag{6.1}$$

It can be seen that a lower pull-in voltage requires a larger radius, which contradicts to

the high mass sensitivity. An optimum solution should ensure mass sensitivity while

maintaining the operating voltage in an acceptable range. One way to achieve that is to

control the pull-in voltage by selecting a suitable membrane material, which is typically

limited to silicon or silicon nitride due to the fabrication process of CMUTs. Nonetheless,

the influence of material properties is small compared to that caused by the changes in

the CMUT dimension. A more effective way to design a small cavity depth. However, it

poses huge fabrication challenges when the radius gets too small and the cavity needs to

be extremely shallow, for instance, under 50 nm. At such a small scale, the fabrication

error tolerance will be very small because the cavity-to-cavity variation can have a

significant impact on the device performance. Another alternative is to employ thin

membranes for CMUTs. Although it is possible to achieve thin silicon membranes at the sub-micron level, it is often difficult due to the limited availability of commercial SOI wafers. The uniformity of the thin device layer of SOI wafers may also be a problem. To this regard, Si_3N_4 membrane is a good choice because it is easy to obtain thin LPCVD Si_3N_4 layers at the sub-micron level. Moreover, Si_3N_4 layers grown by the LPCVD process naturally have an excellent thickness uniformity, which is favorable for a high quality factor. This further explains why the nitride-to-oxide bonding process is more suitable for CMUT sensing applications than the conventional SOI-involved process.

Here, 3 mm-diameter circular CMUTs with Si_3N_4 membranes were designed. The critical design parameters are presented in Table 6.1. The CMUTs were designed with an in-air resonance frequency of 10 MHz and a membrane thickness of 520 nm. The membrane radius was then uniquely optimized via FEA simulation. The DC operating voltage was designed to be under 50 V and the cavity depth was determined accordingly.

Table 6.1 Design parameters of the CMUTs.

Parameter	Value
Resonance frequency	10 MHz
Membrane thickness	520 nm
Membrane diameter	30 μm
Cavity depth	180 nm
Electrode thickness	100 nm
Operating voltage	< 50 V

Number of cells	5380

6.3 Sensor Fabrication
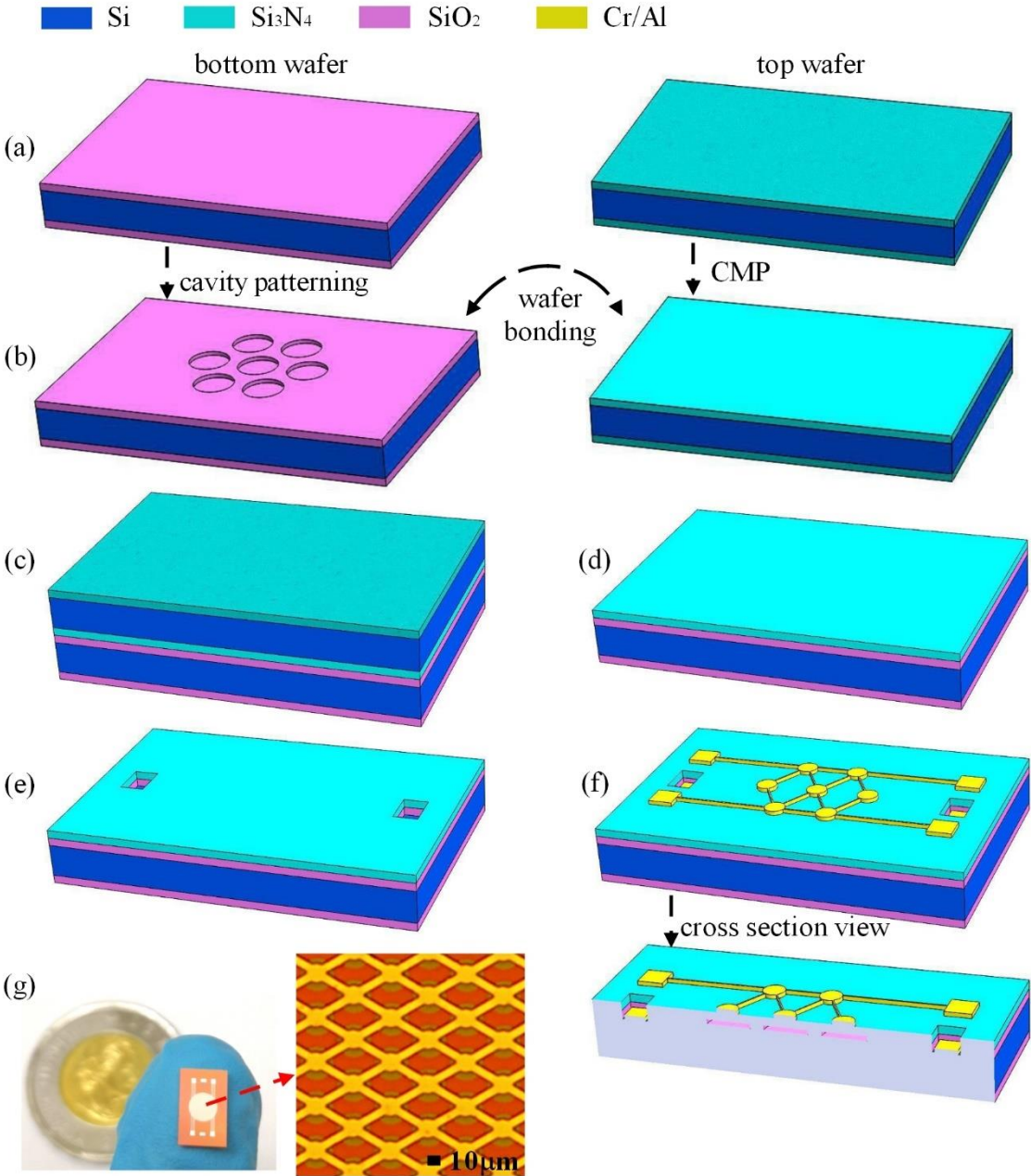
Fig. 6.1: Process flow of the CMUT.

The CMUTs were fabricated using the nitride-to-oxide wafer bonding process, which required only three photomasks. The process, as shown in Fig. 6.1, started with

two 100-mm 0.001-0.005 ohm-cm <100> silicon wafers, which later served as the bottom wafer and top wafer, respectively. In step (a), a 600 nm Si_3N_4 layer was deposited on the top wafer using the LPCVD process and a 500 nm SiO_2 layer was thermally grown on the bottom wafer. In step (b), the bottom wafer was etched with cavities by RIE. In order to achieve an ultra-smooth surface for a successful wafer bonding [101], [102], [104], the top wafer was treated with a CMP process to reduce the surface roughness to sub-nanometer scale. In step (c), the wafers were cleaned in RCA 1 and RCA 2 baths [88] for 5 minutes each, followed by another 5-minute RCA 1 cleaning and a 10-minute oxygen plasma treatment. Then the wafers were fusion bonded under a 2500 N compressive force for 20 minutes. Subsequently, the wafer pair was annealed at 1100 °C for an hour to strengthen the bonding. In step (d), the backside Si_3N_4 layer and the silicon handling layer of the top wafer were removed by RIE and TMAH etching, respectively. Next, a lithography and RIE step was performed to expose the bottom electrode (step (e)). In step (f), the electrode contact pads, formed by 20 nm of chromium and 80 nm of aluminum, were deposited using an e-beam evaporation and a lift-off process.

In this fabrication process, a CMP process before wafer bonding is of crucial importance. For a successful bonding, it is critical to ensure that the root-mean-square (RMS) surface roughness of the wafers is within 10 Å$_{RMS}$ [105]–[107]. The thermally oxidized prime silicon wafer and the LPCVD Si_3N_4 layer naturally meet this requirement. However, the wafer bonding kept failing without the CMP process. Based on our previous experience in fabrication, the thermal oxide grown in our facility is safe for bonding.

Therefore, a roughness characterization on the LPCVD Si_3N_4 layer was performed using atomic force microscopy (AMF). Fig. 6.2 and Fig. 6.3 display the AFM scan of a 520 nm – thick LPCVD Si_3N_4 layer without and with CMP, respectively. In a scanning area of 100 nm * 100 nm, the surface roughness of the nitride layer without CMP was only 4.7 ÅRMS, even smaller than that with CMP. However, there existed lots of randomly distributed large bumps on the surface without CMP. The bumps have varied heights and noticeable areas of vacancies between them. The possible reason for the failed wafer bonding was that the effective bonding area had been significantly reduced by these bumps. After CMP, on the contrary, although the RMS surface roughness slightly increased and countless nanopillars were introduced, these nanopillars were extremely small in diameter and very densely positioned. The effective bonding area was considerably increased. As a result, the bonding was very successful and a fabrication yield of over 90% was achieved.

(a) Roughness = 4.7 Å$_{RMS}$

(b)
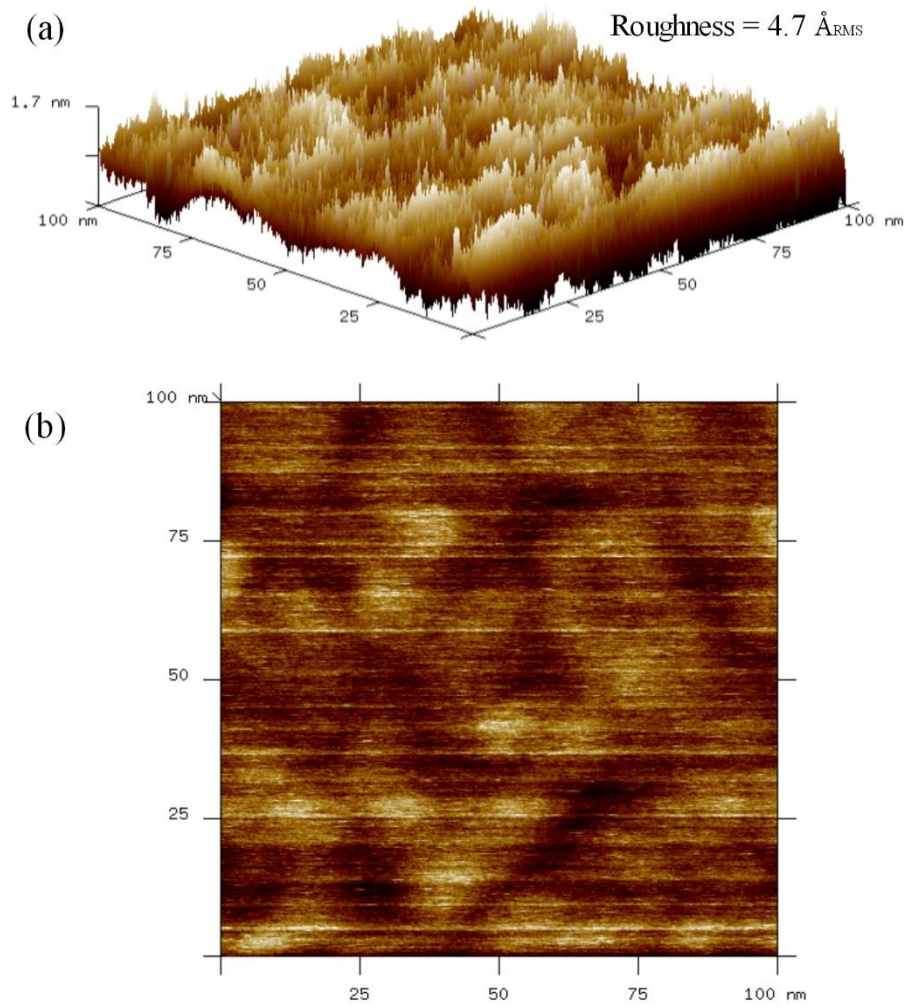
Fig. 6.2: The AFM scan showing the surface roughness of a 520 nm LPCVD Si$_3$N$_4$ layer without

CMP: (a) 3D view; (b) top view.

(a)

Roughness = 7.5 $\mathring{A}_{RMS}$

(b)
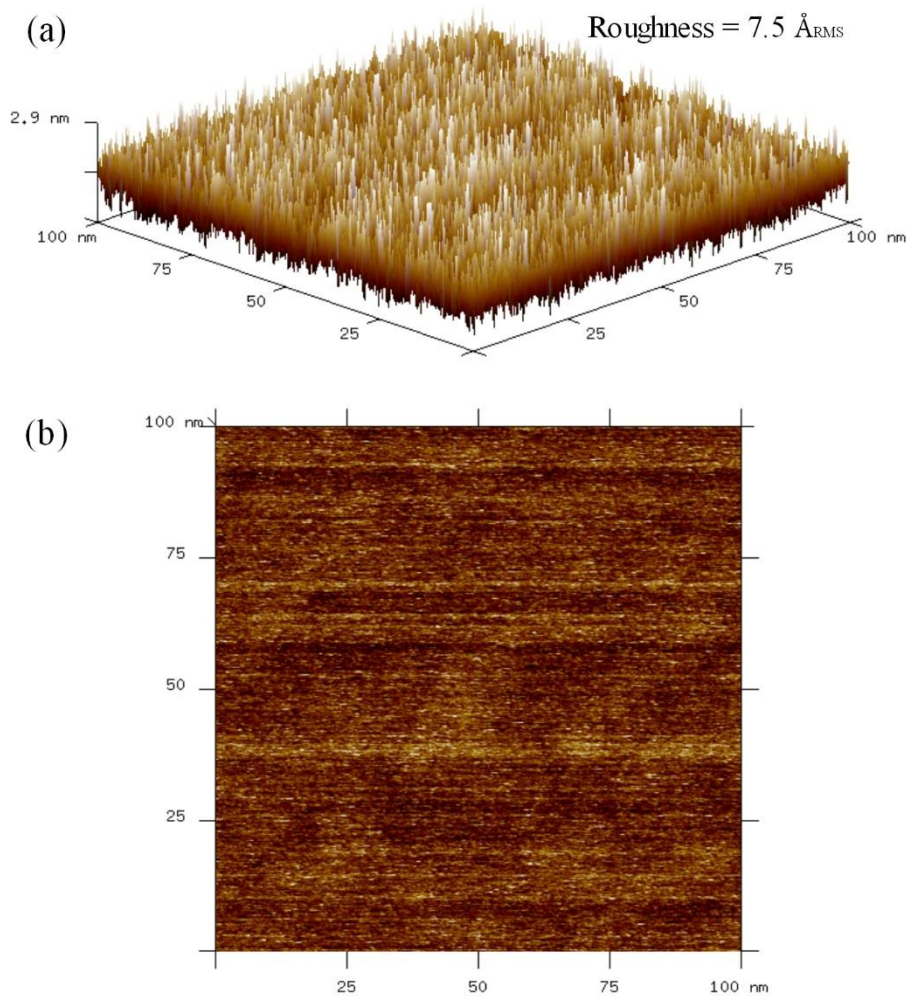
Fig. 6.3: The AFM scan showing the surface roughness of a 520 nm LPCVD Si_3N_4 layer with CMP

(a) 3D view; (b) top view.

After fabrication, the CMUTs were functionalized by drop-casting 6 μL of GO dispersion on the membranes using a microliter syringe. This volume of GO dispersion was determined such that it was able to cover the whole area of the CMUT membranes. The GO thin films were formed after water evaporation in room temperature. To investigate the influence of the GO concentration on the sensor performance, GO dispersions with a concentration of 0.5 mg/ml, 0.25 mg/ml and 0.1 mg/ml were prepared for three CMUTs. The corresponding CMUT humidity sensors were labeled as CMUT-

1, CMUT-2, and CMUT-3, respectively. After coating of the GO thin films, the sensors were kept in room temperature for three weeks until its structure and chemistry properties became stable.

6.4 Device Characterization

Before functionalization of the CMUTs, a laser vibrometer measurement was performed to test their resonance frequencies and cell-to-cell uniformity. Using a frequency sweep with a function generator, the in-air resonance frequency of the biased CMUT-1 was determined at where the membrane displacement reaches the maximum. Fig. 6.4 (a) shows the 2D scan image of the membrane displacement when CMUT-1 was biased at 35 V and excited by a 1 Vpp 10.20 MHz continuous sinusoidal signal. In order to test the cell-to-cell uniformity, the resonance frequencies of 20 cells in a row were measured. Fig. 6.4 (b) displays the resonance frequencies at a bias voltage of 20 V, 30V, and 40 V. A maximum variation of 0.11 MHz (~1%) was observed between the cells, showing an outstanding device uniformity.
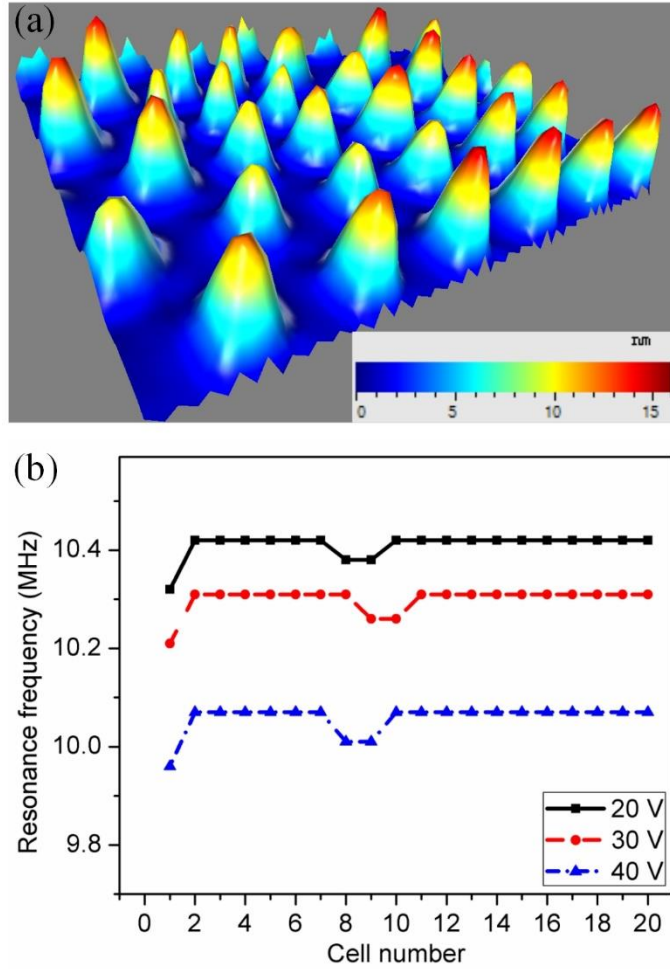
Fig. 6.4: Laser vibrometer test of CMUT-1: (a) 2D scan of the membrane displacement at a 35 V

bias voltage and a 1 Vpp 10.20 MHz continuous sinusoidal signal; (b) resonance frequencies of 20

cells at different bias voltages.

The electrical input impedance of CMUT-1 was first characterized. The pull-in

voltage V_{pi} of the CMUT-1 was measured to determine the operating bias. By gradually

increasing the DC bias, the pull-in voltage was measured to be 60 V, at which an abrupt

resonance shift was identified. The impedances before and after the functionalization

were measured at various bias voltages and are shown in Fig. 6.5 (a) and Fig. 6.5 (b),

respectively. It is observed that the phases of impedances were always negative after

functionalization. This mainly resulted from the capacitive characteristics of the CMUT

sensor. It might also mean that the device had a weak resonance. Nonetheless, the CMUT

can still serve as an effective humidity sensor because the resonance frequency or

frequency shift can be clearly determined from the amplitude of impedance. Fig. 6.5 (b)

also indicates the decrease in quality factor after functionalization, which was due to the

extra energy dissipation induced by the GO film. This may degrade the resolution for

humidity sensing. Similar results were found with CMUT-2 and CMUT-3, the

impedances of which are shown in Fig. 6.6 and Fig. 6.7, respectively. It is also observed

that the performance of CMUT sensors coated with lower-concentrated GO was less

affected by the functionalization.
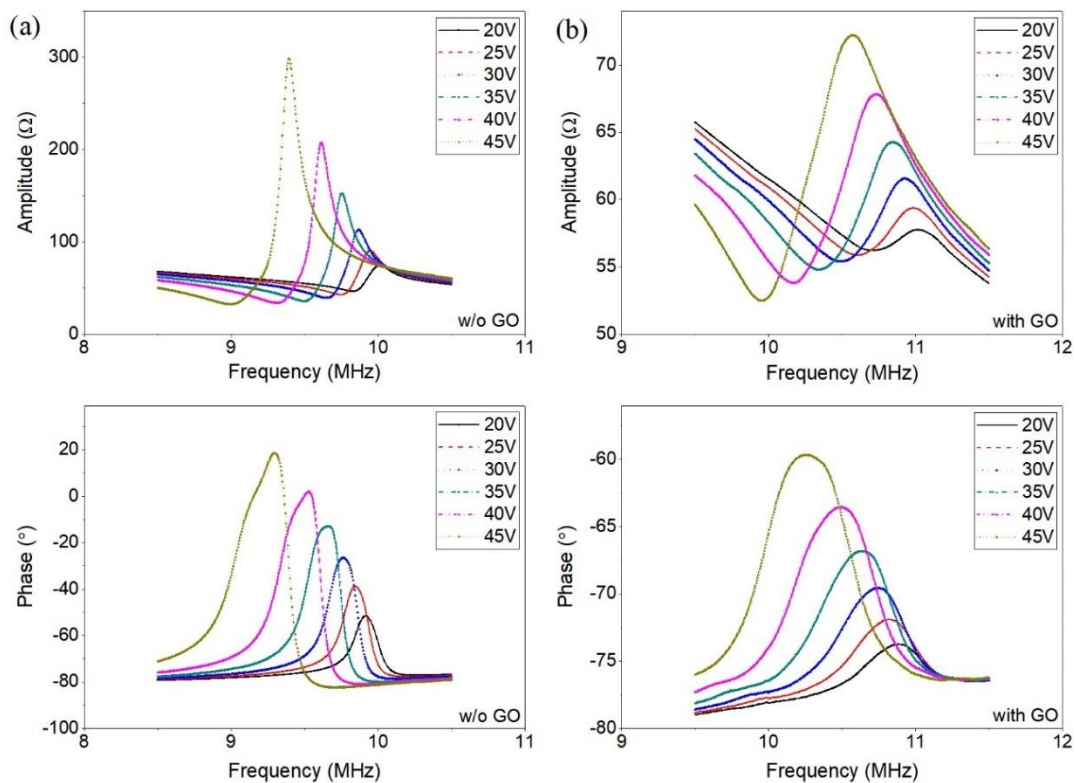
Fig. 6.5: Electrical impedance measurement of CMUT-1: (a) without GO; (b) with GO.
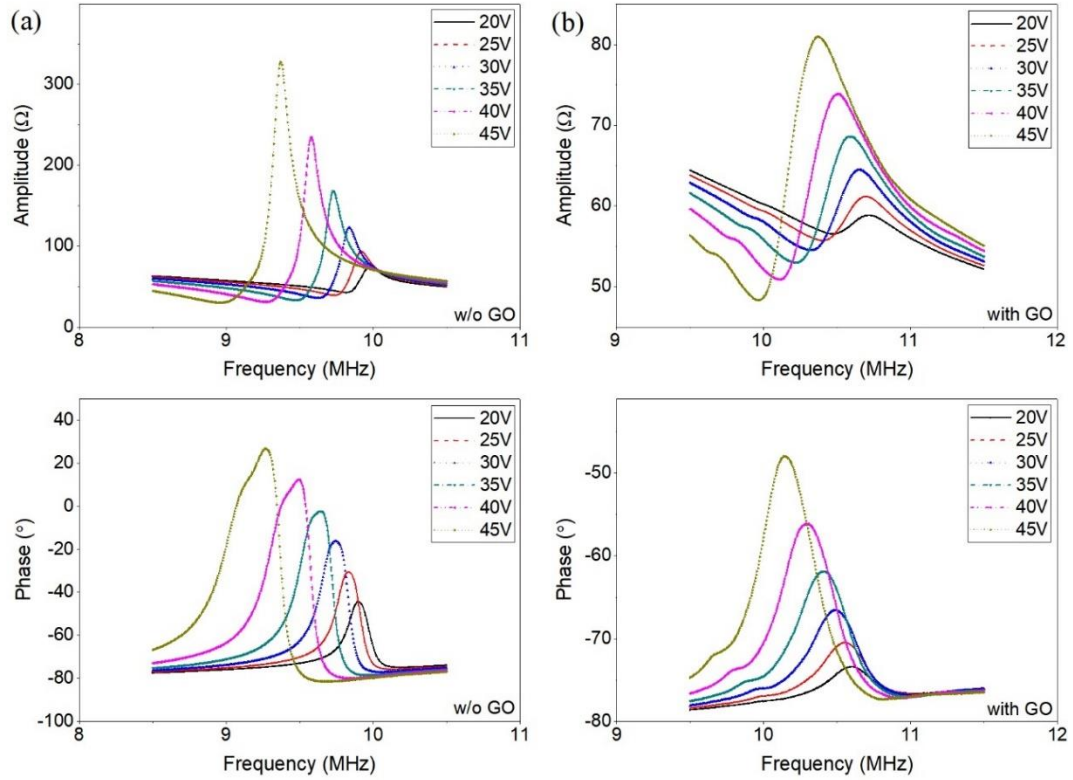
Fig. 6.6： Electrical impedance measurement of CMUT-2: (a) without GO; (b) with GO.
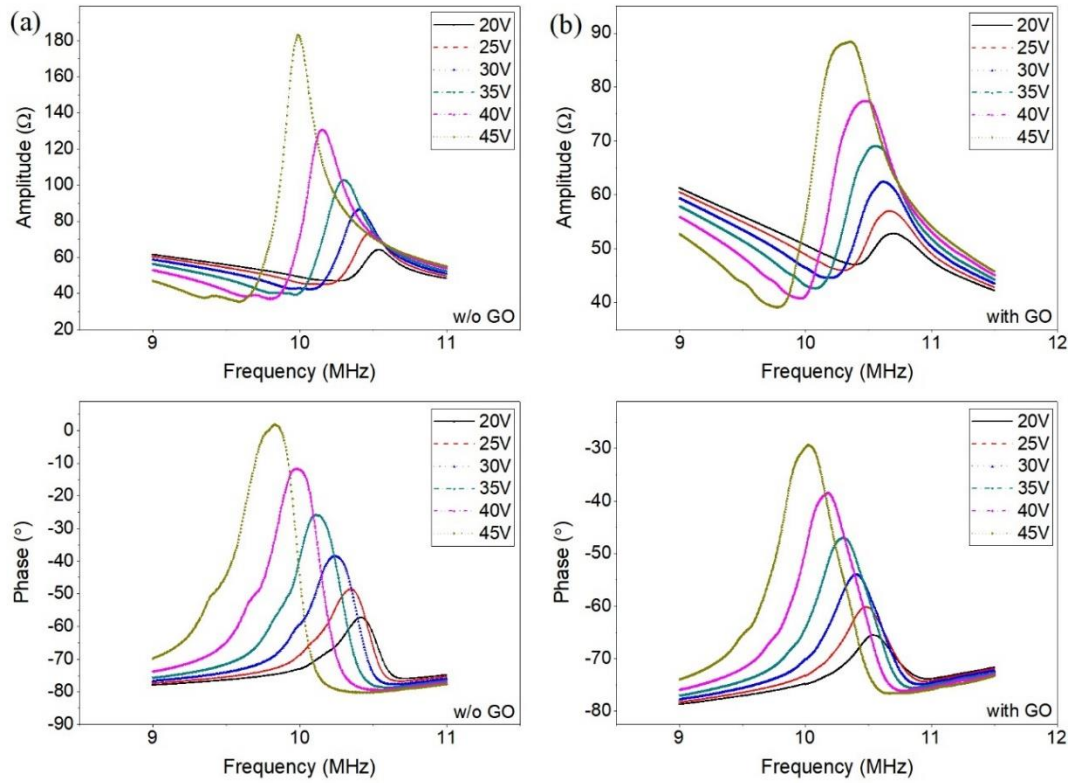
Fig. 6.7: Electrical impedance measurement of CMUT-3: (a) without GO; (b) with GO.

Fig. 6.8 presents the parallel resonance frequency of the CMUTs as a function of the bias voltage. Taking CMUT-1 as an example, the resonance frequency showed a good agreement with that from the laser vibrometer test. As the bias voltage increased, the resonance frequency decreased due to the spring softening effect. It is also observed that the resonance shifted to higher frequencies after coating the GO thin film, which was attributed to the increased effective thickness of the resonating membranes. Among the three sensors, CMUT-1 got the largest frequency shift as expected due to the highest concentration of GO.
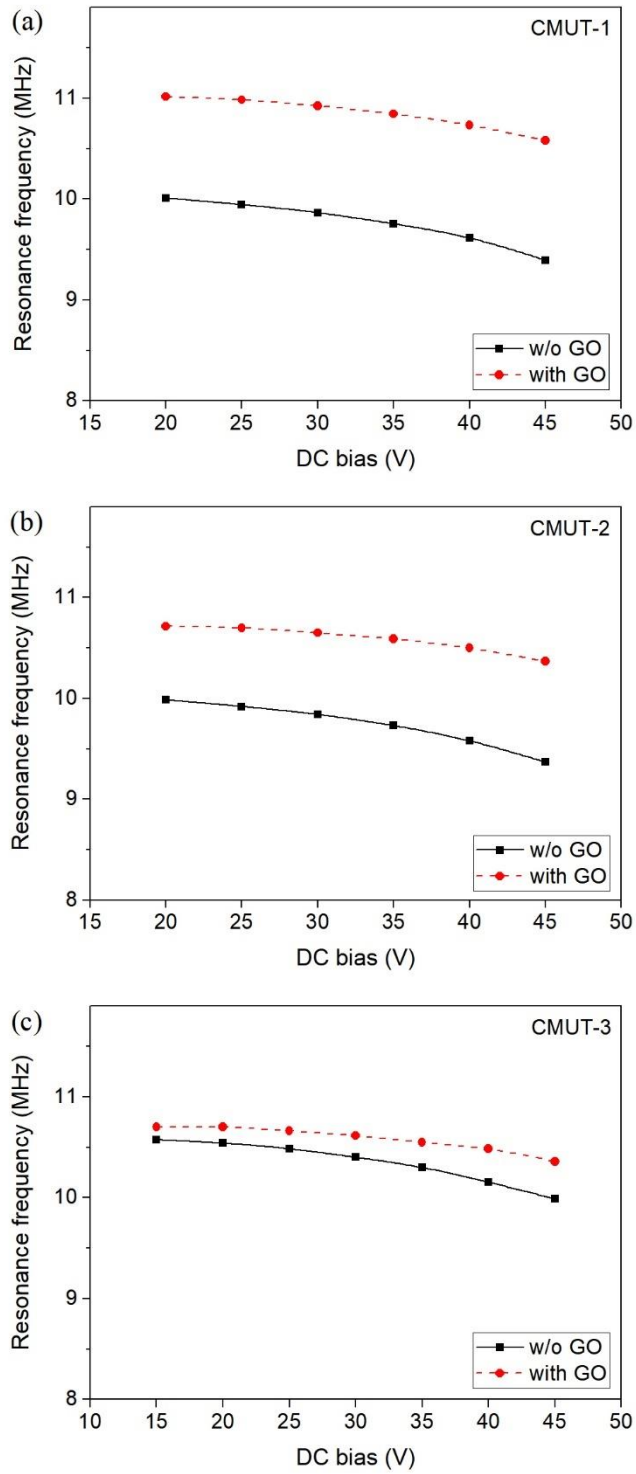
Fig. 6.8: Resonance frequency as a function of the bias voltage: (a) CMUT-1; (b) CMUT-2; (c) CMUT-3.

The morphologies of GO films were examined by SEM. Fig. 6.9 (a-e) presents the surface morphologies of GO films coated on the CMUT membranes (Fig. 6.9 (a)) and a silicon substrate (Fig. 6.9 (b-e)). It is noticed that the GO film with a higher concentration was more tortuous. Fig. 6.9 (f) and Fig. 6.9 (g) show the cross-section views of a CMUT cell without and with GO coating, respectively. Because taking cross-section images required permanent damaging of the CMUT and we had limited number of dummy samples, only a CMUT coated with 0.5 mg/mL GO was used for the imaging. The measured thickness of the GO film was around 175 nm.
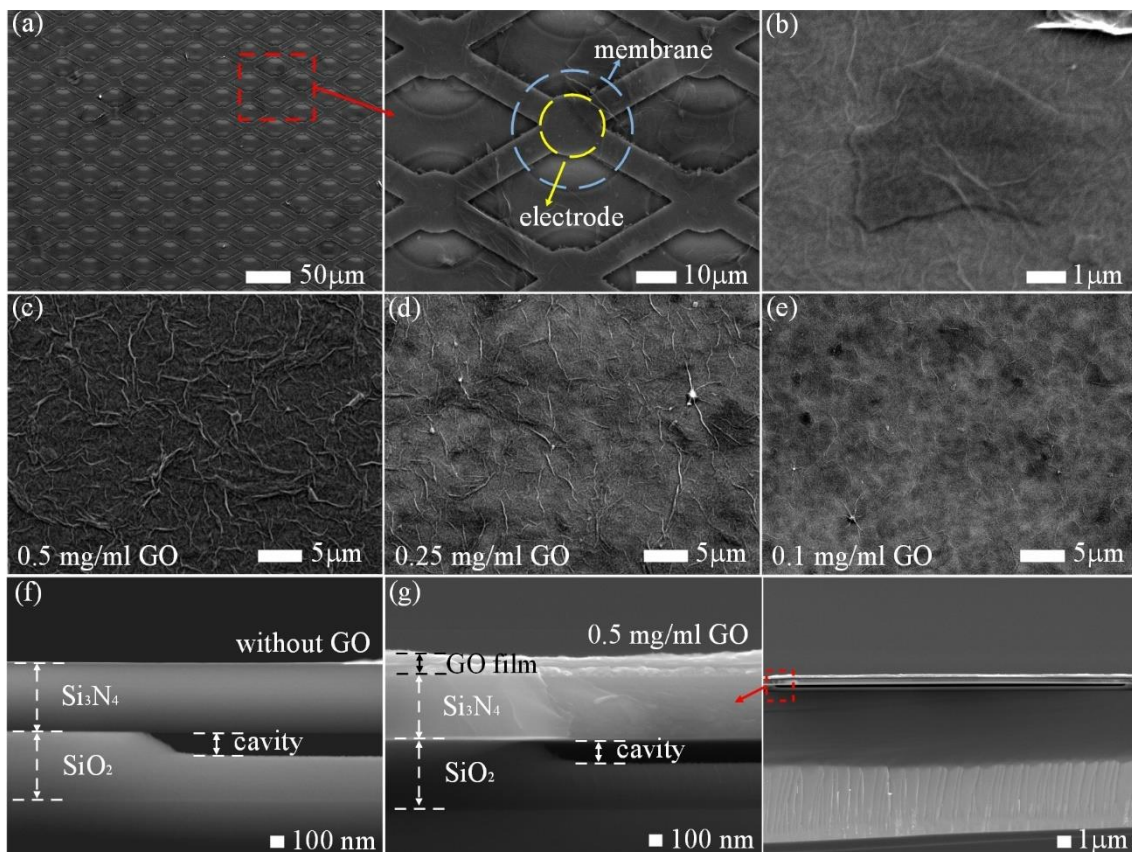
Fig. 6.9: SEM images of: morphologies of (a) GO on the CMUT membranes, (b) GO nanosheet, (c) 0.5 mg/ml GO, (d) 0.25 mg/ml GO, (e) 0.1 mg/ml GO; cross-section views of a CMUT cell (f) without GO coating, (g) with GO coating.

6.5 Apparatus
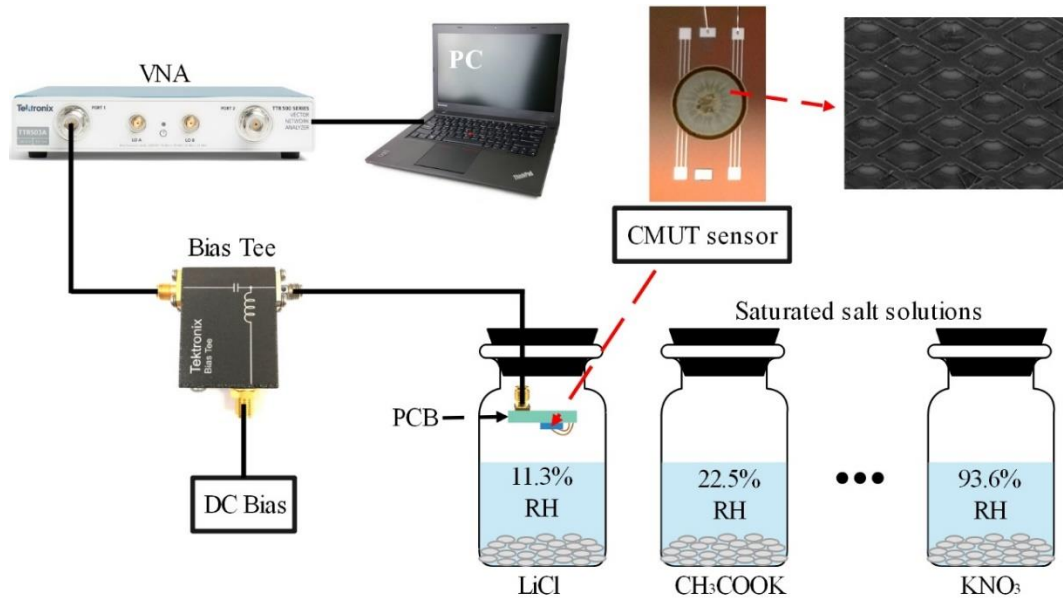
Fig. 6.10: Schematic diagram of the humidity sensing experimental setup.

Fig. 6.10 shows the schematic diagram of the experimental setup for humidity sensing. The RH levels of 11.3%, 22.5%, 32.8%, 43.2%, 52.9%, 75.3%, 84.3%, and 93.6% were generated by saturated salt solutions of lithium chloride (LiCl), potassium acetate (CH$_3$COOK), magnesium chloride (MgCl$_2$), potassium carbonate (K$_2$CO$_3$), magnesium nitrate (Mg(NO$_3$)$_2$), sodium chloride (NaCl), potassium chloride(KCl), and potassium nitrate (KNO$_3$) , respectively [94]. For the SOI-based CMUT humidity sensor presented in Chapter 5, LiCl (RH 11.3%) and Mg(NO$_3$)$_2$ (RH 52.9%) were not used for the humidity sensing tests. It was because the two salts were out of stock at the time of purchasing and some unexpected problem with the order resulted in a very long leading time. Hence, I decided to perform experiments without testing the two RH levels. Later on, the SOI-based CMUT used in Chapter 5 broke down during a pull-in test. So the two RH levels were not tested. Here for the Si$_3$N$_4$-based CMUTs, all ordered salts have arrived and an RH level from 11.3% to 93.6% were measured. Note that all measurements were

performed at room temperature. The CMUT sensors were biased at $0.6 \cdot V_{pi}$ during the humidity sensing tests. The frequency shifts of the sensors were analyzed from the S_{11} parameters measured by the VNA.

6.6 Humidity Sensing Results and Discussion

Table 6.2 Humidity sensing performance of the CMUT sensors.

Label of sensors		CMUT-1	CMUT-2	CMUT-3
GO concentration (mg/ml)		0.5	0.25	0.1
Humidity sensitivity	RH 11%-43%	5.6	4.7	3.5
(kHz/%RH)	RH 43%-93%	15.3	8.7	
Maximum repeatability error (%)		± 2.3	± 1.6	± 2.2
Response/recovery time (s)		11/3	15/3	10/3

The humidity sensing performance of the three CMUT sensors was characterized by measuring the frequency shifts as a function of the RH level. Fig. 6.11 (a) displays the frequency responses as the RH level increased from 11.3% to 93.6%. The sensing performance of the sensors is summarized in Table 6.2. It is observed that the sensor with a lower GO concentration produced a lower RH sensitivity but yet better linearity. For both CMUT-1 and CMUT-2, the frequency shifts were smaller at RH levels below 43.2% and increased at higher RH levels. Based on this transition, their humidity sensitivities were calculated in the two ranges. CMUT-1 and CMUT-2 achieved a sensitivity of up to 15.3 kHz/%RH and 8.7 kHz/%RH, respectively. In contrast, CMUT-3 had an

approximately linear frequency response, with a sensitivity of 3.5 kHz/%RH. The reason

for the discrepancy in sensitivity is quite straightforward. A lower concentration of GO

leads to less adsorption of water molecules and thus smaller frequency shifts. Regarding

the linearity, CMUT-1 and CMUT-2 had thicker GO films, within which the water

molecules could penetrate into the interlayer at high humidity levels and result in larger

frequency shifts [96], whereas the water adsorption mainly took place on the surface of

CMUT-3.
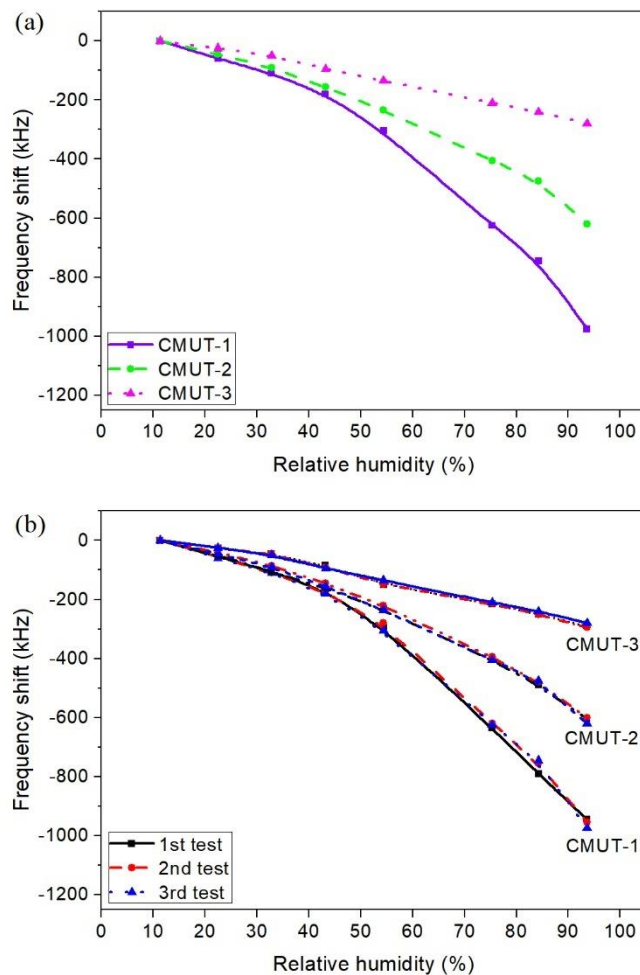
Fig. 6.11: Humidity sensing measurements of the three CMUT sensors: (a) frequency shifts as a

function of RH; (b) frequency responses in three measurements.
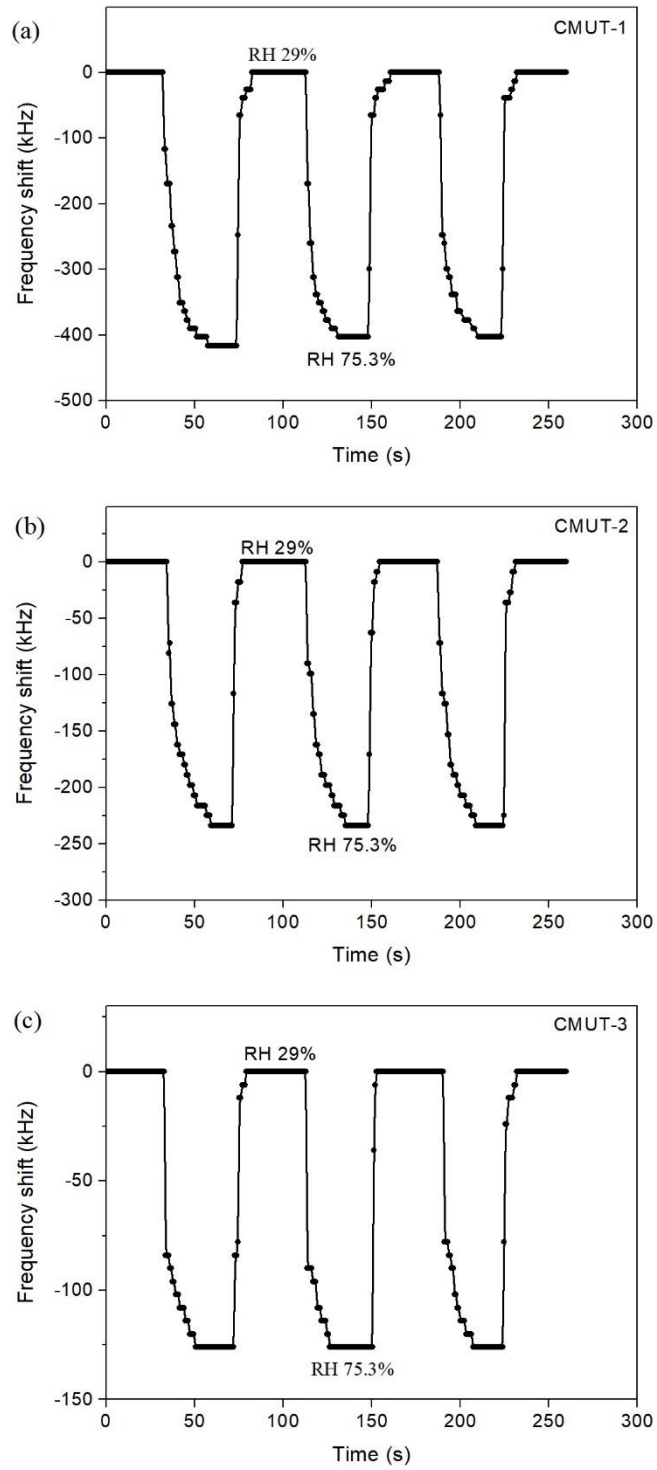
Fig. 6.12: Dynamic frequency shifts of the CMUT sensors with the RH level switching between

29% and 75.3%: (a) CMUT-1; (b) CMUT-2; (c) CMUT-3.

The repeatability of the sensors was examined by performing three humidity sensing measurements under the same experimental condition in different days. The testing results are shown in Fig. 6.11 (b). The repeatability error was calculated as the ratio of the maximum deviation in frequency shifts to the full-scale frequency shift. All the three CMUT sensors exhibited excellent repeatability, with a maximum repeatability error of $\pm 2.3\%$, $\pm 1.6\%$, and $\pm 2.2\%$, respectively.

To characterize the dynamic responses of the CMUT sensors, their resonance frequencies in the laboratory ambiance (29% RH) was used as the benchmark. The dynamic frequency shifts were recorded by the VNA and the Labview program while alternating the sensors between the ambiance and the 75.3% RH environment provided by the saturated NaCl solution. During the switching, the sensors were kept in the ambiance for about 32 s and in the 75.3% RH environment for a little longer time of 42 s to allow sufficient water adsorption. The switching time was controlled in 1 s after repetitive practices. Fig. 6.12 shows the time-dependent responses of the sensors. All the sensors exhibited fast response-recovery performance. The measured response/recovery time for CMUT-1, CMUT-2, and CMUT-3 was 11/3 s, 15/3 s, and 10/3 s, respectively. It is observed that the frequency shifts between 29% RH and 75.3% RH were smaller in the dynamic tests than that shown in Fig. 6.11, and the discrepancy was the most evident with CMUT-1, which employed the highest concentration of GO. The inconsistency was likely induced by two factors. The first one was the different environment in the laboratory ambiance and in the bottle with saturated salt solutions. Subtle alternations in

the environment such as pressure change might have affected the sensing results. The second cause might be the different ways of switching between RH levels. Instead of increasing and decreasing the RH level gradually, the sensors were moved directly between a low and a high RH environment in the dynamic tests, leading to inadequate desorption of water molecules and thus smaller frequency shifts.

The humidity hysteresis of the sensors was examined by gradually increasing the RH level from 11.3% to 93.6% for water adsorption and then decreasing back to 11.3% for water desorption. The frequency shifts were monitored by the VNA. Fig. 6.13 shows the hysteresis curves of the three sensors. The humidity-descending curves were observed to be slightly lagged behind the humidity-ascending curves for all the sensors, possibly caused by the trap of water molecules in the interlayer of GO films during the desorption process [17]. The level of hysteresis reaches the maximum at the RH level of 43.2%, 43.2%, and 32.8% for CMUT-1 to CMUT-3, respectively.
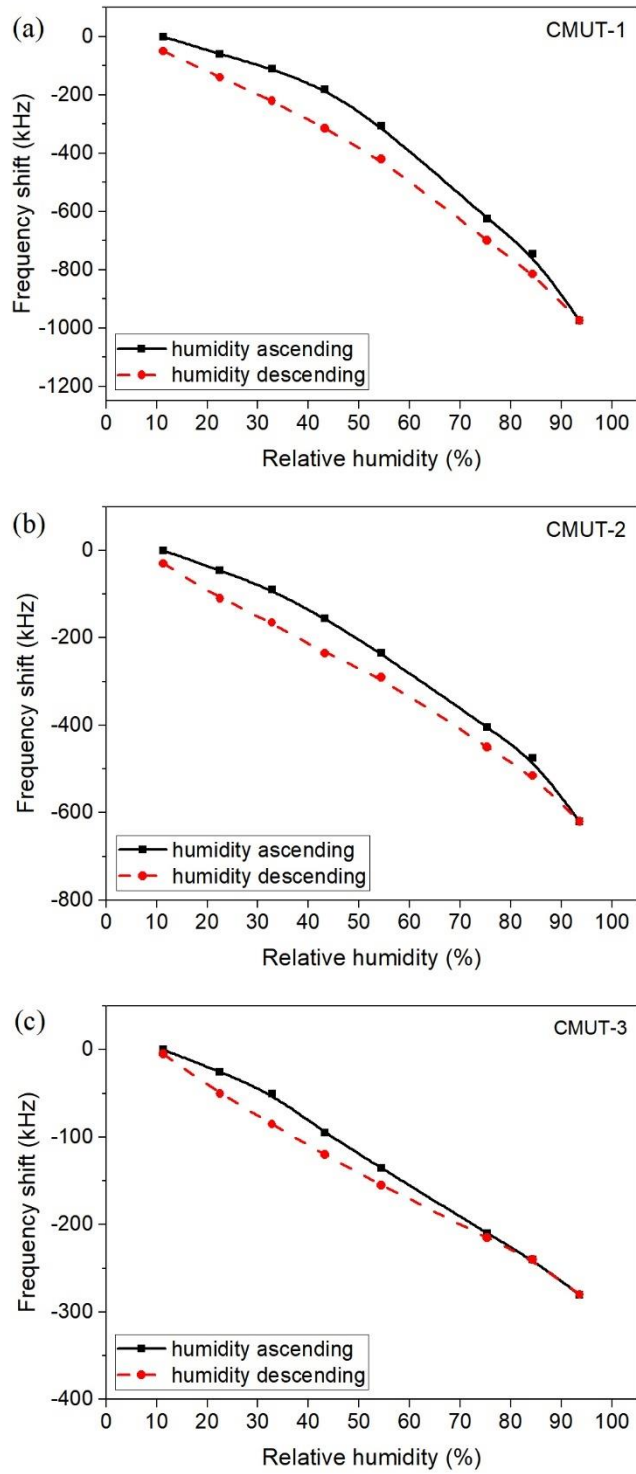
Fig. 6.13: Humidity hysteresis curves of CMUT sensors: (a) CMUT-1; (b) CMUT-2; (c) CMUT-3.

6.7 Summary

This chapter presents CMUT-based humidity sensors that were fabricated by the nitride-to-oxide wafer bonding technology. In contrast to conventional wafer bonding CMUT processes that use expensive SOI wafers to produce resonating membranes, the proposed process employs LPCVD Si_3N_4 as the membrane material, which provides thinner and lighter membranes and thus more sensitive CMUT resonators. Furthermore, additional benefits such as reduced fabrication complexity and more controllable membrane thickness are possible. Ten MHz CMUTs were designed and fabricated. The device uniformities and resonance frequencies were characterized by a laser vibrometer and a VNA. Three CMUTs were functionalized by GO with a dispersion concentration of 0.5 mg/ml, 0.25 mg/ml, and 0.1 mg/ml. Over an RH range from 11.3% to 93.6%, the sensors showed a maximum RH sensitivity of 15.3 kHz/%RH, 8.7 kHz/%RH, and 3.5 kHz/%RH, respectively. The CMUT coated with the highest concentration exhibited the highest sensitivity. Decent repeatability and a short response/recovery time were achieved by all the CMUT sensors. This work demonstrates that CMUT sensors realized by the nitride-to-oxide wafer bonding technique are promising for highly sensitive humidity sensing. Due to their exceptional mass sensitivity, the developed fabrication process can also be suitable for constructing CMUTs for other bio/chemical applications.

Chapter 7   A Multi-Resonance CMUT for Sensing Applications

7.1 Introduction

The last two chapters have demonstrated the benefits of CMUT as a strong humidity sensor. In some cases, however, being sensitive to only one specific analyte like humidity is not good enough. A sensing system is sometimes desirable to discriminate diverse chemical vapors. Currently, one of the most popular solutions for that is the electronic nose system, which uses an array of multiple sensors. Each sensor is functionalized by a specific film that is selectively sensitive to one analyte. By extracting and analyzing the multi-channel signals, it is possible to identify or classify chemical vapors [108], [109]. Microcantilever- [110], [111], QCM- [112]–[114] and SAW-based [115]–[117] sensors have been implemented for such purposes. However, due to the increased complexity in readout circuits and modification processes, these sensing platforms suffer from the large footprint, high cost and power consumption, and degraded long term stability [109].

To overcome these limitations, virtual sensor arrays have been investigated in recent years as an alternative to the multi-sensor array scheme. A virtual sensor array uses a single sensor to generate multiple independent outputs simulating an array [118]. The sensor is functionalized by a sensing material with diverse responses to different analytes. Data analysis on the multi-dimensional responses can provide similar results as achieved by the physical multi-sensor arrays. To date, multi-frequency virtual sensor arrays based

on piezoelectric resonant sensors such as QCM [119]–[121], SAW [122], and bulk acoustic wave resonators [108] have been realized. These sensors employed signals at multiple resonant orders/harmonics to produce diverse responses on different analytes. They have achieved relatively high sensitivities and also the promising capability of distinguishing various analytes. However, due to the intrinsic coupling between harmonic signals, the frequency-dependent responses of these resonators are not completely independent, and hence limiting their ability of vapor discrimination [108]. Moreover, constructing piezoelectric-based resonant sensors with multiple independent resonances is challenging because of the manufacturing constraints.

In this chapter, a single-chip multi-resonance CMUT is proposed as a new alternative. As indicated in Eq. (3.11), the resonance frequency of a CMUT can be adjusted by varying the radius of the membrane. Using microfabrication technology, it is easy to implement multiple membrane radii or resonance frequencies on a single-chip CMUT. Because CMUT cells with different resonances are free of internal coupling, they are able to generate completely independent responses for sensing applications. In addition, the flexible choice on the membrane sizes enables almost arbitrary resonance designs, compared to sorely the fundamental and harmonic signal detections for the piezoelectric-based resonators. All these features make CMUT a powerful alternative as a virtual sensor array for vapor discrimination. The feasibility of multi-size structured CMUTs has recently been demonstrated for medical imaging applications [123], [124]. These arrays consist of interlaced low frequency (LF) and high frequency (HF) sub-arrays that are

electrically insulated and separately operated. In this work, we propose a dual-resonance CMUT with LF (10 MHz) and HF (14 MHz) cells electrically connected in parallel. Using a frequency sweep, two independent resonances can be detected simultaneously and be used for gravimetric sensing. Due to time and experimental condition constraints, the multi-resonance CMUTs were used for humidity sensing only and not used for vapor discrimination. The multi-resonance design still owns its advantages over single-frequency configurations when used for detection of a single analyte. Multiple responses can be produced instead of one, providing more reliable and accurate sensing results.

In this chapter, design, fabrication, and characterization of the multi-resonance CMUT are elaborated. The humidity sensing performance of the GO-modified CMUT sensor is examined by measuring its RH sensitivity, repeatability, dynamic response, and hysteresis characteristics.

7.2 Operational Principle and Design

Fig. 7.1 (a) shows the structure of the dual-resonance CMUT humidity sensor. It consists of many electrically connected cells with two different radii. Functionalized by GO, when the mass of adsorbed water molecules is added on the membranes, two independent frequency shifts will be induced at the resonances. According to Eq. (5.1), the HF cells have a higher mass sensitivity and hence a larger frequency shift. Based on the distinguished frequency shifts, two frequency-dependent responses can be achieved

when the sensor is exposed to various RH levels. The two responses provide more accurate sensing and potentially can be used for discrimination of two chemical vapors.
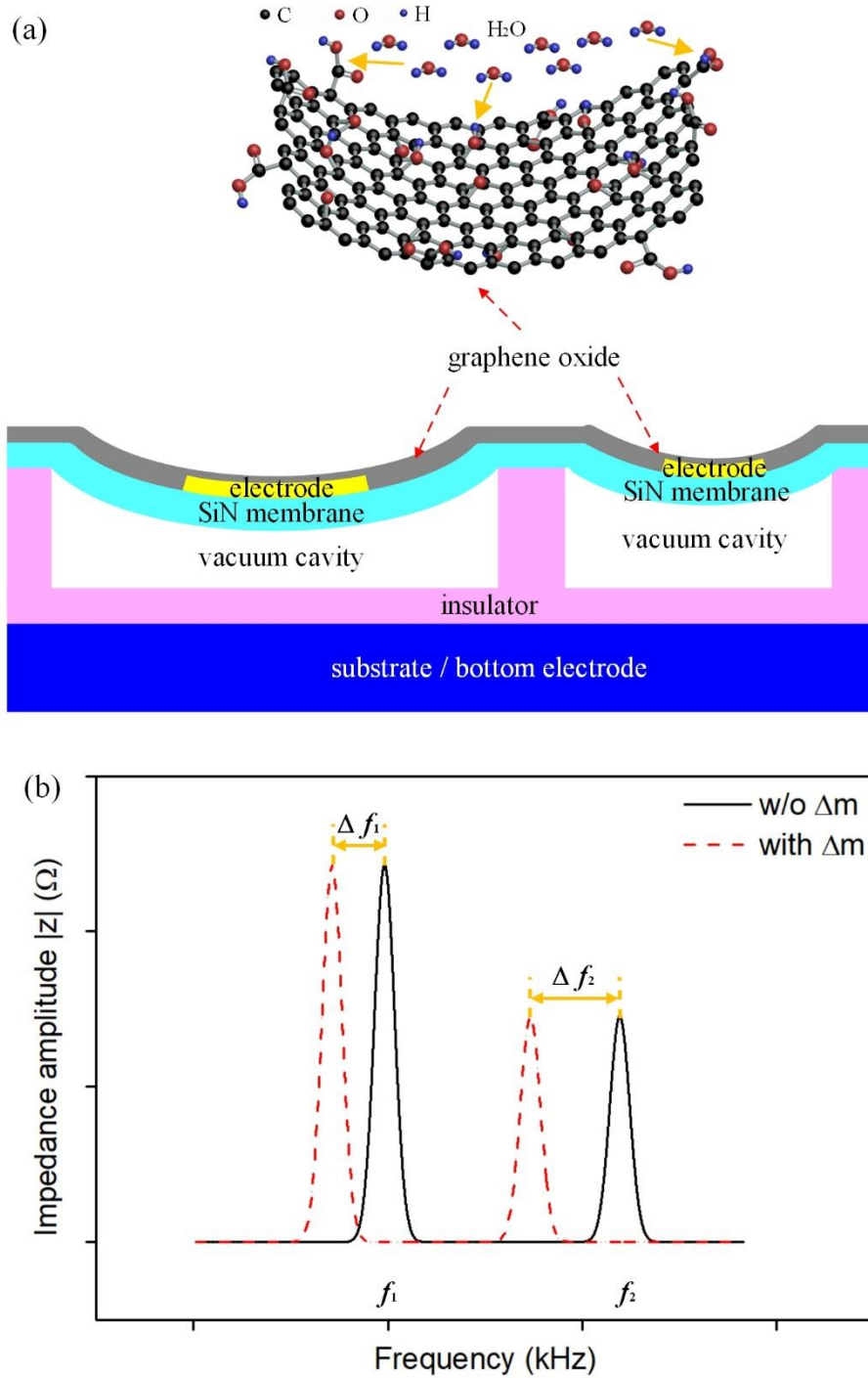
Fig. 7.1: (a) Structure of the dual frequency CMUT; (b) working mechanism of the dual frequency

CMUT humidity sensor.

Table 7.1 Design parameters of the dual-resonance CMUT.

Parameter	Value
Resonance frequencies	10 MHz / 14 MHz
Membrane thickness	520 nm
LF membrane diameter	30 μm
HF membrane diameter	25 μm
Cavity depth	180 nm
Electrode thickness	100 nm
Number of LF cells	1260
Number of HF cells	1188

A 1 mm * 2.5 mm rectangular CMUT with Si_3N_4 membrane were designed for humidity sensing. The critical design parameters are presented in Table 7.1. The LF resonance of the CMUT was selected to be 10 MHz. The HF resonance was designed as a synthetical consideration of the sensing performance, the operating voltage, and the fabrication complexity. In terms of the sensing performance, a largely separated pair of dual frequencies is favorable because it generates more distinguishable responses. The downside is that it requires a longer frequency sweeping time during the sensing process if we want to keep the resolution of detection. As the LF and HF cells are biased and excited simultaneously during operation, they should ideally have equal pull-in voltages to ensure the SNR at both resonances. To achieve this objective, Eq. (6.1) suggests that an efficient way is to create a shallower cavity depth for the HF cells. However, making

cavities with various depths on a single chip requires extra photomasks and patterning and etching steps, which increases the fabrication complexity and cost. A solution is to choose two close resonances such that the corresponding CMUT cells can have the same cavity depths and also close pull-in voltages. Although close resonances may cause crosstalk and degrade the identifiability of the two responses, a compromise can be reached upon careful consideration. Here, the HF resonance was chosen to be 14 MHz as a trade-off between the sensing performance and the fabrication complexity.

Given the designed resonances and the membrane thickness of 520 nm, the membrane radii were uniquely determined via FEA simulation. The DC operating voltage was designed to be under 50 V and the cavity depth was determined accordingly. The final CMUT was composed of 1260 LF cells and 1188 HF cells.

7.3 Sensor Fabrication

The process flow of the dual-resonance CMUT is depicted in Fig. 7.2. The CMUT was fabricated using the same nitride-to-oxide wafer bonding process as introduced in Chapter 6. The only modification is that cavities with two different radii were created simultaneously in step (b). Fig. 7.2 (g) shows the fabricated device. The CMUT was functionalized by drop-casting 8 µL GO dispersion with a concentration of 0.1 mg/ml. This concentration was selected because it provided reasonably high sensitivity and also relatively less damping to the sensor as proved in Chapter 6. The sensor was then kept in room temperature for three weeks before it served as a humidity sensor.
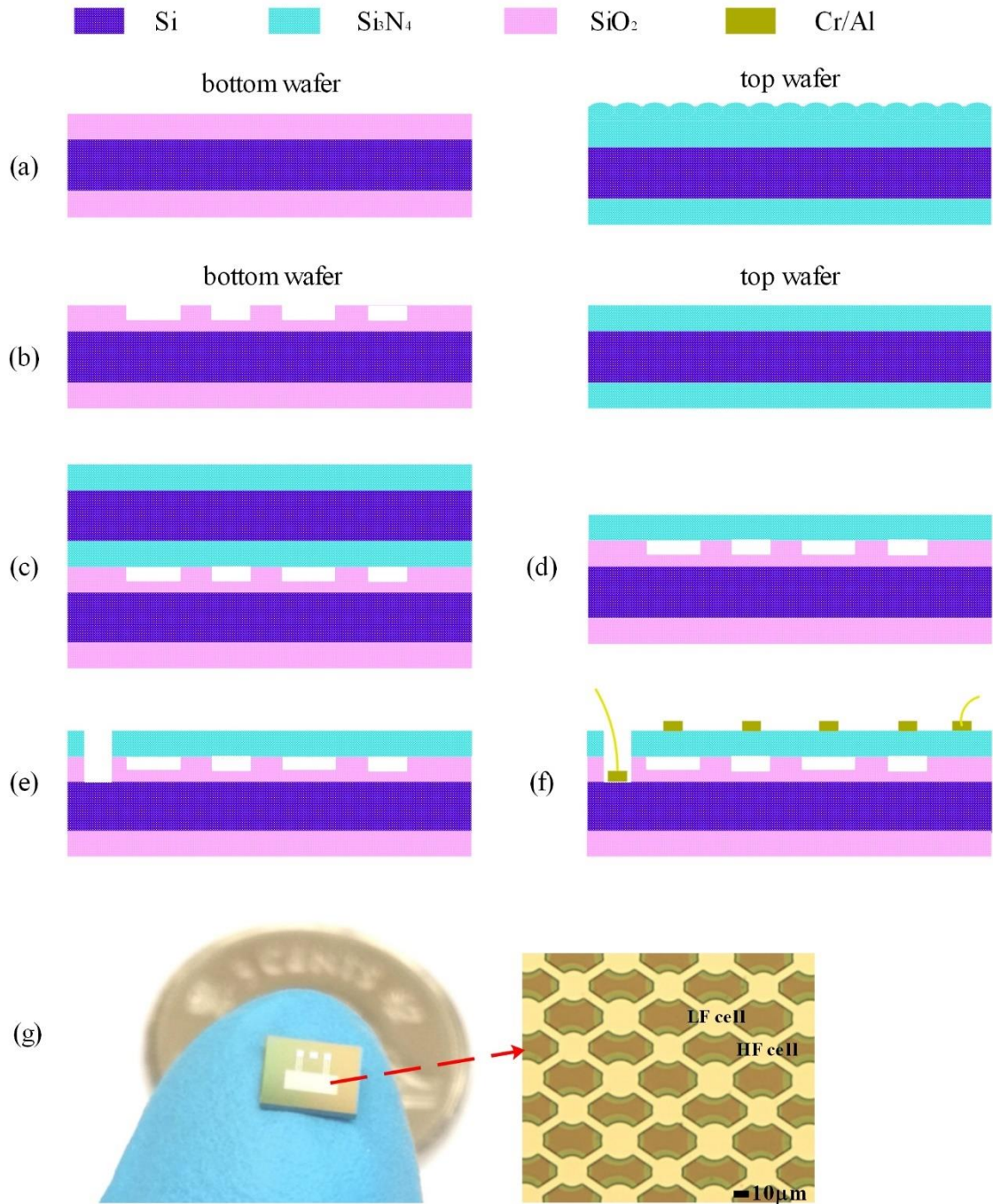
Fig. 7.2: Process flow of the dual frequency CMUT.

7.4 Device Characterization
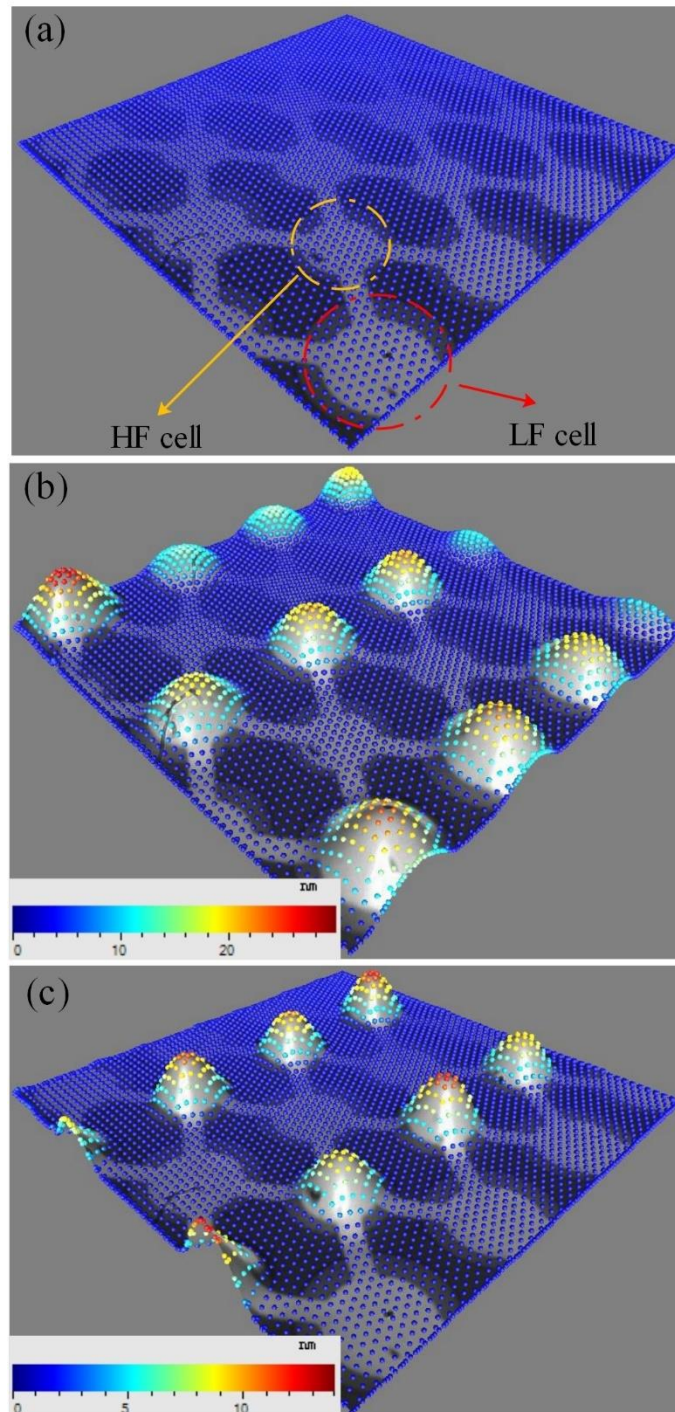
Fig. 7.3: Vibrometer displacement measurement of the dual frequency CMUT at a 30 V bias

voltage: (a) without AC excitation; (b) with a 1 Vpp AC signal at 9.94 MHz; (c) with a 1 Vpp AC

signal at 13.72 MHz.

Before functionalization of the CMUT, a laser vibrometer test was carried out to check the mechanical vibration and resonance frequencies of the cells, as well as the crosstalk between the two resonances. First, 20 LF cells and 20 HF cells were randomly chosen for the resonance test. The resonance frequencies were measured to be 9.94 MHz and 13.72 MHz, respectively, with a maximum variation of ±1.1%. Fig. 7.3 shows the 2D scan images of the membrane displacements when the CMUT was biased at 30 V and excited at different AC signals. In Fig. 7.3 (a), no membrane vibration was observed without AC excitation. It can be seen from Fig. 7.3(b) and Fig. 7.3 (c) that membranes of the LF and HF cells reached the maximum displacements near their resonances, respectively, and there was no evident crosstalk between the two resonances. Small variations in the displacement amplitude were observed. This was attributed to the resonance variation between the cells. The vibration measurement proved the complete independence between the two frequencies, which is favorable for vapor discrimination applications.

The electrical input impedance of the CMUT was characterized by the VNA. The pull-in voltages of the LF cells and the HF cells were measured to be $V_{pi\_LF} = 62V$ and $V_{pi\_HF} = 79V$, respectively. Fig. 7.4 (a) and Fig. 7.4 (b) show the impedances at various bias voltages before and after functionalization of the CMUT, respectively. To avoid the collapse of any cells, the operating voltage was determined based on the pull-in voltage of the LF cells. The maximum bias in this test was 40 V, which was $0.65 \cdot V_{pi\_LF}$ and $0.51 \cdot V_{pi\_HF}$. Both resonances were clearly identified from a single frequency sweep. It

can be seen that the LF resonance was always stronger than the HF resonance. This was because the dual frequency CMUT had a larger number of LF cells and the operating voltage was closer to the pull-in voltage of the LF cells. It is also observed that the coating of GO film has slightly damped the resonation of the CMUT and also degraded the quality factor. Nevertheless, the resonances were still easily detectable because the loaded damping was small.
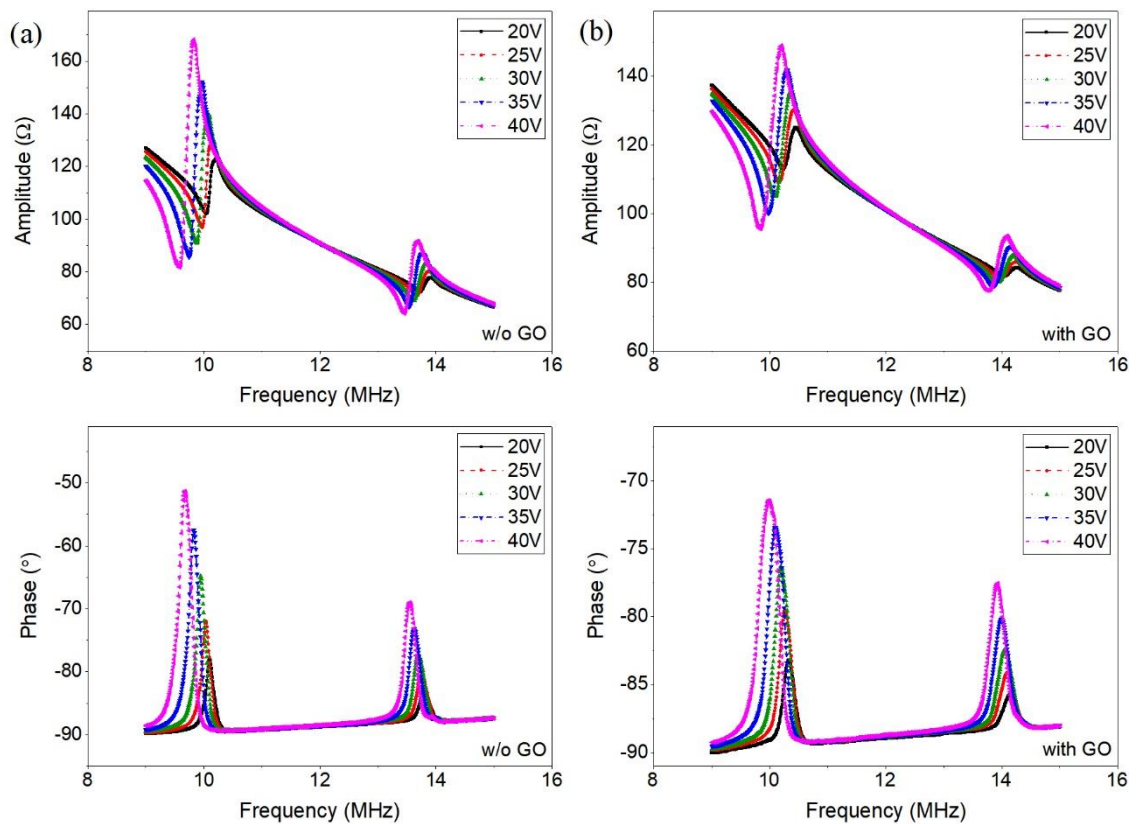
Fig. 7.4: Electrical impedance measurement of the CMUT: (a) without GO; (b) with GO.

Fig. 7.5 shows the parallel resonance frequencies of the CMUT as a function of the bias voltage. Before functionalization, the resonances had a good agreement with that measured from the laser vibrometer characterization. At the bias of 30 V, for instance, the measured resonance frequencies were 10.08 MHz and 13.82 MHz from the

impedance test, very close to 9.94 MHz and 13.72 MHz from the vibrometer test. The spring softening effect was observed at both resonances. After coating of the GO film, the resonances arose slightly due to the increased effective membrane thickness and the resonance shift was larger at the HF resonance because of the higher sensitivity.
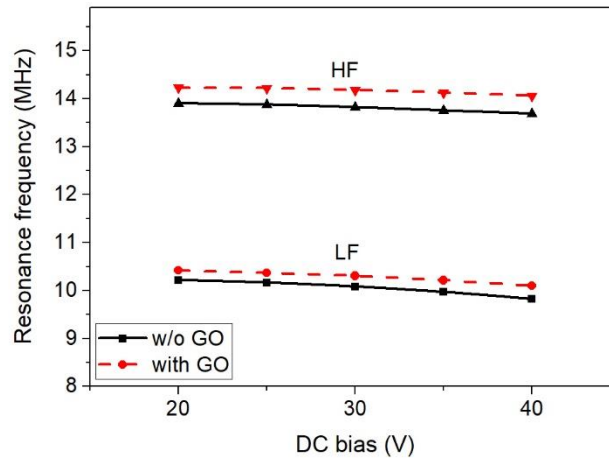
Fig. 7.5: Resonance frequencies as a function of bias voltage.
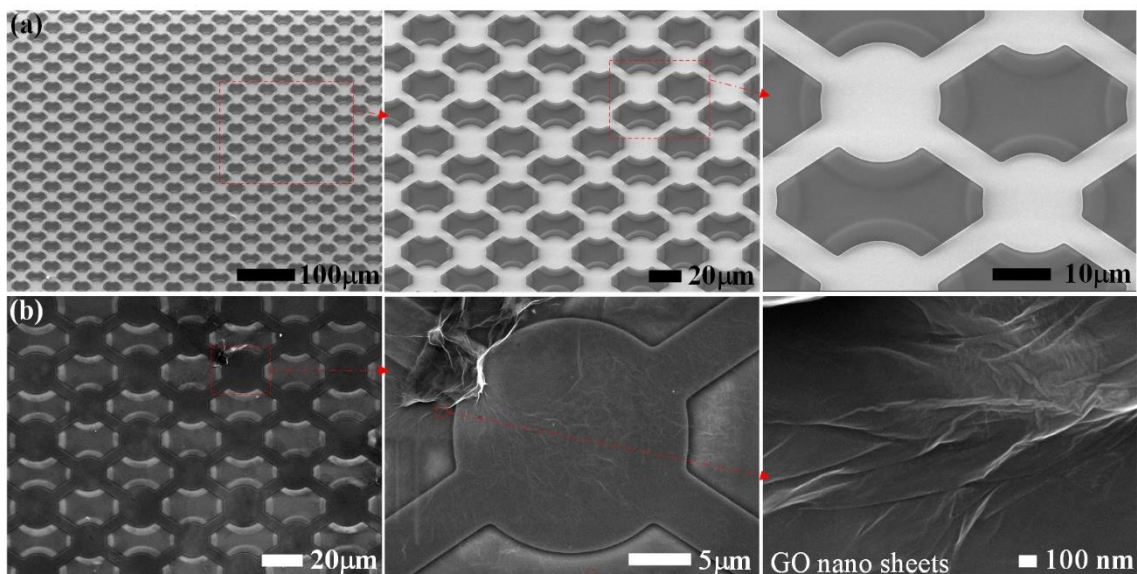
Fig. 7.6: SEM images of the CMUT: (a) without GO; (b) with GO.

Fig. 7.6 (a) and Fig. 7.6 (b) present the SEM images of the CMUT without and with GO coating, respectively. Cells with different resonances can be clearly visualized. A

cluster of GO was observed in Fig. 7.6 (b). This was not desirable because it was formed

by many layers of GO nanosheet and might cause trapping of water molecules, which

might degrade the reversibility of the sensor.

7.5 Results and Discussion
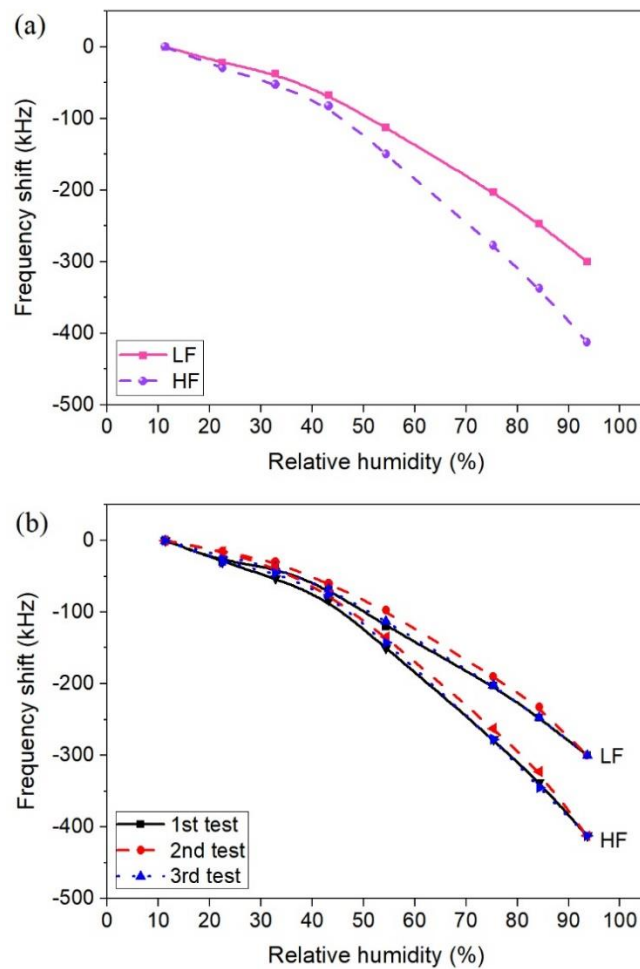
Fig. 7.7: Humidity sensing measurements of the dual frequency CMUT: (a) frequency shifts as a

function of RH; (b) frequency responses in three measurements.

The humidity sensing measurement was performed using the setup shown in Fig.

6.10. The CMUT sensor was tested at a biased voltage of 35 V at room temperature. The

frequency shifts of both resonances were characterized. Fig. 7.7 (a) displays the

frequency responses as the RH increased from 11.3% to 93.6%. The sensing performance

of the sensor is summarized in Table 7.2. The sensor showed distinguished sensitivities

at the two resonances. Similar to the results in Chapter 6, the sensor at both resonances,

had larger frequency shifts at higher RH levels due to the adequate adsorption of water

molecules. Accordingly, the RH sensitivity was calculated in the RH ranges of 11% - 43%

and 43% - 93%. The maximum sensitivities at the LF and HF resonances are 4.6

kHz/%RH and 6.4 kHz/%RH, respectively. The higher sensitivity of the HF cells was

attributed to their smaller membrane radius, as indicated in Eq. (5.1). Fig. 7.7 (b) shows

the responses of three tests on different days. The CMUT humidity sensor exhibited

outstanding repeatability at both the LF and HF resonances, with a maximum

repeatability error of $\pm 3.7\%$ and $\pm 2.7\%$, respectively.

Table 7.2 Humidity sensing performance of the dual frequency CMUT sensor.

Resonance		LF	HF
Humidity sensitivity	RH 11%-43%	2.1	2.5
(kHz/%RH)	RH 43%-93%	4.6	6.4
Maximum repeatability error (%)		± 3.7	± 2.7
Response/recovery time (s)		11/4	12/5

The dynamic response of the CMUT was characterized by switching the sensor

between the laboratory ambiance (22% RH) and the 75.3% RH environment. The

resonance shifts were recorded by the VNA and the Labview program. In order to

enhance the sampling rate, the LF and the HF resonance shifts were measured separately.

Fig. 7.8 shows the dynamic response of the sensor. The measured response/recovery time at the two resonances was 11/4 s and 12/5 s, respectively.
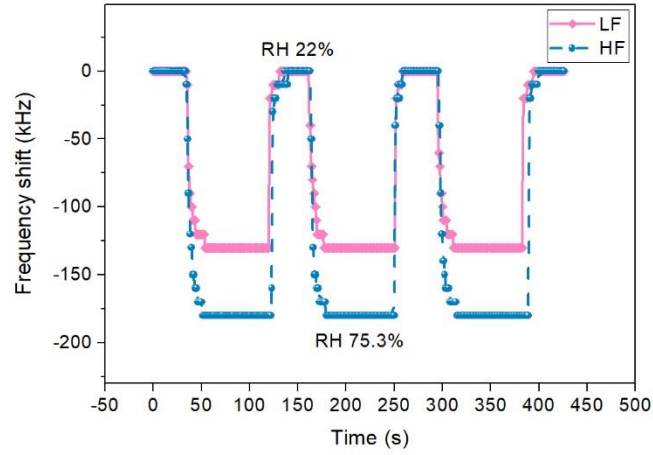
Fig. 7.8: Dynamic frequency shift of the dual frequency CMUT sensor with the RH level switching between 22% and 75.3%.
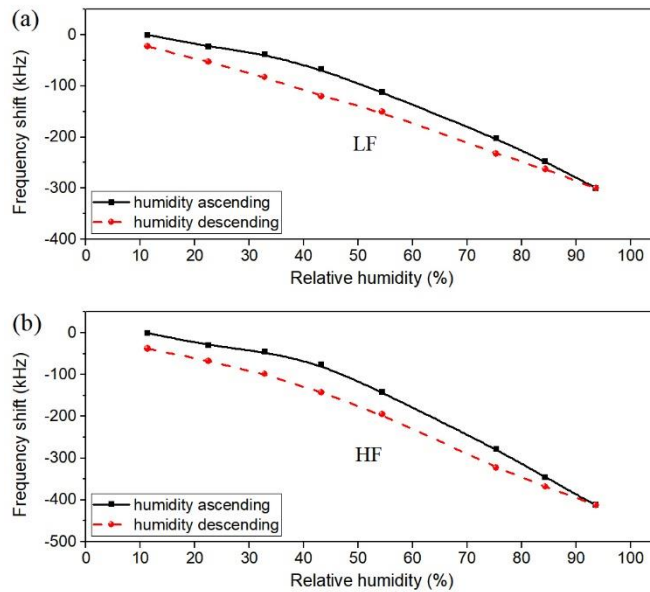
Fig. 7.9: Humidity hysteresis curves of the dual frequency CMUT sensor: (a) at LF resonance; (b) at HF resonance.

The humidity hysteresis of the CMUT sensor was examined by gradually increasing the RH level from 11.3% to 93.6% and then decreasing back to 11.3%. Hysteresis still

remained a problem for the sensor due to the trapped water molecules in the interlayer of the GO film. The level of hysteresis was similar at the two resonances and reached the maximum at 43.2% RH. Coating a thinner and more uniform layer of GO film will possibly suppress the hysteresis.

7.6 Summary

This chapter reports a multi-resonance CMUT fabricated by the nitride-to-oxide wafer bonding technology. With the ultimate goal of implementing vapor discrimination, this sensor was solely used for moisture sensing due to time constraints. A single-resonance CMUT is eligible for humidity detection but not for vapor discrimination. The multi-resonance CMUT (10 MHz/14 MHz) was designed and fabricated to overcome this limitation. The basic idea was to utilize the frequency dependency of the mass sensitivity. By implementing two resonances in a single sensor, two distinct responses can be achieved for selective sensing. Characterizations on the CMUT membrane vibration showed that the two resonation states were able to function completely independent. The CMUT was then functionalized by 0.1 mg/mL GO and applied for humidity sensing. It generated two isolated responses at two resonances, with a maximum sensitivity of 4.6 kHz/%RH and 6.4 kHz/%RH, respectively. It also exhibited decent repeatability and rapid response/recovery. Compared to sensors that can only produce a single response, the multi-resonance CMUT could significantly decrease the chance of false alarms and potentially be used for vapor discrimination.

Chapter 8   Summary and Future Work

8.1 Summary of Contributions

CMUT was initially proposed for air-coupled NDT applications in the early 1990s. Since then, it has gained tremendous interests and has been considered as the next-generation of acoustic imaging transducers which may compete with piezoelectric transducers [6]. Because many attractive features of CMUTs, the compact size in particular, address several challenges met by conventional piezoelectric transducers, most of the ongoing CMUT research focuses on medical imaging applications. Yet, CMUTs have certain limitations with low output pressure being one of them. Part of the thesis aims to provide a solution to this issue.

The first contribution of this thesis is developing a novel hybrid ultrasound transducer which may offer a new perspective for ultrasound imaging applications. By integrating an annular CMUT and a circular piezoelectric probe, the benefits of the two transducer technologies are combined for enhanced sensitivity and resolution. The fabrication process of the annular CMUT is presented and a concentric configuration is proposed for its integration with the piezoelectric probe. Potential variations of the hybrid configuration have been discussed for promising medical imaging applications. This work is presented in Chapter 4.

Chemical sensing is a relatively new area for CMUTs. Although CMUT-based humidity sensing is even less studied, it can be expected that CMUTs inherit all benefits

that have been achieved from other chemical sensing applications. Such advantages include the high mass sensitivity, reliability, ease of functionalization, and minimized array configuration. This thesis first looked into the feasibility of using GO film to functionalize CMUTs for highly sensitive humidity sensing, then dedicated to further improving the sensing performance by developing new CMUTs.

The second contribution is developing a highly sensitive CMUT-based humidity sensor that uses GO as the sensing layer. The efficiency of incorporating the mass-sensitive CMUT and the moisture-sensitive GO is studied for the first time. The CMUT sensor generates a higher RH sensitivity than most of other reported gravimetric humidity sensors. It also shows excellent repeatability and fast response/recovery. This work is presented in Chapter 5.

The third contribution is proposing the nitride-to-oxide wafer bonding process to fabricate CMUT-based humidity sensors for enhanced sensing performance. Compared to the conventional SOI-based fabrication method, this process offers reduced fabrication complexity and cost, improved sensitivity, and superior device uniformity. The high sensitivity of the fabricated CMUTs is demonstrated through humidity sensing tests. The proposed fabrication process is not only suitable for humidity sensing, but also for other chemical sensing applications. This work is presented in Chapter 6.

The fourth contribution is developing a multi-resonance CMUT for sensing applications for the first time. The functionalized CMUT is able to generate two independent frequency responses to each specific analyte, showing great potential for

chemical vapor discrimination. It has the same capability as the multi-sensor arrays but requires much simpler operation and sensing circuits. Moreover, in applications where only one analyte such as water vapor needs to be detected, the multi-response CMUT can provide more accurate and reliable results than single frequency measurements. This work is presented in Chapter 7.

8.2 Future Work

8.2.1   CMUTs for Medical Applications

In Chapter 4, the study contributes to the initial investigation of integrating the piezoelectric transducer and the CMUT. This idea can be further extended for medical applications. Variations of the hybrid transducer can be pursued in the future. A potential variation is a transducer that consists of a multi-element CMUT ring array and a piezoelectric-based circular element or ring array. By using the CMUT array for conventional B-mode imaging and the piezoelectric transducer for high-power therapeutic purposes such as hyperthermia and drug delivery, the hybrid transducer would be suitable for image-guided therapy.

An even more promising variation of the hybrid transducer will be composed of a LF (f_L = 1 to 5 MHz) piezoelectric transmitter and a HF ($f_H \geq 2f_L$) CMUT receiver. It is believed that the ultra-broadband transducer will offer new perspectives for harmonic imaging, which enhances visualization of blood vessels by transmitting ultrasound at the fundamental frequency f_L and receives at two or higher times of the transmit frequency

[81], [125]. The wide bandwidth of CMUTs is particularly valuable for high-order ($>2^{nd}$) harmonic imaging, because it allows detection of multiple harmonic components so as to improve the SNR [81]. However, the exploitation of CMUTs for harmonic imaging is currently limited by their inherent nonlinearity. The acoustic pulse generated by CMUTs contains an undesirable 2nd harmonic component due to the dependence of electrostatic force on the square of the applied voltage and the membrane displacement [126], [127]. The unwanted harmonic signal pollutes the nonlinear response of the explored media and thus deteriorates the image quality [126], [128]. An alternative transducer for harmonic imaging can be the hybrid transducer that uses a piezoelectric probe for ultrasound transmission and a CMUT for harmonic reception. Consequently, the nonlinearity is avoided and the wide bandwidth of the CMUT is employed for high SNR harmonic imaging.

8.2.2 CMUTs for Sensing Applications

This thesis has laid the foundation of CMUT-based humidity sensors. The focus of this work is mainly on the sensor development for humidity sensing. While the ultimate goal of this research program is to fulfill a highly sensitive, reliable, and portable CMUT-based sensing system that can discriminate multiple chemical vapors including moisture, a few things can be pursued beyond this thesis in the future.

8.2.2.1 Optimization on CMUT Design

Due to consideration of the fabrication yield and the condition of the equipment at the time of fabrication, the CMUTs were designed conservatively. Their potential is not

fully developed yet. Further improvement can be made by optimizing the design. First, the mass sensitivity of the CMUTs can be enhanced by increasing the resonance frequency and decreasing the membrane radius. Second, the operating voltage of the CMUTs can be minimized for portable sensing applications. The minimum operating bias of the CMUTs in this thesis is 35 V. Although a bias voltage of 20 V should also be applicable, the price will be the degraded SNR and resolution of detection. As mentioned in Chapter 6, an effective way of minimizing the operating voltage can be decreasing the cavity depth and membrane thickness. The third improvement in the future is to develop multi-element CMUT arrays and CMUTs with more than two resonances as electronic nose systems. A dual-resonance CMUT has been presented in Chapter 7. However, the maximum number of chemicals that can be discriminated is only two at a time. By implementing more resonances in a CMUT or more elements in a CMUT array, it is possible to detect and distinguish more types of chemicals.

8.2.2.2 Optimization on Sensing Material

GO has been used as the sensing material throughout this thesis and it has shown excellent performance on moisture adsorption. However, it has also caused a relatively high level of hysteresis. A possible reason for the hysteresis is that the coated GO film is not optimized for a good thickness and uniformity. The thicker the sensing film, the more chance that water molecules will be trapped in the interlayer, which deteriorates the reversibility. The thickness of GO film can be reduced by simply diluting the GO dispersion. But reducing the concentration will decrease the sensitivity of the sensor. The

concentration of GO dispersion employed in this thesis ranges from 0.1 mg/ml to 1 mg/ml. An optimal dose of GO dispersion can be investigated in the future to find a balance between the sensitivity and the reversibility.
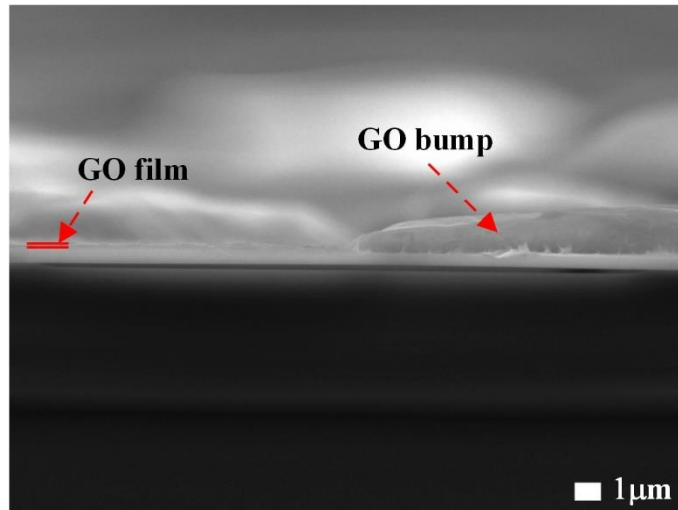
Fig. 8.1: SEM image of the CMUT showing non-uniform coating of GO film.

The coating method of the GO film in this thesis is drop-casting, which is known for its uncontrollable uniformity. Fig. 8.1 displays the SEM image of a CMUT membrane drop-casted with the 0.1 mg/ml GO dispersion. A large bump is observed and it is several times thicker than the average GO thickness. A badly controlled drop-casting might result in countless bumps, which generates a considerable volume to trap water molecules and leads to notable hysteresis. To improve the uniformity of the sensing film, other coating techniques such as spin coating and inkjet printing can be investigated.

Another cause of the hysteresis might be the strong interaction between GO and water molecules. It is known that the sensitivity and the reversibility of a material are a pair of contradiction. Because a high sensitivity requires strong adsorption of water molecules, whereas good reversibility needs the interaction to be weak such that the

device can rapidly return to its original status. Therefore, it is worth studying more other

sensing materials such as nanostructured polymers for an optimal trade-off between the

sensitivity and the reversibility.

Bibliography

[1]   Z. Zheng *et al.*, "Development of a novel CMUT-based concentric dual-element ultrasonic transducer: Design, fabrication, and characterization," *J. Microelectromechanical Syst.*, vol. 27, no. 3, pp. 538–546, 2018.

[2]   Z. Zheng, Y. Yao, Y. Sun, and J. Yeow, "Development of a highly sensitive humidity sensor based on the capacitive micromachined ultrasonic transducer," *Sensors Actuators B Chem.*, vol. 286, pp. 39–45, 2019.

[3]   Z. Zheng, Y. Yao, J. A. Liu, Y. Sun, and J. T. W. Yeow, "Highly sensitive CMUT-based humidity sensors built with nitride-to-oxide wafer bonding technology," *Sensors Actuators B Chem.*, vol. 294, pp. 123–131, 2019.

[4]   M. I. Haller and B. T. Khuri-yakub, "A surface micromachined electrostatic ultrasonic air transducer," in *Ultrasonics Symposium*, 1994, pp. 1241–1244.

[5]   M. I. Haller and B. T. Khuri-yakub, "A surface micromachined electrostatic ultrasonic air transducer," *IEEE Trans. Ultrason. Ferroelectr. Freq. Control*, vol. 43, no. 1, 1996.

[6]   O. Oralkan *et al.*, "Capacitive micromachined ultrasonic transducers: Next-generation arrays for acoustic imaging?," *IEEE Trans. Ultrason. Ferroelectr. Freq. Control*, vol. 49, no. 11, pp. 1596–1610, 2002.

[7]   G. Caliano *et al.*, "Design, fabrication and characterization of a capacitive micromachined ultrasonic probe for medical imaging," *IEEE Trans. Ultrason. Ferroelectr. Freq. Control*, vol. 52, no. 12, pp. 2259–2269, 2005.

[8]   B. T. Khuri-Yakub and O. Oralkan, "Capacitive micromachined ultrasonic transducers for medical imaging and therapy," *J. Micromechanics Microengineering*, vol. 21, no. 5, pp. 054004–054014, 2011.

[9]   A. S. Ergun, Y. Huang, X. Zhuang, O. Oralkan, G. G. Yaralioglu, and B. T. Khuri-Yakub, "Capacitive micromachined ultrasonic transducers: Fabrication technology," *IEEE Trans. Ultrason. Ferroelectr. Freq. Control*, vol. 52, no. 12, pp. 2242–2258, 2005.

[10]   K. K. Park *et al.*, "Capacitive micromachined ultrasonic transducers for chemical detection in nitrogen," *Appl. Phys. Lett.*, vol. 91, no. 9, pp. 3–5, 2007.

[11]   H. J. Lee, K. K. Park, M. Kupnik, Ö. Oralkan, and B. T. Khuri-Yakub, "Chemical vapor detection using a capacitive micromachined ultrasonic transducer," *Anal. Chem.*, vol. 83, no. 24, pp. 9314–9320, 2011.

[12]   K. K. Park *et al.*, "Capacitive micromachined ultrasonic transducer (CMUT) as a chemical sensor for DMMP detection," *Sensors Actuators B Chem.*, vol. 160, no. 1, pp. 1120–1127, 2011.

[13]   H. J. Lee, K. K. Park, Ö. Oralkan, M. Kupnik, and B. T. Khuri-Yakub, "A multichannel oscillator for a resonant chemical sensor system," *IEEE Trans. Ind. Electron.*, vol. 61, no. 10, pp. 5632–5640, 2014.

[14] L. Zhao, Y. Zhao, Y. Xia, Z. Li, J. Li, and J. Zhang, "A novel CMUTs-based resonant biochemical sensor using electrospinning technology," *IEEE Trans. Ind. Electron.*, pp. 1–10, 2018.

[15] C. Lee and G. Lee, "Humidity sensors: A review," *Sensors Lett.*, vol. 3, pp. 1–14, 2005.

[16] H. Farahani, R. Wagiran, and M. N. Hamidon, "Humidity sensors principle, mechanism, and fabrication technologies: A comprehensive review," *Sensors*, vol. 14, no. 5, pp. 7881–7939, 2014.

[17] X. Le *et al.*, "A high performance humidity sensor based on surface acoustic wave and graphene oxide on AlN/Si layered structure," *Sensors Actuators, B Chem.*, vol. 255, pp. 2454–2461, 2018.

[18] W. Xuan *et al.*, "A film bulk acoustic resonator oscillator based humidity sensor with graphene oxide as the sensitive layer," *J. Micromechanics Microengineering*, vol. 27, no. 5, 2017.

[19] C. Steffens, A. Manzoli, F. L. Leite, O. Fatibello, and P. S. P. Herrmann, "Atomic force microscope microcantilevers used as sensors for monitoring humidity," *Microelectron. Eng.*, vol. 113, pp. 80–85, 2014.

[20] G. Chen *et al.*, "Film bulk acoustic resonators integrated on arbitrary substrates using a polymer support layer," *Sci. Rep.*, vol. 5, pp. 1–8, 2015.

[21] T. L. Szabo, *Diagnostic ultrasound imaging: Inside out*, 2nd ed. Kidlington, Oxford, United Kingdom: Academic Press, 2014.

[22] K. Martin *et al.*, "Dual-Frequency Piezoelectric Transducers for Contrast Enhanced Ultrasound Imaging," *Sensors*, vol. 14, no. 11, pp. 20825–20842, 2014.

[23] A. S. Ergun, G. G. Yaralioglu, and B. T. Khuri-yakub, "Capacitive micromachined ultrasonic transducers: Theory and technology," *J. Aerosp. Eng.*, vol. 16, no. 2, pp. 76–84, 2003.

[24] X. Cheng *et al.*, "CMUT-in-CMOS ultrasonic transducer arrays with on-chip electronics," in *International Conference on Solid-State Sensors, Actuators and Microsystems (Transducers)*, 2009, pp. 1222–1225.

[25] J. Zahorian *et al.*, "Monolithic CMUT-on-CMOS integration for intravascular ultrasound applications," *IEEE Trans. Ultrason. Ferroelectr. Freq. Control*, vol. 58, no. 12, pp. 2659–2667, 2011.

[26] G. Gurun, P. Hasler, and F. L. Degertekin, "Front-end receiver electronics for high-frequency monolithic CMUT-on-CMOS imaging arrays," *IEEE Trans. Ultrason. Ferroelectr. Freq. Control*, vol. 58, no. 8, pp. 1658–1668, 2011.

[27] A. Bhuyan *et al.*, "3D volumetric ultrasound imaging with a 32×32 CMUT array integrated with front-end ICs using flip-chip bonding technology," in *IEEE International Solid-State Circuits Conference Digest of Technical Papers (ISSCC)*, 2013, pp. 396–398.

[28] C. K. Abbey, N. Q. Nguyen, and M. F. Insana, "Effects of frequency and bandwidth on diagnostic information transfer in ultrasonic B-Mode imaging,"

IEEE Trans. Ultrason. Ferroelectr. Freq. Control, vol. 59, no. 6, pp. 1115–1126, 2012.

[29] A. Savoia, G. Caliano, B. Mauti, and M. Pappalardo, "Performance optimization of a high frequency CMUT probe for medical imaging," in *IEEE International Ultrasonics Symposium, IUS*, 2011, pp. 600–603.

[30] A. S. Savoia, G. Caliano, and M. Pappalardo, "A CMUT probe for medical ultrasonography: From microfabrication to system integration," *IEEE Trans. Ultrason. Ferroelectr. Freq. Control*, vol. 59, no. 6, pp. 1127–1138, 2012.

[31] S. Luryi, J. Xu, and A. Zaslavsky, *Future trends in microelectronics: Frontiers and innovations*. Hoboken, New Jersey: Wiley-IEEE Press, 2013.

[32] M. J. G. Mølgaard, M. Laustsen, M. H. Jakobsen, T. L. Andresen, and E. V. Thomsen, "Combined colorimetric and gravimetric CMUT sensor for detection of benzyl methyl ketone," *Sensors Actuators B Chem.*, vol. 275, no. July, pp. 483–489, 2018.

[33] Q. Stedman, K. K. Park, and B. T. Khuri-Yakub, "Distinguishing chemicals using CMUT chemical sensor array and artificial neural networks," *IEEE Int. Ultrason. Symp. IUS*, pp. 162–165, 2014.

[34] D. Barauskas, D. Pelenis, D. Virzonis, J. P. Baltrus, and J. Baltrusaitis, "Greenhouse gas molecule CO_2 detection using a capacitive micromachined ultrasound transducer," *Anal. Chem.*, vol. 88, no. 13, pp. 6662–6665, 2016.

[35] H. J. Lee, K. K. Park, M. Kupnik, and B. T. Khuri-Yakub, "Functionalization layers for CO2 sensing using capacitive micromachined ultrasonic transducers," *Sensors Actuators, B Chem.*, vol. 174, pp. 87–93, 2012.

[36] H. J. Lee, K. K. P. an D M. Kupnik, Ö. Oralkan, and B. T. Khuri-Yakub, "Highly sensitive detection of DMMP using a CMUT chemical sensor," in *IEEE Sensors Conference*, 2010, pp. 2122–2126.

[37] K. K. P. K. K. Park, H. J. Lee, M. Kupnik, O. Oralkan, and B. T. Khuri-Yakub, "Capacitive micromachined ultrasonic transducer as a chemical sensor," in *IEEE Sensors Conference*, 2008, vol. 160, no. 1, pp. 5–8.

[38] Y. Huang, A. S. Ergun, E. Haggstrom, M. H. Badi, and B. T. Khuri-Yakub, "Fabricating capacitive micromachined ultrasonic transducers with wafer-bonding technology," *J. Microelectromechanical Syst.*, vol. 12, no. 2, pp. 128–137, 2003.

[39] A. Tripathy *et al.*, "Design and development for capacitive humidity sensor applications of lead-free Ca, Mg, Fe, Ti-oxides-based electro-ceramics with improved sensing properties via physisorption," *Sensors*, vol. 16, no. 7, 2016.

[40] K. J. Park and M. S. Gong, "A water durable resistive humidity sensor based on rigid sulfonated polybenzimidazole and their properties," *Sensors Actuators, B Chem.*, vol. 246, pp. 53–60, 2017.

[41] X. Gan *et al.*, "High performance graphene oxide-based humidity sensor integrated on a photonic crystal cavity," *Appl. Phys. Lett.*, vol. 110, no. 15, pp. 1–5, 2017.

[42] Y. Yao, X. Chen, H. Guo, and Z. Wu, "Graphene oxide thin film coated quartz crystal microbalance for humidity detection," *Appl. Surf. Sci.*, vol. 257, no. 17, pp. 7778–7782, 2011.

[43] S. Wang *et al.*, "Reduced graphene oxide-polyethylene oxide composite films for humidity sensing via quartz crystal microbalance," *Sensors Actuators, B Chem.*, vol. 255, pp. 2203–2210, 2018.

[44] D. Zhang, D. Wang, X. Zong, G. Dong, and Y. Zhang, "High-performance QCM humidity sensor based on graphene oxide/tin oxide/polyaniline ternary nanocomposite prepared by in-situ oxidative polymerization method," *Sensors Actuators, B Chem.*, vol. 262, pp. 531–541, 2018.

[45] L. García-Gancedo *et al.*, "ZnO-Based FBAR resonators with carbon nanotube electrodes," *IEEE Trans. Ultrason. Ferroelectr. Freq. Control*, vol. 58, no. 11, pp. 2438–2445, 2011.

[46] Y. Zhu, H. Yuan, J. Xu, P. Xu, and Q. Pan, "Highly stable and sensitive humidity sensors based on quartz crystal microbalance coated with hexagonal lamelliform monodisperse mesoporous silica SBA-15 thin film," *Sensors Actuators, B Chem.*, vol. 144, no. 1, pp. 164–169, 2010.

[47] J. Xie, H. Wang, Y. Lin, Y. Zhou, and Y. Wu, "Highly sensitive humidity sensor based on quartz crystal microbalance coated with ZnO colloid spheres," *Sensors Actuators, B Chem.*, vol. 177, pp. 1083–1088, 2013.

[48] S. Rey-mermet, R. Lanz, and P. Muralt, "Bulk acoustic wave resonator operating at 8 GHz for gravimetric sensing of organic films," *Sensors Actuators B Chem.*, vol. 114, pp. 681–686, 2006.

[49] T. Y. Lee and J. T. Song, "Detection of carcinoembryonic antigen using AlN FBAR," *Thin Solid Films*, vol. 518, no. 22, pp. 6630–6633, 2010.

[50] Y. Zhang, J. Luo, A. J. Flewitt, Z. Cai, and X. Zhao, "Film bulk acoustic resonators (FBARs) as biosensors: A review," *Biosens. Bioelectron.*, vol. 116, no. May, pp. 1–15, 2018.

[51] G. Korotcenkov, *Handbook of humidity measurement, volume 2: Electronic and electrical humidity sensors*. Taylor & Francis Group, 2019.

[52] H. Sone, H. Okano, and S. Hosaka, "Picogram mass sensor using piezoresistive cantilever for biosensor," *Japanese J. Appl. Physics, Part 1 Regul. Pap. Short Notes Rev. Pap.*, vol. 43, no. 7 B, pp. 4663–4666, 2004.

[53] M. Li, H. X. Tang, and M. L. Roukes, "Ultra-sensitive NEMS-based cantilevers for sensing, scanned probe and very high-frequency applications," *Nat. Nanotechnol.*, vol. 2, no. 2, pp. 114–120, 2007.

[54] Z. Chen and C. Lu, "Humidity Sensors: A Review of Materials and Mechanisms," *Sens. Lett.*, vol. 3, no. 4, pp. 274–295, 2005.

[55] W. Hu, S. Chen, B. Zhou, L. Liu, B. Ding, and H. Wang, "Highly stable and sensitive humidity sensors based on quartz crystal microbalance coated with

bacterial cellulose membrane," *Sensors Actuators B Chem.*, vol. 159, no. 1, pp. 301–306, 2011.

[56] H. Y. Yoo and S. Bruckenstein, "A novel quartz crystal microbalance gas sensor based on porous film coatings. A high sensitivity porous poly(methylmethacrylate) water vapor sensor," *Anal. Chim. Acta*, vol. 785, pp. 98–103, 2013.

[57] A. Glück, W. Halder, G. Lindner, H. Müller, and P. Weindler, "PVDF-excited resonance sensors for gas flow and humidity measurements," *Sensors Actuators B Chem.*, vol. 19, no. 1–3, pp. 554–557, 1994.

[58] J. Xu, M. Bertke, H. S. Wasisto, and E. Peiner, "Piezoresistive microcantilevers for humidity sensing," *J. Micromechanics Microengineering*, 2019.

[59] U. Mittal, T. Islam, A. T. Nimal, and M. U. Sharma, "A novel sol–Gel γ-Al2O3 thin-film-based rapid SAW humidity sensor," *IEEE Trans. Electron Devices*, vol. 62, no. 12, pp. 4242–4250, 2015.

[60] N. Sakly, A. Haj Said, and H. Ben Ouada, "Humidity-sensing properties of ZnO QDs coated QCM: Optimization, modeling and kinetic investigations," *Mater. Sci. Semicond. Process.*, vol. 27, no. 1, pp. 130–139, 2014.

[61] A. I. Buvailo, Y. Xing, J. Hines, N. Dollahon, and E. Borguet, "TiO2/LiCl-based nanostructured thin film for humidity sensor applications," *ACS Appl. Mater. Interfaces*, vol. 3, no. 2, pp. 528–533, 2011.

[62] F. Yakuphanoglu, "Semiconducting and quartz microbalance (QCM) humidity sensor properties of TiO2 by sol gel calcination method," *Solid State Sci.*, vol. 14, no. 6, pp. 673–676, 2012.

[63] M. Procek, A. Stolarczyk, T. Pustelny, and E. Maciak, "A study of a QCM sensor based on TiO2 nanostructures for the detection of NO2 and explosives vapours in air," *Sensors*, vol. 15, no. 4, pp. 9563–9581, 2015.

[64] Y. Yao *et al.*, "Novel QCM humidity sensors using stacked black phosphorus nanosheets as sensing film," *Sensors Actuators, B Chem.*, vol. 244, pp. 259–264, 2017.

[65] H. W. Chen, R. J. Wu, K. H. Chan, Y. L. Sun, and P. G. Su, "The application of CNT/Nafion composite material to low humidity sensing measurement," *Sensors Actuators, B Chem.*, vol. 104, no. 1, pp. 80–84, 2005.

[66] A. L. Robinson *et al.*, "Ultrasensitive humidity detection using metal-organic framework-coated microsensors," *Anal. Chem.*, vol. 84, no. 16, pp. 7043–7051, 2012.

[67] L. Kosuru, A. Bouchaala, N. Jaber, and M. I. Younis, "Humidity detection using MOF Coated on QCM," *J. Sensors*, vol. 2016, pp. 1–8, 2016.

[68] K. K. Park, "Capacitive micromachined ultrasonic transducer (cmut) for chemical detection in air," 2011.

[69] I. O. Wygant, M. Kupnik, and B. T. Khuri-Yakub, "Analytically calculating membrane displacement and the equivalent circuit model of a circular CMUT cell," in *IEEE International Ultrasonics Symposium, IUS*, 2008, no. 6, pp. 2111–2114.

[70] X. Zhuang, "Capacitive micromachined ultrasonic transducers with through-wafer interconnects," 2008.

[71] G. G. Yaralioglu, A. S. Ergun, B. Bayram, E. Haeggström, and B. T. Khuri-Yakub, "Calculation and measurement of electromechanical coupling coefficient of capacitive micromachined ultrasonic transducers.," *IEEE Trans. Ultrason. Ferroelectr. Freq. Control*, vol. 50, no. 4, pp. 449–456, 2003.

[72] C. Cao, T. Filleter, M. Daly, and C. V. Singh, "High strength measurement of monolayer graphene oxide," *Carbon N. Y.*, vol. 81, pp. 497–504, 2014.

[73] T. Bayer, S. R. Bishop, N. H. Perry, K. Sasaki, and S. M. Lyth, "Tunable mixed ionic/electronic conductivity and permittivity of graphene oxide paper for electrochemical energy conversion," *Appl. Mater. Interfaces*, vol. 8, no. 18, pp. 11466–11475, 2016.

[74] J. Wan, J. Jiang, and H. S. Park, "Negative Poisson's ratio in graphene oxide," *Nanoscale*, vol. 9, no. 11, pp. 4007–4012, 2017.

[75] L. L. P. Wong, A. I. H. Chen, Z. Li, A. S. Logan, and J. T. W. Yeow, "A row–column addressed micromachined ultrasonic transducer array for surface scanning applications," *Ultrasonics*, vol. 54, no. 8, pp. 2072–2080, 2014.

[76] D. M. Mills and L. S. Smith, "Real-time in-vivo imaging with capacitive micromachined ultrasound transducer (cMUT) linear arrays," in *IEEE International Ultrasonics Symposium, IUS*, 2003, pp. 568–571.

[77] B. Bayram, O. Oralkan, A. S. Ergun, E. Haeggstrom, G. G. Yaralioglu, and B. T. Khuri-Yakub, "Capacitive micromachined ultrasonic transducer design for high power transmission," *IEEE Trans. Ultrason. Ferroelectr. Freq. Control*, vol. 52, no. 2, pp. 326–339, 2005.

[78] R. O. Guldiken, J. McLean, and F. L. Degertekin, "CMUTS with dual-electrode structure for improved transmit and receive performance," *IEEE Trans. Ultrason. Ferroelectr. Freq. Control*, vol. 53, no. 2, pp. 483–491, 2006.

[79] Y. Huang, E. O. Haggstrom, A. S. Ergun, and B. T. Khuri-Yakub, "Optimized membrane configuration improves CMUT performance," *IEEE Int. Ultrason. Symp. IUS*, pp. 505–508, 2004.

[80] Y. Huang, X. Zhuang, E. O. Haggstrom, A. S. Ergun, C.-H. Cheng, and B. T. Khuri-Yakub, "Capacitive micromachined ultrasonic transducers with piston-shaped membranes: Fabrication and experimental characterization," *IEEE Trans. Ultrason. Ferroelectr. Freq. Control*, vol. 56, no. 1, pp. 136–145, 2009.

[81] R. Gessner, M. Lukacs, M. Lee, E. Cherin, F. S. Foster, and P. A. Dayton, "High-resolution, high-contrast ultrasound imaging using a prototype dual-frequency transducer: In vitro and in vivo studies," *IEEE Trans. Ultrason. Ferroelectr. Freq. Control*, vol. 57, no. 8, pp. 1772–1781, 2010.

[82]   M. Lukacs *et al.*, "Hybrid dual frequency transducer and scanhead for micro-ultrasound imaging," in *IEEE International Ultrasonics Symposium, IUS*, 2009, pp. 1000–1003.

[83]   H. H. Kim, J. M. Cannata, R. Liu, J. H. Chang, R. H. Silverman, and K. K. Shung, "20 MHz/40 MHz dual element transducers for high frequency harmonic imaging," *IEEE Trans. Ultrason. Ferroelectr. Freq. Control*, vol. 55, no. 12, pp. 2683–2691, 2008.

[84]   B. A. J. Angelsen, *Ultrasound Imaging: Waves, signals and signal processing*. Trondheim, Norway: Emantec AS, 2000.

[85]   R. J. McGough, T. V. Samulski, and J. F. Kelly, "An efficient grid sectoring method for calculations of the near-field pressure generated by a circular piston," *J. Acoust. Soc. Am.*, vol. 115, no. 5 Pt 1, pp. 1942–1954, 2004.

[86]   D. Chen and R. J. McGough, "A 2D fast near-field method for calculating near-field pressures generated by apodized rectangular pistons," *J. Acoust. Soc. Am.*, vol. 124, no. 3, pp. 1526–1537, 2008.

[87]   S. Na, Z. Zheng, A. I. Chen, L. L. P. Wong, Z. Li, and J. T. W. Yeow, "Design and fabrication of a high-power air-coupled capacitive micromachined ultrasonic transducer array with concentric annular cells," *IEEE Trans. Electron Devices*, vol. 64, no. 11, pp. 4636–4643, 2017.

[88]   W. Kern and J. E. Soc, "The evolution of silicon wafer cleaning technology," *J. Electrochem. Soc.*, vol. 137, no. 6, pp. 1887–1892, 1990.

[89] A. A. Ayon, R. Braff, C. C. Lin, H. H. Sawin, and M. A. Schmidt, "Characterization of a time multiplexed inductively coupled plasma etcher," *J. Electrochem. Soc.*, vol. 146, no. 1, pp. 339–349, 1999.

[90] J. Y. Lu, H. Zou, and J. F. Greenleaf, "Biomedical ultrasound beam forming," *Ultrasound Med. Biol.*, vol. 20, no. 5, pp. 403–428, 1994.

[91] A. Weyns, "Radiation field calculations of pulsed ultrasonic transducers. Part 1: Planar circular, square and annular transducers," *Ultrasonics*, vol. 18, no. 4, pp. 183–188, 1980.

[92] H. J. Lee, K. K. Park, M. Kupnik, N. A. Melosh, and B. T. Khuri-Yakub, "Mesoporous thin-film on highly-sensitive resonant chemical sensor for relative humidity and CO_2detection," *Anal. Chem.*, vol. 84, no. 7, pp. 3063–3066, 2012.

[93] S. Kim *et al.*, "Room-temperature metastability of multilayer graphene oxide films," *Nat. Mater.*, vol. 11, no. 6, pp. 544–549, 2012.

[94] L. Greenspan, "Humidity fixed points of binary saturated aqueous solutions," *J. Res. Natl. Bur. Stand. - A. Phys ics Chem.*, vol. 81A, no. 1, pp. 89–96, 1977.

[95] R. Mavaddat, *Network scattering parameters (Vol. 2)*. World Scientific, 1996.

[96] H. Bi *et al.*, "Ultrahigh humidity sensitivity of graphene oxide," *Sci. Rep.*, vol. 3, no. 5 V, pp. 1–7, 2013.

[97] Y. Tang *et al.*, "Highly sensitive surface acoustic wave (SAW) humidity sensors based on sol-gel SiO_2 films: Investigations on the sensing property and mechanism," *Sensors Actuators, B Chem.*, vol. 215, pp. 283–291, 2015.

[98] X. Qiu *et al.*, "Film bulk acoustic-wave resonator based relative humidity sensor using ZnO films," *Electrochem. Solid-State Lett.*, vol. 13, no. 5, pp. J65–J67, 2010.

[99] Z. Yuan *et al.*, "Novel highly sensitive QCM humidity sensor with low hysteresis based on graphene oxide (GO)/poly(ethyleneimine) layered film," *Sensors Actuators, B Chem.*, vol. 234, pp. 145–154, 2016.

[100] M. Björkqvist, J. Paski, J. Salonen, and V. P. Lehto, "Studies on hysteresis reduction in thermally carbonized porous silicon humidity sensor," *IEEE Sens. J.*, vol. 6, no. 3, pp. 542–546, 2006.

[101] A. Logan and J. T. W. Yeow, "Fabricating capacitive micromachined ultrasonic transducers with a novel silicon-nitride-based wafer bonding process," *IEEE Trans. Ultrason. Ferroelectr. Freq. Control*, vol. 56, no. 5, pp. 1074–1084, 2009.

[102] A. I. H. Chen, L. L. P. Wong, Z. Li, S. Na, and J. T. W. Yeow, "Practical CMUT fabrication with a nitride-to-oxide-based wafer bonding process," *J. Microelectromechanical Syst.*, vol. 26, no. 4, pp. 829–836, 2017.

[103] Ö. Oralkan *et al.*, "Experimental characterization of collapse-mode CMUT operation," *IEEE Trans. Ultrason. Ferroelectr. Freq. Control*, vol. 53, no. 8, pp. 1513–1523, 2006.

[104] A. S. Logan, L. L. P. Wong, A. I. H. Chen, and J. T. W. Yeow, "A 32 x 32 element row-column addressed capacitive micromachined ultrasonic transducer," *IEEE Trans. Ultrason. Ferroelectr. Freq. Control*, vol. 58, no. 6, pp. 1266–1271, 2011.

[105] J. B. Lasky, "Wafer bonding for silicon-on-insulator technologies," *Appl. Phys. Lett.*, vol. 48, no. 1, pp. 78–80, 1986.

[106] M. Shimbo, K. Furukawa, K. Fukuda, and K. Tanzawa, "Silicon-to-silicon direct bonding method," *J. Appl. Phys.*, vol. 60, no. 8, pp. 2987–2989, 1986.

[107] J. Haisma, G. A. C. M. Spierings, U. K. P. Biermann, and J. A. Pals, "Silicon-on-insulator wafer bonding-wafer thinning technological evaluations," *Jpn. J. Appl. Phys.*, vol. 28, no. 8, pp. 1426–1443, 1989.

[108] Y. Zhao *et al.*, "Detection and discrimination of volatile organic compounds using a single multi-resonance mode piezotransduced silicon bulk acoustic wave resonator (PSBAR) as virtual sensor array," *Sensors Actuators, B Chem.*, vol. 254, pp. 1191–1199, 2018.

[109] A. Oprea and U. Weimar, "Gas sensors based on mass-sensitive transducers part 1: transducers and receptors-basic understanding," *Anal. Bioanal. Chem.*, 2019.

[110] D. Lange, C. Hagleitner, A. Hierlemann, O. Brand, and H. Baltes, "Complementary metal oxide semiconductor cantilever arrays on a single chip: Mass-sensitive detection of volatile organic compounds," *Anal. Chem.*, vol. 74, no. 13, pp. 3084–3095, 2002.

[111] A. Bietsch, J. Zhang, M. Hegner, H. P. Lang, and C. Gerber, "Rapid functionalization of cantilever array sensors by inkjet printing," *Nanotechnology*, vol. 15, no. 8, pp. 873–880, 2004.

[112] J. Rabe, S. Büttgenbach, J. Schröder, and P. Hauptmann, "Monolithic miniaturized quartz microbalance array and its application to chemical sensor systems for liquids," *IEEE Sens. J.*, vol. 3, no. 4, pp. 361–368, 2003.

[113] X. Jin, Y. Huang, A. Mason, and X. Zeng, "Multichannel monolithic quartz crystal microbalance gas sensor array," *Anal. Chem.*, vol. 81, no. 2, pp. 595–603, 2009.

[114] R. Toniolo, A. Pizzariello, N. Dossi, S. Lorenzon, O. Abollino, and G. Bontempelli, "Room temperature ionic liquids as useful overlayers for estimating food quality from their odor analysis by quartz crystal microbalance measurements," *Anal. Chem.*, vol. 85, no. 15, pp. 7241–7247, 2013.

[115] K. T. Tang, C. H. Li, and S. W. Chiu, "An electronic-nose sensor node based on a polymer-coated surface acoustic wave array for wireless sensor network applications," *Sensors*, vol. 11, no. 5, pp. 4609–4621, 2011.

[116] U. Stahl *et al.*, "Long-term stability of polymer-coated surface transversewave sensors for the detection of organic solvent vapors," *Sensors (Switzerland)*, vol. 17, no. 11, 2017.

[117] J. Devkota, P. R. Ohodnicki, and D. W. Greve, "SAW sensors for chemical vapors and gases," *Sensors (Switzerland)*, vol. 17, no. 4, pp. 13–15, 2017.

[118] R. A. Potyrailo, "Multivariable sensors for ubiquitous monitoring of gases in the era of internet of things and industrial internet," *Chem. Rev.*, vol. 116, no. 19, pp. 11877–11923, 2016.

[119] N. Siraj, H. Marzoughi, B. P. Regmi, C. Neal, I. M. Warner, and N. C. Speller, "Rational Design of QCM-D Virtual Sensor Arrays Based on Film Thickness, Viscoelasticity, and Harmonics for Vapor Discrimination," *Anal. Chem.*, vol. 87, no. 10, pp. 5156–5166, 2015.

[120] N. C. Speller, N. Siraj, K. S. McCarter, S. Vaughan, and I. M. Warner, "QCM virtual sensor array: Vapor identification and molecular weight approximation," *Sensors Actuators, B Chem.*, vol. 246, pp. 952–960, 2017.

[121] N. C. Speller, N. Siraj, S. Vaughan, L. N. Speller, and I. M. Warner, "QCM virtual multisensor array for fuel discrimination and detection of gasoline adulteration," *Fuel*, vol. 199, pp. 38–46, 2017.

[122] W. Seidel and T. Hesjedal, "Multimode and multifrequency gigahertz surface acoustic wave sensors," *Appl. Phys. Lett.*, vol. 84, no. 8, pp. 1407–1409, 2004.

[123] A. Kshirsagar *et al.*, "Multi-frequency CMUT arrays for imaging-therapy applications," in *IEEE International Ultrasonics Symposium, IUS*, 2013, pp. 1991–1993.

[124] R. K. W. Chee, P. Zhang, M. Maadi, and R. J. Zemp, "Multi-Frequency Interlaced CMUTs for Photoacoustic Imaging," *IEEE Trans. Ultrason. Ferroelectr. Freq. Control*, vol. 64, no. 2, pp. 391–401, 2017.

[125] Y. E. Chung and K. W. Kim, "Contrast-enhanced ultrasonography: Advance and current status in abdominal imaging," *Ultrasonography*, vol. 34, no. 1, pp. 3–18, 2014.

[126] A. Novell, M. Legros, N. Felix, and A. Bouakaz, "Exploitation of capacitive micromachined transducers for nonlinear ultrasound imaging.," *IEEE Trans. Ultrason. Ferroelectr. Freq. Control*, vol. 56, no. 12, pp. 2733–2743, 2009.

[127] S. Zhou, P. Reynolds, and J. Hossack, "Precompensated excitation waveforms to suppress harmonic generation in MEMS electrostatic transducers," *IEEE Trans. Ultrason. Ferroelectr. Freq. Control*, vol. 51, no. 11, pp. 1564–1574, 2004.

[128] A. Novell, M. Legros, J.-M. Grégoire, P. A. Dayton, and A. Bouakaz, "Evaluation of bias voltage modulation sequence for nonlinear contrast agent imaging using a capacitive micromachined ultrasonic transducer array," *Phys. Med. Biol.*, vol. 59, no. 17, pp. 4879–4896, 2014.